



Compositional Study of Trans-Neptunian Objects at $\lambda > 2.2 \mu\text{m}$

E. Fernández-Valenzuela¹ , N. Pinilla-Alonso¹ , J. Stansberry² , J. P. Emery³ , W. Perkins⁴, C. Van Laerhoven⁵ , B. J. Gladman⁵ , W. Fraser⁶ , D. Cruikshank⁷ , E. Lellouch⁸ , T. G. Müller⁹ , W. M. Grundy¹⁰ , D. Trilling³ , Y. Fernandez¹¹ , and C. Dalle Ore^{12,7}

¹ Florida Space Institute, University of Central Florida, 12354 Research Parkway, Partnership 1, Orlando, FL, USA; estela@ucf.edu

² Space Telescope Science Institute, Baltimore, MD, USA

³ Department of Astronomy and Planetary Sciences, Northern Arizona University, Flagstaff, AZ, USA

⁴ Department of Earth and Planetary Sciences, University of Tennessee, Knoxville, TN, USA

⁵ University of British Columbia, Department of Physics and Astronomy, 6224 Agricultural Road, Vancouver, BC, Canada

⁶ NRC Herzberg Astrophysics, BC, Canada

⁷ NASA Ames Research Center, Moffett Field, CA, USA

⁸ LESIA, Observatoire de Paris, Meudon, France

⁹ Max-Planck-Institut für Extraterrestrische Physik, Center for Astrochemical Studies, Garching, Germany

¹⁰ Lowell Observatory, Flagstaff, AZ, USA

¹¹ Department of Physics, University of Central Florida, Orlando, FL, USA

¹² SETI Institute, Mountain View, CA, USA

Received 2020 April 21; revised 2020 October 13; accepted 2020 October 13; published 2021 January 25

Abstract

Using data from the Infrared Array Camera on the Spitzer Space Telescope, we present photometric observations of a sample of 100 trans-Neptunian objects (TNOs) beyond $2.2 \mu\text{m}$. These observations, collected with two broadband filters centered at 3.6 and $4.5 \mu\text{m}$, were done in order to study the surface composition of TNOs, which are too faint to obtain spectroscopic measurements. With this aim, we have developed a method for the identification of different materials that are found on the surfaces of TNOs. In our sample, we detected objects with colors that are consistent with the presence of small amounts of water, and we were able to distinguish between surfaces that are predominantly composed of complex organics and amorphous silicates. We found that 86% of our sample have characteristics that are consistent with a certain amount of water ice, and the most common composition (73% of the objects) is a mixture of water ice, amorphous silicates, and complex organics. Twenty-three percent of our sample may include other ices, such as carbon monoxide, carbon dioxide, methane, or methanol. Additionally, only small objects seem to have surfaces dominated by silicates. This method is a unique tool for the identification of complex organics and to obtain the surface composition of extremely faint objects. Furthermore, this method will be beneficial when using the James Webb Space Telescope for differentiating groups within the trans-Neptunian population.

Unified Astronomy Thesaurus concepts: [Trans-Neptunian objects \(1705\)](#); [Solar system formation \(1530\)](#); [Small solar system bodies \(1469\)](#); [Surface composition \(2115\)](#); [Infrared photometry \(792\)](#); [Broad band photometry \(184\)](#)

Supporting material: figure set, machine-readable tables

1. Introduction

Trans-Neptunian objects (TNOs) are solar system objects whose heliocentric orbits have semimajor axes a greater than that of Neptune and less than where the Oort cloud begins, i.e., $30.07 < a < 2000$ au (Gladman et al. 2008). Centaurs, with semimajor axes a between those of Jupiter and Neptune, are a significant population of objects in the region between the giant planets; from a compositional point of view, they are of great interest because these nearby objects are easier to study and believed to be derived from TNOs via perturbations by Neptune and the other giant planets (Fernandez 1980; Levison & Duncan 1997). Therefore, both populations are studied together, with the understanding that there is a greater chance of recent modification of Centaur surfaces as they approach the Sun from the trans-Neptunian region.

Due to their large heliocentric distances, all TNOs have surface temperatures that are low enough to retain water ice.

Non-Centaur TNOs can also harbor highly volatile ices such as CO_2 , CH_4 , CO , and N_2 in stable form, although the last three are likely only present on the TNO dwarf planets, which have enough mass to trap them gravitationally (Schaller & Brown 2007a; Pinilla-Alonso et al. 2020; Young et al. 2020). In addition to these molecular ices, TNO surfaces are thought to be composed of refractory macromolecular complexes (termed tholins), derived via photolysis and radiolysis of ices (Khare et al. 1993; Materese et al. 2014, 2015), and silicates incorporated as grains during accretion from the solar nebula. The slightly to extremely red colors of some TNOs likely reflect the presence of these organic “tholins,” although some silicates can also be slightly reddish in the visible spectral region.

Determining the relationships between the physical properties of TNOs to their dynamical classifications and orbital histories may help us understand the composition and thermal state of the solar nebula as a function of heliocentric radius (e.g., Fernández 2020). The cold classical objects in the main belt (see Section 3.1) are the only ones thought to still reside in their primordial orbits (e.g., Brown 2001; Van Laerhoven et al. 2019); TNOs in all other classes were likely perturbed greatly



Original content from this work may be used under the terms of the [Creative Commons Attribution 4.0 licence](#). Any further distribution of this work must maintain attribution to the author(s) and the title of the work, journal citation and DOI.

from their original orbits by interactions with the migrating giant planets (e.g., Gladman et al. 2008; Petit et al. 2011; Morbidelli & Nesvorný 2020). However, establishing the composition–dynamics relationship is difficult because TNOs are so faint (typical $m_V \gtrsim 20$). Relatively few have near-IR colors, which could be diagnostic of composition, let alone near-IR spectra. The alteration of surface composition may also play a role in camouflaging links between dynamical class and composition (Gil-Hutton 2002). This is more likely on Centaurs, which experience much higher temperatures and fluxes of solar UV and charged particles than the more distant TNOs.

Multi-filter photometry has been used to study the composition of relatively large samples of TNOs; it has revealed some correlation between optical colors and size (e.g., Fraser & Brown 2012; Peixinho et al. 2015), as well as between color and orbital inclination in the classical population (e.g., Doressoundiram et al. 2002; Trujillo & Brown 2002; Marsset et al. 2020). Thermal data also revealed that the cold classical objects also generally have higher albedos than the hot classical objects (Brucker et al. 2009; Lacerda et al. 2014; Vilenius et al. 2014). Near-IR colors potentially offer better discrimination of composition, but only $\sim 25\%$ of all ground-based data for TNOs are at these wavelengths (i.e., from $\lambda \sim 1$ to $\sim 2.5 \mu\text{m}$; e.g., Hainaut et al. 2012). Fraser & Brown (2012) and Fraser et al. (2015) reported on the visible and NIR observations of 100 small TNOs and Centaurs using the Hubble WFC3, finding two clusters in visible versus near-IR color, as well as evidence of ubiquitous H_2O ice. To date, spectra of various quality have been collected for only about 75 TNOs and Centaurs total (e.g., Barkume et al. 2008; Brown 2008; Barucci et al. 2011; Barucci & Merlin 2020, and references therein). Based on those data, it appears that H_2O is the most common ice detected on TNOs’ surfaces.

These past studies have achieved limited success, in part because they are limited by the sensitivity of ground-based facilities, and in part because only the relatively weak near-IR bands of the components of interest could be studied. The ices and complex organics (sometimes we also simply refer to the latter as organics) that we expect to find on TNOs and Centaurs have their fundamental absorption bands beyond $2.2 \mu\text{m}$, necessitating space-based observations due to the atmospheric interference and low brightness presented by this populations. Here, we summarize a collection of 3.6 and $4.5 \mu\text{m}$ observations of TNOs made with the Infrared Array Camera (IRAC; Fazio et al. 2004), on the Spitzer Space Observatory (hereafter, Spitzer). These data are consistent with absorption bands due to H_2O , organic tholins, and volatile ices, as well as the presence of silicates. They also reveal the range of geometric albedos of TNOs at 3– $5 \mu\text{m}$, which will be important for planning observations at those wavelengths using the James Webb Space Telescope (JWST). In principle, JWST can provide high-quality spectra for hundreds of TNOs from 1 to $5 \mu\text{m}$.

2. Spitzer/IRAC observations and Data Reduction

Spitzer, with an aperture of 85 cm, was launched in 2003 August into an Earth-trailing, heliocentric orbit (Werner et al. 2004). Its Infrared Array Camera (IRAC), a broadband imager with four channels, has a field of view (FoV) of 5.2×5.2 and an image scale of $\sim 1.2 \text{ arcsec pixel}^{-1}$ (Fazio et al. 2004). The four broadband channels are centered at 3.6, 4.5, 5.8, and $8.0 \mu\text{m}$, with full width at half maximum of 0.68, 0.87, 1.25,

and $2.52 \mu\text{m}$, respectively. Spitzer’s instruments were originally cooled by liquid helium, but this cryogen was exhausted in 2009 May. Thereafter, Spitzer entered its so-called “warm mission,” during which only the 3.6 and $4.5 \mu\text{m}$ channels of IRAC have been operational.

From 2005 to 2016, we observed TNOs and Centaurs during different Spitzer observational cycles,¹³ and included all dynamical classes. In this work, we present the results from a subsample that includes detached, classical, and resonant types (see Section 3.1). Data are available for download from the Spitzer Heritage Archive.¹⁴ Even though some objects were observed in 5.8 and $8.0 \mu\text{m}$, only the 3.6 and $4.5 \mu\text{m}$ data are reported and analyzed here. Note that, for these cold ($\sim 40 \text{ K}$) and distant (beyond 30 au) objects, the flux at these wavelengths is only reflected light, with no thermal emission from their surfaces. A summary of observations is provided in Table C1, which includes: object designation, date of observation, Spitzer-object distance (Δ), heliocentric distance (r_H), phase angle (α), flux at 3.6 and $4.5 \mu\text{m}$ ($F_{3.6}$, and $F_{4.5}$, respectively), and geometric albedo at 3.6 and $4.5 \mu\text{m}$ ($p_{3.6}$ and $p_{4.5}$, respectively).

Each object was observed twice, with time intervals between several hours to several days, with the aim of having two different measurements at different locations relative to the background star fields, while keeping the object within the same FoV (movement of the object was around $30''$). This provides several benefits: identification of the object by its motion against background stars, straightforward and accurate background subtraction, and increased probability of at least one good measurement in the case of a field star obscuring the object (Emery et al. 2007). Each observation consists of nine or more dithered frames, which allows image correction for effects such as bad pixels, latent images from previous observations, and stray light from bright objects in or just off the frame.

IRAC data frames were pre-processed by the Spitzer Science Center (SSC) automated pipeline for dark, bias, and flat-field corrections, as well as flux calibrations. Corrections for IRAC-specific artifacts such as column and array pulldown, muxbleeding, and stray light contamination, were done for individual frames, if necessary. The two observations per object were used as background frames for each other in order to remove diffuse flux and most of the contribution from stars in the field. Corrections (available from the SSC) for pixel solid angle variations and array location dependent photometric variations were applied to the frames.

We performed synthetic aperture photometry in order to calculate the flux from the object, as outlined in the IRAC Instrument Handbook.¹⁵ We used four combinations of aperture radius and background annulus as shown in Table 1 (Emery et al. 2007). Aperture corrections for each combination are given in the IRAC Instrument Handbook. Color corrections are calculated for each broadband channel assuming a solar spectral slope through each passband (Smith & Gottlieb 1974). All aperture/annulus combinations and all frames in an observation are averaged together for each channel and recorded as final fluxes. Uncertainties of 1σ are reported. The uncertainties account for photon counting statistics, deviation

¹³ Specifically GO2, GO4, GO6, GO7, GO8, and GO12 cycles, with program IDs 20769, 40389, 60155, 70115, 80116, and 12012, respectively.

¹⁴ <http://sha.ipac.caltech.edu/applications/Spitzer/SHA/>

¹⁵ <http://irsa.ipac.caltech.edu/data/SPITZER/docs/spitzermission/>

Table 1
Parameters Used to Perform the Synthetic Aperture Photometry

Aperture (pix)	Annul Radius (pix)	Annul Width (pix)
2	2	4
2	10	10
3	3	4
3	10	10

among the dithered frames, and deviation among the aperture/annulus combinations. The absolute calibration of all IRAC channels is accurate to $\sim 3\%$ (Reach et al. 2005).

A visual inspection of each frame, the average frame, and the background-subtracted frame for each observation was conducted in order to assess the success of the observation. If objects were not discernible by eye in the observation, an upper limit calculated from the background flux is presented. The background flux is the mean of the repeated aperture photometry process for 50 random center points, removing outliers outside $\pm 2\sigma$, within a radius of 50 pixels of the location of the object predicted by its ephemeris.

With the aim of ensuring that our measurements are reliable, the objects had to satisfy the following criteria in order to be selected for the final analysis:

1. Not contaminated by a background star or image artifact.
2. Clearly visible in the average frames.
3. Greater than 3σ detection.

For any objects selected for final analysis that have $< 3\sigma$ detection, we used a 3σ upper limit calculated from the background flux. From the total sample, 100 objects satisfied these criteria and were analyzed in this work. All measured fluxes with errors are provided in Table C1.

3. Supporting Data

3.1. Dynamical Classification

The dynamical classes of the objects in the sample, which are included in Table C2, were determined using the numerical procedure detailed in Gladman et al. (2008).

These classifications are categorized as either secure or insecure. Given the observed on-sky location of each TNO over time, we find the best-fit orbit as well as the highest- and lowest-semimajor axis orbits that are consistent with the observations.¹⁶ These three orbits are used as starting points for 100 Myr numerical simulations. If all three “clones” show the same orbital behavior in these simulations, the classification is considered secure. If not, it is insecure and additional future observations are still required to establish the classification; in this case, we give the best-fit classification.

Each of the dynamical classifications are designed to capture orbital behavioral characteristics, particularly to describe the manner in which each TNO is (or is not) interacting with Neptune. TNOs that are experiencing active gravitational

¹⁶ For each candidate orbit, we consider the deviation between the predicted position from that orbit versus the observed astrometry. To be consistent with observations, the worst predicted versus observed astrometric position must be no more than 1.5 times the worst from the best-fit orbit, and the root mean square of these deviations must be no more than 1.5 times that of the best fit. The selected extremal orbits are then those with the lowest and highest semimajor axes.

scattering by Neptune are classified as *scattering* objects; we consider a TNO to be scattering if the semimajor axis changes by > 1.5 au over the 100 Myr simulation. *Resonant* objects are TNOs in mean-motion resonance with Neptune (resonance with Uranus are searched for, but are only known for Centaurs). We diagnose resonance by determining if a resonant angle is librating as opposed to circulating; see Gladman et al. (2008) and Khain et al. (2018) for more details. TNOs that are not strongly interacting with Neptune are classified as either *detached* or *classical* objects; if the TNO is not scattering or resonant and has an initial eccentricity above 0.24, then it is called “detached.” Otherwise, it is considered “classical.” Classical objects are then subdivided, based on their position relative to two major TNO resonances, as *inner* ($a < 39.4$ au, where the 3:2 resonance is located), *main* ($39.4 < a < 47.0$ au), and *outer* ($a > 47.0$ au). Orbital inclination i is not part of the dynamical classification, because the TNO i structure is complex (varying with a) and causes confusion if an overly simplistic i cut is used. In particular, modern understanding shows that the so-called “cold” component (Brown 2001) appears to be present only in the main classical belt between $42.5 < a < 47.0$ au (Petit et al. 2011). Therefore, it should be located by using free inclinations i_{free} corrected for secular effects and thus measured with respect to the local Laplace pole. Van Laerhoven et al. (2019) show that the cold component then has an impressively small “inclination width” of $< 2^\circ$, and that in the main belt, choosing objects with $i_{\text{free}} < 4^\circ$ gives a reasonable separation, where the majority of the objects on either side of this boundary belong to only one of the two otherwise overlapping hot and cold components. At other semimajor axes, the “cold classical” component appears not to exist and objects with low inclinations are simply the low- i tail of the hot component.

In this manuscript, we analyzed those that did not have or are not having planetary encounters. In other words, we excluded scattering objects, which will be analyzed separately along with Centaurs in a future paper. In summary, from the 100 objects that satisfied the criteria from the above section: 40 are hot classical, 4 are cold classical, 41 are resonant, and 15 are detached.

3.2. Albedos and Diameters

Different physical properties were used for our albedo calculations (see Section 5). Radii and visible geometric albedos were compiled from the database of the “TNOs Are Cool” project¹⁷ (Müller et al. 2009), which is, to date, the most complete and accurate database of these properties for TNOs (Müller et al. 2020). Figure 1 shows diameters and albedos for resonant objects (green squares), detached objects (turquoise triangles), and hot and cold classical objects (pink stars and blue circles, respectively). The “TNOs Are Cool” sample is shown in gray circles. To maintain consistency, we also adopted the corresponding absolute magnitudes used in the “TNOs Are Cool” project.

Not all our objects were observed by the “TNOs Are Cool” project; in those instances, we used $11 \pm 9\%$, the median albedo calculated from the “TNOs Are Cool” database. Coupled with the absolute magnitude specified by the Minor Planet Center (MPC), we calculate the radius (R) using the

¹⁷ <http://public-tnoarecool.lesia.obspm.fr>

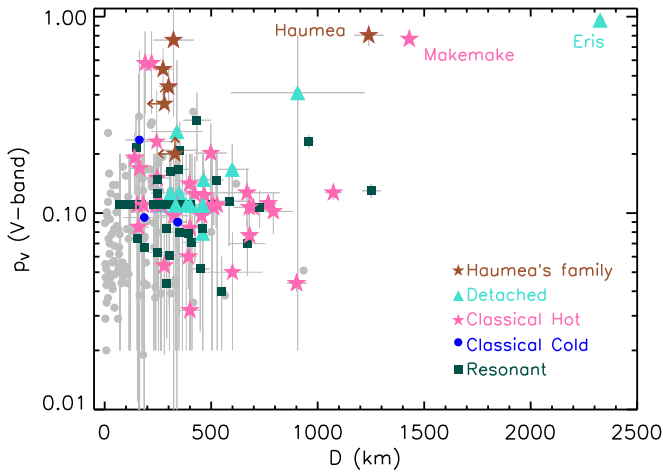


Figure 1. Diameter vs. geometric albedo in V band from the “TNOs Are Cool” sample (gray circles). Colored symbols denote objects of our sample (note that some of them have diameters assuming the median albedo calculated from Müller et al. 2020). Green squares show resonant objects, turquoise triangles show detached objects, pink stars and blue circles represent hot and cold classical objects, respectively. Brown stars represent Haumea’s family members, and brown arrows indicate lower and upper limits for the albedo and the diameter, respectively (Brown et al. 2007b; Snodgrass et al. 2010). Only dwarf planets and Haumea’s family members have albedos over 40%, which belong to detached and hot classical groups. The remaining objects have albedos under 40%.

equation:

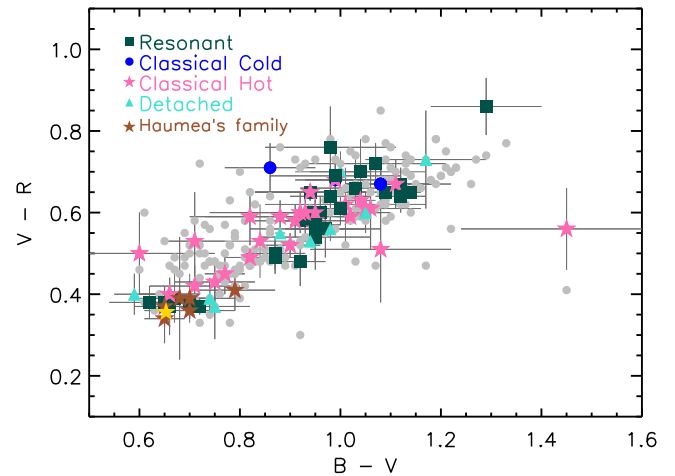
$$R = C p^{-1/2} 10^{-H/5}, \quad (1)$$

where C is a constant depending on the observed wavelength (i.e., 1329 km for V band), and p and H are the geometric albedo and the absolute magnitude of the object in the same photometric band, respectively. The same procedure was also applied to three Haumea family members that only have upper limits in their V -band albedos (Vilenius et al. 2018), specifically, 1995 SM₅₅, 1996 TO₆₆, and 1999 CD₁₅₈. For these three objects, we calculated a median value using the albedos from Haumea family members ($p_{V,Haumea} = 0.58 \pm 0.26$), as the median value for the TNO population is not representative of the family. Table C2 shows a compilation of the physical properties used in this work.

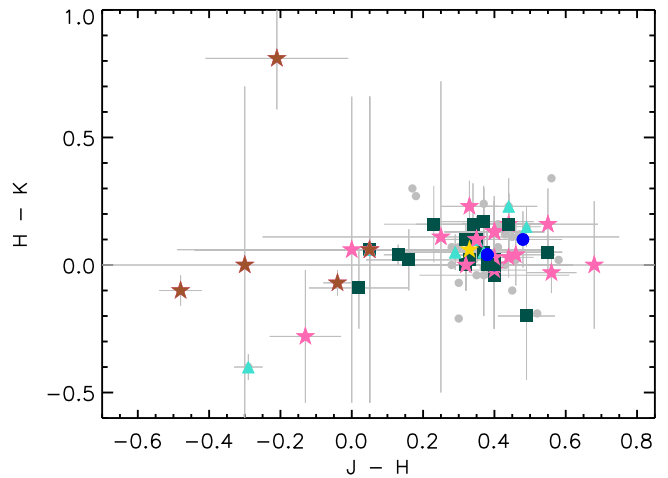
3.3. Visible and Near-infrared Photometric Data

Ground-based observations for VNIR photometric data were compiled from published literature using the following process:

1. Visible colors were taken from Peixinho et al. (2015), and near-infrared (NIR) colors from Fulchignoni et al. (2008), with some of the NIR colors completed using data from Belskaya et al. (2015), MBOSS, and Tegler et al. (2016), among others (see Table C3).
2. For objects with no color available in the above references, we used the average colors published by Fulchignoni et al. (2008) as a function of their taxonomy (given in Belskaya et al. 2015).
3. Some exceptions were made during the process: Because the NIR colors available in the literature for Makemake and Quaoar have very large errors, we decided to extract their colors using VNIR spectra published in the literature. We also used the measured spectrum of 2002



(a)



(b)

Figure 2. (a) $B - V$ vs. $V - R$ color-color plot for our sample using colors and symbols to represent different populations. Gray circles represent data from Peixinho et al. (2015). (b) $J - H$ vs. $H - K$ color-color plot for our sample using colors and symbols to represent different populations. Gray circles represent the sample from Fulchignoni et al. (2008). In both panels, the same scale as in Doressoundiram et al. (2008) was used in order to compare the diversity of our sample: green squares show resonant objects, triangles show detached objects, and pink stars and blue circles represent hot and cold classical objects, respectively. Solar colors are indicated by a yellow star.

TX₃₀₀ (Licandro et al. 2006a) and synthesized its NIR colors because they are unavailable in the literature.

As can be seen in Figure 2, our sample exhibits the full diversity of colors reported by different surveys (e.g., Barucci et al. 1999; Delsanti et al. 2001, 2004, 2006; Doressoundiram et al. 2001, 2002, 2005, 2007; Boehnhardt et al. 2002; DeMeo et al. 2009; Perna et al. 2010). Table C3 provides a compilation of colors for our sample. The reference for each object and any exceptions to the process to select the reference are included in the table.

3.4. Spectroscopic Data

Spectra were also compiled as a baseline to understand our sample and to assess whether our compilation of colors that are

translated to spectrophotometric measurements (i.e., geometric albedo versus wavelength) are in agreement with the spectra. We followed the work performed by Barucci et al. (2011) regarding surface composition of TNOs using VNIR spectra. We used this work as a reference for detection of water and other ices because it provides a homogeneous analysis of spectra for at least some of our targets. However, because this review was published eight years ago, we also searched into more recent papers in order to find spectra published for other objects.

Although we have not performed any calculation to measure bands, we followed the criteria of Barucci et al. (2011), in which three categories are defined: objects with clear detection of absorption bands reported by the authors are considered “sure detections,” objects with some indications of absorption bands reported by the authors are considered “tentative detections,” and objects with no indications of absorption bands reported by the authors are considered “no detections.”

We cite literature regarding the spectra used in this work in Sections 5 and 7, where each object is independently analyzed. In general, there is good agreement for the whole sample, as demonstrated in Appendix B. There exist only five exceptions in which the spectrum and the spectrophotometric measurements do not completely agree (discussed in Section 6).

4. Reflectance and Color Indices

4.1. Reflectance

Fluxes in the IRAC wavelengths are converted into geometric albedos in order to be combined with ground-based data and to plot as spectrophotometric measurements. The geometric albedo (p_λ) at wavelength λ is given as follows:

$$p_\lambda = \frac{F_\lambda r_H^2 \Delta^2}{F_{\odot,\lambda} \Phi R^2}, \quad (2)$$

where F_λ is the measured flux at wavelength λ , $F_{\odot,\lambda}$ is the solar flux at 1 au at the same wavelength, r_H is the heliocentric distance in au, Δ is the Spitzer-centric distances in km, R is the radius of the object in km, and Φ is the phase correction factor. We have calculated the phase correction factor by $\Phi = 10^{-\frac{\beta\alpha}{2.5}}$; where α is the phase angle with respect to Spitzer, and $\beta = 0.14_{-0.03}^{+0.07}$ mag deg⁻¹ is the median of phase coefficients tabulated by Alvarez-Candal et al. (2016), where we have excluded values that are negative or greater than 0.5, as these are likely due to uncharacterized rotational light-curve effects.¹⁸

Colors from the literature were also converted into geometric albedo by means of the equation:

$$p_R = p_V 10^{\frac{(V-R)-(V-R)_\odot}{2.5}}, \quad (3)$$

where p_R is the albedo in R band, p_V is the albedo in V band, $(V - R)$ is the color of the object, and $(V - R)_\odot$ is the color of the Sun. Analogous relations are used for the other colors, in our particular case: $(B - V)$, $(V - I)$, $(V - J)$, $(V - H)$, and $(V - K)$. As a result, spectrophotometric measurements have been incorporated for each object (see Appendix B), allowing

us to analyze the surface composition using the widest possible wavelength range (see Section 5).

Note that, from Equation (2), the IRAC albedo depends on the radius R explicitly, and therefore, one may expect that the large relative uncertainties in the measurements of the radii of known objects would translate into large relative uncertainties in the IRAC albedos. However, Equation (1) provides a workaround, as one can check explicitly that combining both Equations (2) and (1) results in an expression for the ratio of the ground-based V -band geometric albedo and IRAC albedo, p_V/p_λ , that does not depend explicitly on the radius R nor p_V (in other words, in the resulting combined equation, only the relative albedo plays a role). Hence, if one focuses on the relative albedos (i.e., on the absorption), the effect of large uncertainties in R is neutralized—provided, of course, that R and p_V are constrained to satisfy Equation (1). Table 2 shows median and average values for the geometric albedos at 3.6 and 4.5 μm of our sample, while Tables C1 and C4 show the geometric albedos obtained for each object at IRAC and VNIR wavelengths, respectively. Note that measurements at 3.6 and 4.5 μm were taken consecutively, one after the other. The total exposure times (including all subexposures) were no longer than 40 minutes at 3.6 μm . Considering that the fastest rotation period for a TNO known to date is 4 hr (Haumea), with a median value of ~ 8 hr (Thirouin et al. 2012), large effects due to rotational variability between both filters are very unlikely.

4.2. Color Indices

In order to combine our IRAC/Spitzer measurements with existing apparent magnitude measurements at shorter wavelengths, we define colors, expressed as magnitude differences, as:

$$\begin{aligned} m_1 - m_2 &= -2.5 \log \left(\frac{F_1/S_1}{F_2/S_2} \right) \\ &= -2.5 \log \left(\frac{F_1}{F_2} \right) + 2.5 \log \left(\frac{S_1}{S_2} \right), \end{aligned}$$

where F_n is the flux from the target in a given band and S_n is the solar flux in that band (with $n = 1, 2$). In what follows, we denote these colors as “ $V - 3.6 \mu\text{m}$,” “ $J - 3.6 \mu\text{m}$,” “ $K - 3.6 \mu\text{m}$,” and “ $3.6 \mu\text{m} - 4.5 \mu\text{m}$.” Because these colors are corrected for the intrinsic solar color, they can be related to the albedos in the bands, for example:

$$3.6 \mu\text{m} - 4.5 \mu\text{m} = -2.5 \log \frac{p_{3.6}}{p_{4.5}}, \quad (4)$$

where $3.6 \mu\text{m} - 4.5 \mu\text{m}$ is the color from IRAC/Spitzer measurements, $p_{3.6}$ is the geometric albedo at 3.6 μm , and $p_{4.5}$ is the geometric albedo at 4.5 μm . Other colors using IRAC/Spitzer broadband and ground-based measurements can be obtained using the same equation. Table C5 shows a compilation of the different colors used in the analysis.

5. Results

Below, we present our results in two ways: (1) by comparing the color indices that we have measured to color indices computed from synthetic reflectance models for pure substances and binary and trinary mixtures of those substances;

¹⁸ The median value using the complete sample was $\beta = 0.1 \pm 0.1$ mag deg⁻¹, which produces an error of the same order of magnitude as the β value; for that reason, outliers were excluded first.

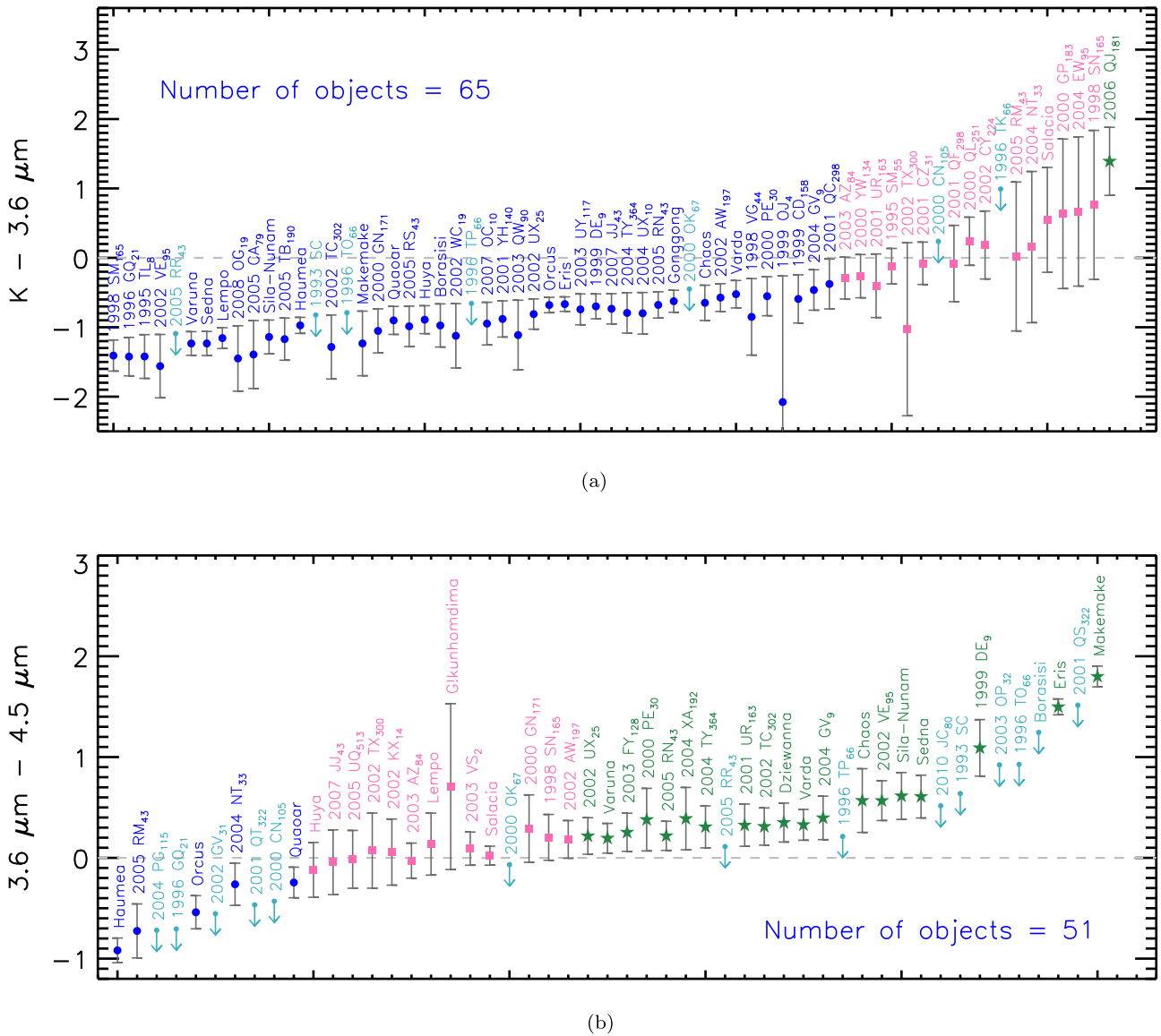


Figure 3. K -band vs. IRAC color indices for our entire sample, plotted in order of increasing color index. Negative (positive) values indicate absorption in the longer (shorter) wavelength; zero indicates neutral (i.e., solar) colors (horizontal dashed line). Note that not all the objects of our sample presented measurements at $4.5 \mu\text{m}$ or published data in the K band, which drops the number of objects to 65 and 51 for $K - 3.6 \mu\text{m}$ (upper panel) and $3.6 \mu\text{m} - 4.5 \mu\text{m}$ (bottom panel), respectively. There are also a few objects that have only upper limits in both IRAC bands, so those are also not plotted in the bottom panel. Error bars give 1σ uncertainties while arrows give 3σ upper limits. Objects with a 1σ independent probability of presenting absorption at $3.6 \mu\text{m}$ (upper panel) and $4.5 \mu\text{m}$ (bottom panel) are represented by blue circles and are labeled in blue. Objects with a 1σ independent probability of presenting no absorption are plotted as green stars and labeled in green. Objects with error bars that overlap both regions are represented by pink squares and labeled in pink. Objects for which upper limits have been determined are represented by turquoise arrows and are labeled in turquoise. The range of TNO colors in these bands ($\gtrsim 2$ mag) significantly exceeds that seen in the visible ($\lesssim 1$ mag; see Figure 2 and, e.g., Peixinho et al. 2015; Schwamb et al. 2019).

Table 2
Median and Average Values for the Geometric Albedos and Colors Obtained in This Work

	$p_{3.6}$	$p_{4.5}$	$3.6 \mu\text{m} - 4.5 \mu\text{m}$ (mag)	$V - 3.6 \mu\text{m}$ (mag)	$J - 3.6 \mu\text{m}$ (mag)	$K - 3.6 \mu\text{m}$ (mag)
Median	0.12 ± 0.01	0.15 ± 0.03	0.2 ± 0.1	0.0 ± 0.1	-0.9 ± 0.1	-0.9 ± 0.1
Average	0.16 ± 0.05	0.21 ± 0.05	0.3 ± 0.2	0.1 ± 1.0	-0.7 ± 0.3	-0.8 ± 0.6

Note. Abbreviations are defined as follows: geometric albedo at 3.6 and $4.5 \mu\text{m}$ ($p_{3.6}$, $p_{4.5}$, respectively).

and (2) by presenting the measured reflectance spectra (i.e., spectrophotometric measurements) of all objects, along with measured visible–near-IR spectra found in the literature, or spectral models if available (see Appendix B).

5.1. Measured Colors and Synthetic Spectra

Figure 3 shows the measured K versus IRAC color indices for all of our targets. Note that not all objects of our sample presented measurements at $4.5 \mu\text{m}$ or published data in the

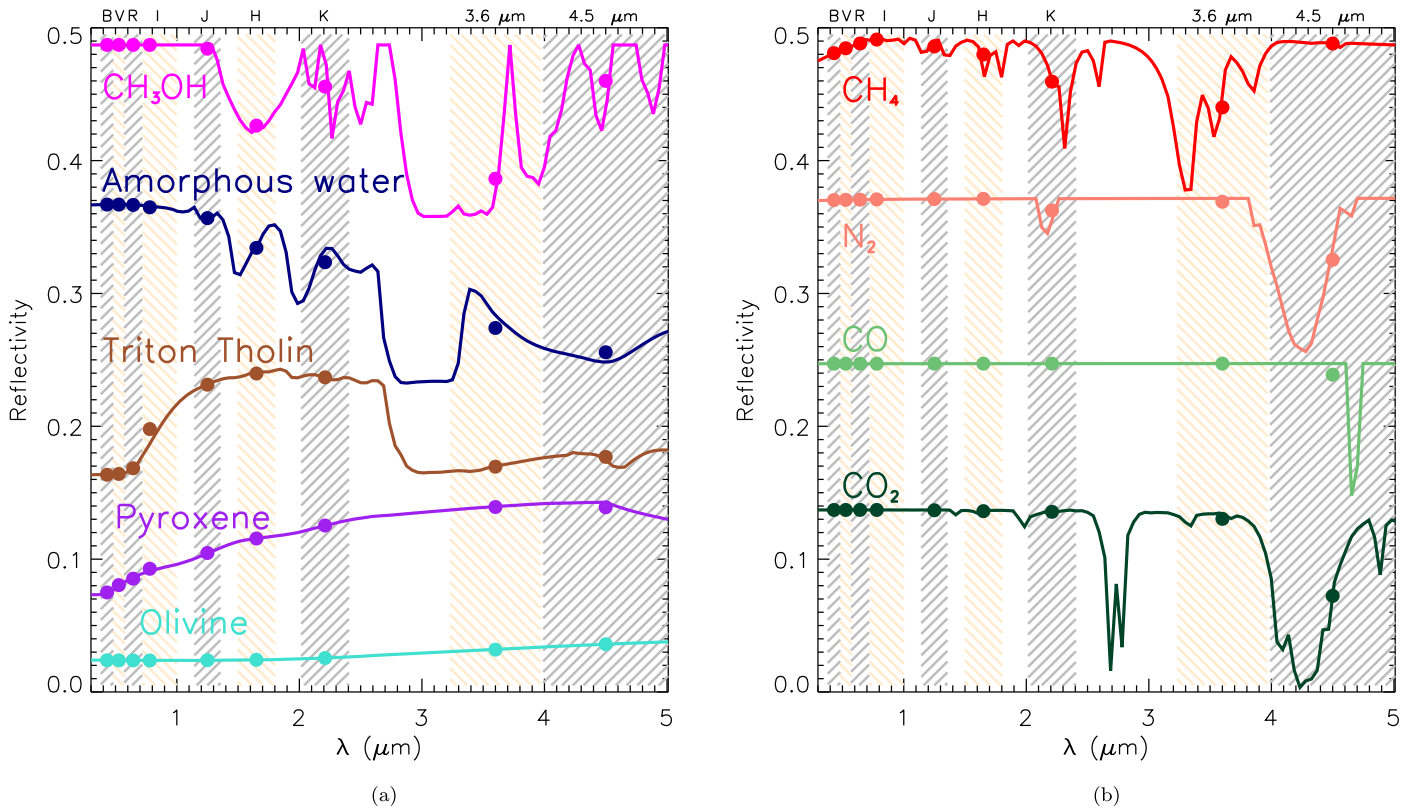


Figure 4. Synthetic reflectance spectra of some pure materials expected or known to exist on the surfaces of small TNOs and Centaurs (left), and additional molecular ices found on TNO dwarf planets (right). The particle size was $10\ \mu\text{m}$ for all materials except for N_2 , where the particle size is $10\ \text{cm}$. Vertical gray and brown shaded bars indicate VNIR and IRAC/Spitzer filter bands, as labeled along the top axis. Bandwidth here is the full width of the band at 50% of the average in-band transmission. Dots represent the spectrophotometric measurements as given by the convolution of each synthetic spectrum with the filters. For clarity, reflectance has been shifted by arbitrary offsets as follows: olivine (0.02), pyroxene (0.07), Triton tholin (0.16), amorphous H_2O (0.23), CH_3OH (0.35), CH_4 (0.355), N_2 (0.235), CO (0.11), and CO_2 (no offset).

K band, which drops the number of objects to 65 and 51 for $K - 3.6\ \mu\text{m}$ and $3.6\ \mu\text{m} - 4.5\ \mu\text{m}$, respectively. From the upper panel in Figure 3, we see that, from the 65 objects with $K - 3.6\ \mu\text{m}$, 48 present a 1σ independent probability of having an absorption at $3.6\ \mu\text{m}$ (74% of the sample), with 44 objects representing the 1σ compound probability (i.e., 68%). Only one object presents a 1σ independent probability of not having absorption at $3.6\ \mu\text{m}$, with two objects representing the 1σ compound probability (i.e., 3%). Additionally, and as shown in the bottom panel, with a total of 51 objects, 11 objects present a 1σ independent probability of having an absorption at $3.6\ \mu\text{m}$ (22% of the sample), with the same number of objects representing the 1σ compound probability. From both panels, we can appreciate that the range of colors is significantly larger than seen in the visible–near-IR wavelengths (e.g., Fulchignoni et al. 2008; Peixinho et al. 2015; Schwamb et al. 2019), suggesting the potential of using the IRAC colors to constrain TNO composition in ways that have previously been impossible. Figure 4 shows synthetic spectral models for some materials typically found, or expected to be present, on TNOs and Centaurs. The figure illustrates how much stronger the absorption bands of most of these materials are at the IRAC wavelengths than in the near-IR. This is because the longer-wavelength absorptions are associated with fundamental molecular vibration frequencies, while those shortward of $2.5\ \mu\text{m}$ are weaker overtone bands, which explains the strong color diversity of TNOs seen in Figure 3. Other colors are also important for constraining composition, and they help establish

continuum levels (particularly true for the J , H , and K bands). In addition to the colors discussed above, we also use $V - 3.6\ \mu\text{m}$ and $J - 3.6\ \mu\text{m}$ colors in the following analysis. Table C5 shows our compilation of all the colors for our targets (including the aforementioned and VNIR colors) used in this work.

5.2. Spectrophotometric Measurements

We plot our compilation of visible–near-IR and IRAC spectrophotometric measurements for each object, in terms of geometric albedo, in Appendix B. The measurements were converted to albedo as described in Section 4. When a previously published visible–near-IR spectrum of an object is available, it is also plotted, in order to allow comparison to our IRAC results. The figures are ordered by provisional designation in ascending order, followed by named objects in alphabetical order in our sample. The albedo spectra are shown for all objects, regardless of whether we found J - and/or K -band photometry in the literature. However, the objects lacking those measurements are excluded from the color index analysis we present below.

Inspecting each albedo spectrum in Appendix B, we found that seven of our objects do not show absorption at 3.6 and $4.5\ \mu\text{m}$ with respect to the K -band. Referencing Figure 4, it seems plausible that such objects have surfaces dominated by amorphous silicates. Those objects are: 1998 SN₁₆₅, 2000 GP₁₈₃, 2000 QL₂₅₁, 2002 CY₂₂₄, 2004 EW₉₅, 2006 QJ₁₈₁, and Salacia, all of which have positive $K - 3.6\ \mu\text{m}$ colors in

Table 3
References of the Optical Constants for the Synthetic Models Used in This Work

Model	Temperature (K)/Phase	Reference
CH ₃ OH	90	Robert Brown ^a
CH ₄	40	Grundy et al. (2002)
N ₂	21	Quirico & Schmitt (1997)
CO	21	Quirico & Schmitt (1997)
CO ₂	150	Hansen (1997)
H ₂ O	120 amorphous	Mastrapa et al. (2009)
H ₂ O	150 crystalline	Mastrapa et al. (2009)
Triton Tholin	Not available	Imanaka et al. (2012)
Titan Tholin	≈290	Khare et al. (1984)
Pyroxene 5: Mg _{0.7} Fe _{0.3} SiO ₃	Amorphous	Dorschner et al. (1995)
Pyroxene 8: Mg _{0.4} Fe _{0.6} SiO ₃	Amorphous	Dorschner et al. (1995)
Olivine 1	Amorphous	Dorschner et al. (1995)
Olivine 2	Amorphous	Dorschner et al. (1995)

Note.

^a See Appendix in Cruikshank et al. (1998).

Figure 3. The remaining objects have absorption identification in at least one of the two IRAC/Spitzer bands. These absorption identifications are related to either ices (H₂O, CH₄, CH₃OH,...) or complex organics, as explained below.

6. Analysis

6.1. Synthetic Color Indices

In order to interpret the colors of our objects in terms of composition, we computed synthetic spectral models for the substances shown in Figure 4 and Table 3, using a range of grain sizes for each component. We convolved the synthetic spectral models with the Johnson–Cousins–Bessell standard filter system (Johnson 1964; Bessell & Brett 1988; Bessell 2005) and the IRAC broadbands (Fazio et al. 2004), to derive synthetic photometry and colors for the synthetic spectra. Figure 5 illustrates the results for the $K - 3.6 \mu\text{m}$ and $3.6 \mu\text{m} - 4.5 \mu\text{m}$ color indices (circles) for the pure materials as a color–color diagram. There are distinct regions that can be attributed to most of the materials we consider, with the color versus grain-size trends extending approximately radially in different directions from the origin for each material. Because of this layout, we informally call this diagram the “compositional clock.” While most of the materials result in color trends at different “times” on the clock, CO₂, CO, and N₂ occupy nearly the same region (for clarity within the diagram, we did not represent the N₂ in Figure 5), although for a given color, the relevant grain size would be orders of magnitude larger for CO or N₂ than for CO₂. While the trends for these pure materials are simple, minor changes to the model assumptions, such as having a distribution of grain sizes or mixtures of different materials complicate these trends. In order to plot the region of influence for each pure material, we have applied the K -nearest neighbors (KNN) method (Hastie et al. 2001; James et al. 2013), as implemented in `scikit learn` (Pedregosa et al. 2011), with $K = 15$, and assigning weights proportional to the inverse of the distance from the query point. The method will classify each coordinate in the graphic considering the 15 nearest points provided by the models, filling the empty regions of the diagram. The selection of K was made via inspection of the results provided by different values. Small values of K will be too malleable, leading to unstable decision boundaries, and large values of K will have smoother decision boundaries, which

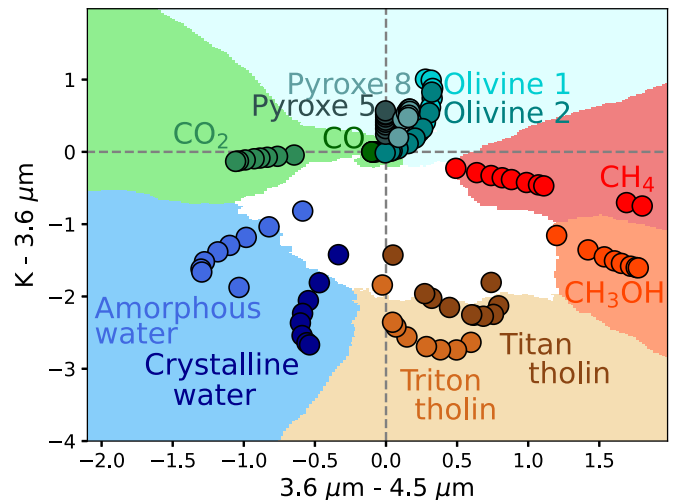


Figure 5. An illustration of the “compositional clock,” a color–color diagram for $K - 3.6 \mu\text{m}$ vs. $3.6 \mu\text{m} - 4.5 \mu\text{m}$ synthetic colors for pure materials (each plotted with a different color and symbol, and labeled). Colors were synthesized from spectral models using grain sizes from 10 to 100 μm in 10 μm increments (CH₄ also included 400 and 500 μm). The larger the grain, the deeper the absorption band produced, and therefore grains of 10 μm are nearest to the origin of the plot.

mean lower variance but increased bias (as well as greater computational expense). A good estimation is made from the square root of the total number of models (in our case, we have 207 points of synthetic materials, i.e., $K \sim 15$). We inspected values of K between 10 and 25, which produced similar results, and therefore we chose 15 as a good compromise. Each colored region is dominated by a different material (water, complex organics, methanol, methane, silicates, and supervolatiles—CO and CO₂), while the white region is dominated by different mixtures of those materials, as explained below.

Surfaces of TNOs are very unlikely to be dominated by pure materials, so we now explore synthetic colors for intimate combinations between spectral models for three of our representative components (i.e., olivine 1, Triton tholin, and amorphous H₂O), with each component having a single grain size. The intimate mixtures have been carried out using Hapke scattering models (Hapke & Wells 1981; Hapke 1993). The results are shown in Figure 6 for mixing between each pair of

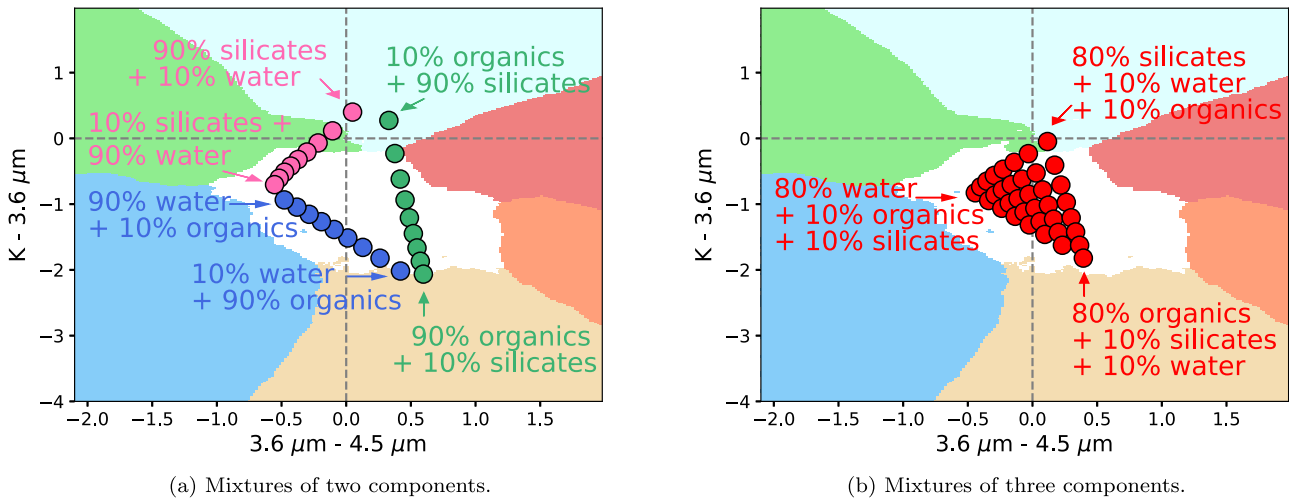


Figure 6. Same color–color space as in Figure 5, but showing trends for intimate mixing between two (left, panel a) and three (right, panel b) components. Here, we have chosen amorphous H₂O ice, Triton tholin, and olivine 1 as representative materials, and we show only the 10 μm grain-size results. Models including crystalline and amorphous H₂O have similar relative positions in the diagram. For comparison, we plotted the same colored regions as in Figure 5, to indicate those regions dominated by pure materials.

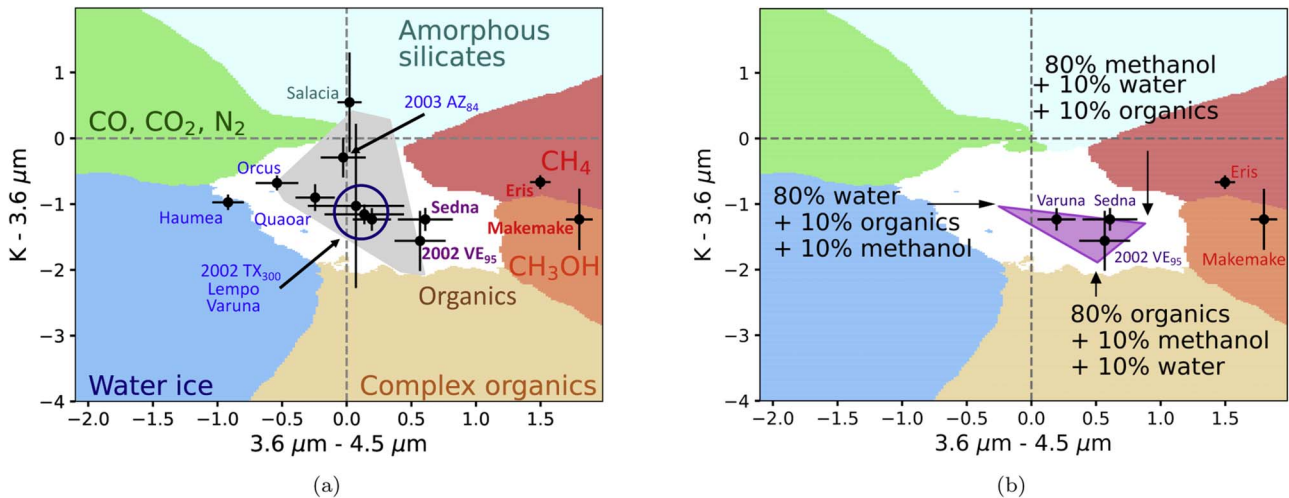


Figure 7. Color–color diagram, similar to Figure 5, including the shaded regions for pure materials, and with measured colors of 12 TNOs with relatively well-characterized compositions from VNIR spectroscopic observations. Left: Target names are given in colors indicating whether the spectrum has previously been characterized as having H₂O (blue), CH₄ (red), or CH₃OH (purple). Silicates (turquoise) have not been detected in Salacia. However, its flat spectrum and low albedo are consistent with our results, shown in this diagram, indicating a surface composition dominated by silicates. Gray polygon is bounding the regions shown in Figure 6 for binary and ternary models of H₂O, Olivine 1, and Triton tholin (i.e., H₂O, silicates, and organics). Right: colors for Varuna, Sedna, and 2002 VE₉₅ are compared to ternary mixing models of amorphous H₂O, Triton tholin, and CH₃OH with grain sizes of 10 μm.

components (a) and between all three components (b). If additional combinations of grain sizes and/or mixtures between more than three components are considered, the region covered in the color–color diagram would expand but still be bounded by the colors of the pure components. The figure shows that surfaces with significant fractions of multiple components can have colors that deviate from the trends seen for the pure materials in Figure 5. However, it also illustrates that the colors for such surfaces are still confined to certain regions of the diagram, and therefore can constrain the composition in useful ways and exclude the presence of some components.

6.2. Compositional Interpretation of the TNO Colors

In order to explore the utility of the synthetic colors and color–color diagram discussed above, we now plot the measured colors for our targets and include the composition

regions and color trends shown in Figures 5 and 6. To start, we focus on 12 objects with relatively well-understood spectral properties, shown in Figure 7(a). (Albedo spectra for these objects are given in Appendix B.) Fortunately, the colors of these objects span much of the color–color diagram, providing a fairly complete sample for testing the predictions based on the compositional-clock approach. The colors of all 12 objects appear to be roughly consistent with the predictions based on synthetic colors for the pure substances and simple mixtures between those substances. To obtain the proportion of each material for each object, we have implemented an interpolation routine that uses the KNN method (Hastie et al. 2001; James et al. 2013). For each object (or observational point), we calculate the Euclidean distance to search for the K-nearest points given by the synthetic models. The selection of K was made following the same procedure explained in Section 6.1, which led to $K = 15$. Next, we average the different proportion

of each material for each point to provide an interpolation for each object. To calculate the errors in the proportions, we obtained the uppermost and lowest value of each of the two colors, considering their error bars. This provides four new points for each object (these are arranged in the form of a cross around the central value). We applied the K-nearest method to calculate the proportion of different materials for each of those four new points. We obtained the difference between the proportion of each material given for the object and the proportion of each material given the four new points. For a more conservative perspective, we chose as the error the biggest difference from those obtained from opposite points in the cross shape.

Haumea plots squarely in the H₂O-ice pure region, as expected based on previous studies (e.g., Merlin et al. 2007; Trujillo et al. 2007; Pinilla-Alonso et al. 2009). We obtain a composition of $80 \pm 5\%$ H₂O, $10 \pm 10\%$ silicates, $10 \pm 10\%$ organics.

Quaoar has been found to have large amounts of water ice in its surface, according to absorption bands at 1.5, 1.65, and 2.0 μm (Jewitt & Luu 2004; Schaller & Brown 2007b; Dalle Ore et al. 2009; Guilbert et al. 2009). Another band was found at 2.2 μm , which has produced some discussion among different authors, who suggest that this band could be due either to ammonia hydrate (NH₃·H₂O) or CH₄. The model by Dalle Ore et al. (2009) also included photometric data at wavelengths 3.6 and 4.5 μm from Spitzer. They claim a surface composition of $\sim 40\%$ H₂O, $\sim 10\%$ CH₄, and $\sim 50\%$ complex organics. They also fit a different model that includes up to 20% N₂. Taking into account those percentages of water and complex organics, Quaoar should appear in a region in the color-color diagram slightly more downward and rightward than depicted. Considering our method, we obtain a composition of $60 \pm 10\%$ H₂O, $20 \pm 10\%$ silicates, and $20 \pm 10\%$ complex organics. Note that, for simplicity, we have not included mixtures with supervolatiles; nonetheless, if there exists N₂ on its surface, which overlaps the CO region in the $K - 3.6 \mu\text{m}$ versus $3.6 \mu\text{m} - 4.5 \mu\text{m}$ diagram, the data point for Quaoar can be displaced up and to the left, toward its position shown in Figure 7(a). The water percentage is consistent with the models provided by Dalle Ore et al. (2009), and the variation in the other materials could be due to the inclusion of CH₄ and N₂ on their mixtures. Overall, its position is consistent with the models provided by Dalle Ore et al. (2009).

Orcus has been studied by several authors, and most of them agree on a composition with a low percentage of water (Fornasier et al. 2004b; de Bergh et al. 2005; Delsanti et al. 2010). Others have fit models with larger amounts of water. For instance, Trujillo et al. (2005) imposed an upper limit of 50% water ice, and Barucci et al. (2008) modeled the spectrum with $\sim 40\%$ water ice. DeMeo et al. (2010) also modeled the spectrum of Orcus with a larger amount of water (up to 70%), claiming that models from earlier papers (i.e., Fornasier et al. 2004b; de Bergh et al. 2005; Trujillo et al. 2005) did not include the albedo of Orcus, which was published by Stansberry et al. (2008). DeMeo et al. (2010) also discussed that the difference between their model and the model in Barucci et al. (2008) may be due to a different blue component used to fit the data. Other ices, such as CH₄, NH₃, and C₂H₆, have been proposed for Orcus (Trujillo et al. 2005; Delsanti et al. 2010), and the presence of CO₂ is hypothesized to not

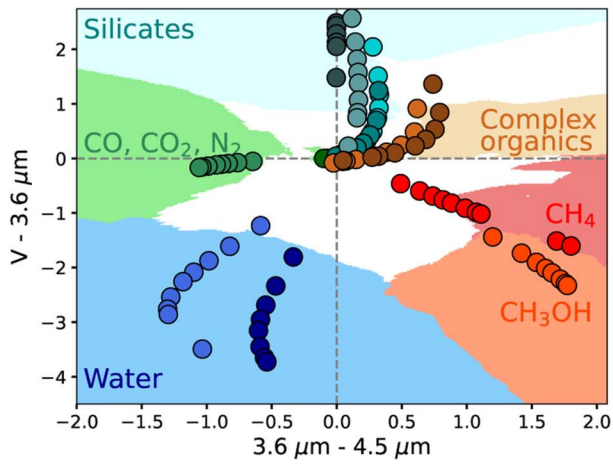
exceed 5% (DeMeo et al. 2010). Our data, which include the V-band albedo, are consistent with a large amount of water on the surface of Orcus: as can be seen in Figure 7(a), our method produces a composition of $70 \pm 10\%$ H₂O, $20 \pm 10\%$ silicates, and $10 \pm 10\%$ complex organics. Smaller amounts of water would be also consistent with our measurements if we include other volatiles (e.g., CO₂, N₂) in the mixture.

Another object that has its surface distinctly dominated by water ice is 2002 TX₃₀₀, which is part of Haumea's family; see its spectrum in Appendix B, as well as Licandro et al. (2006a) and Barkume et al. (2008). We obtain a composition of $30 \pm 30\%$ H₂O, $30 \pm 50\%$ silicates, and $40 \pm 50\%$ complex organics, which is consistent with the spectroscopic measurements, considering the error bars. However, we think that, given the high proportion of water detected through its spectrum (see, e.g., Licandro et al. 2006a), our method does not seem to be very accurate for this specific object. This could be due to the extremely wide absorption bands produced at 3.6 and 4.5 μm by the water, which could overlap one another, producing uncertainty on the photometric measurements when using wide passbands such as those used in this work (see Figure 4). Furthermore, the presence of CH₃OH could move its position rightward, as explained in Section 8.3. (Note that NIR colors of this object were extracted from its spectrum, for which p_V is needed; therefore, the large uncertainty on p_V translates into large uncertainty on the NIR colors).

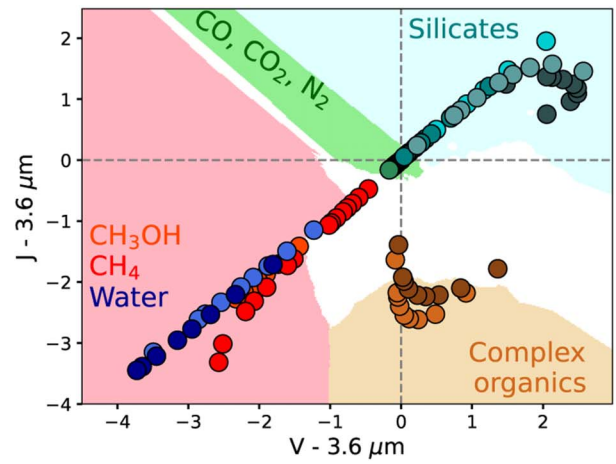
Spectral models for 2003 AZ₈₄ have included 17%–44% of water and small amounts of organic compounds (Barkume et al. 2008; Guilbert et al. 2009; Barucci et al. 2011). In the color-color diagram, it plots in a region intermediate between H₂O-dominated and silicate-dominated colors, with a composition of $30 \pm 10\%$ H₂O, $60 \pm 20\%$ silicates, and $10 \pm 10\%$ complex organics. If organics are present, these will not be greater than 20%, which is consistent with its slightly steeped spectral slope.

The spectrum of Lempo has been modeled with different proportions of H₂O ice, complex organics, and silicates: 5%–35%, 10%–65%, and 0%–85%, respectively (Dotto et al. 2003; Merlin et al. 2005; Barkume et al. 2008; Guilbert et al. 2009; Protospapa et al. 2009). The position of this object in the color-color diagram corresponds to a composition of $30 \pm 20\%$ H₂O, $20 \pm 10\%$ silicates, and $50 \pm 10\%$ complex organics, in agreement with the proportions mentioned previously. This is also supported by the $3.6 \mu\text{m} - 4.5 \mu\text{m}$ versus $V - 3.6 \mu\text{m}$ and the $V - 3.6 \mu\text{m}$ versus $J - 3.6 \mu\text{m}$ diagrams (see Section 7).

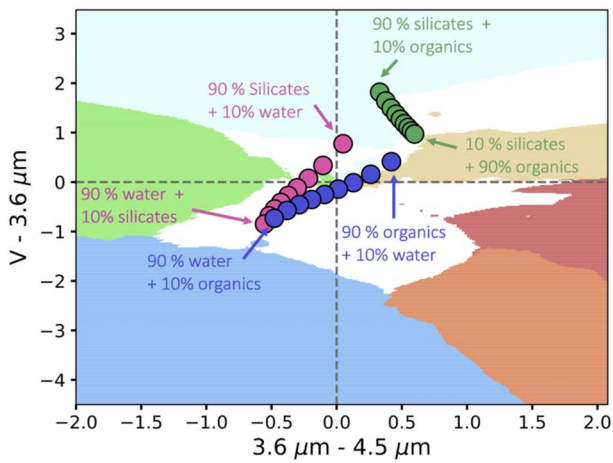
Eris and Makemake both have spectra dominated by CH₄, and spectral models suggest particle sizes as large as 20 mm for Eris (Licandro et al. 2006b; Merlin et al. 2009; Alvarez-Candal et al. 2011), and 1 cm for Makemake (Licandro et al. 2006c; Brown et al. 2007a), and both appear well inside the methane region. Note that Makemake is at the boundary between methane and methanol, where these classification methods do not provide accurate results. Also note that, compared with Figure 5, its position is closer to points corresponding to larger methane particles than to those corresponding to methanol particles. Since it is clear that they have a composition dominated by pure methane and that the grain size is playing an important role, given their position in the compositional clock, for these two objects we have applied the KNN method to obtain the grain size of this material. For this calculation, we took only methane models and added six models with larger grain sizes (specifically, 0.4, 0.5, 1, 1.5, 2, 2.5, 5, and 10 mm).



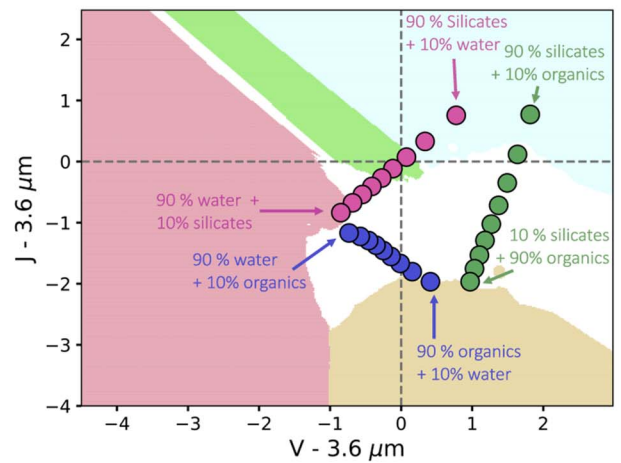
(a) Pure materials.



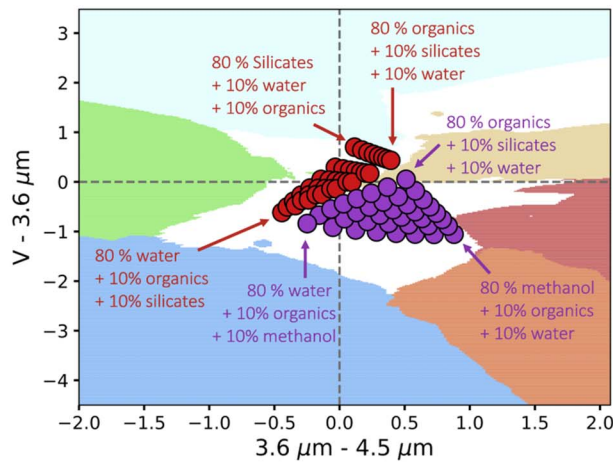
(b) Pure materials.



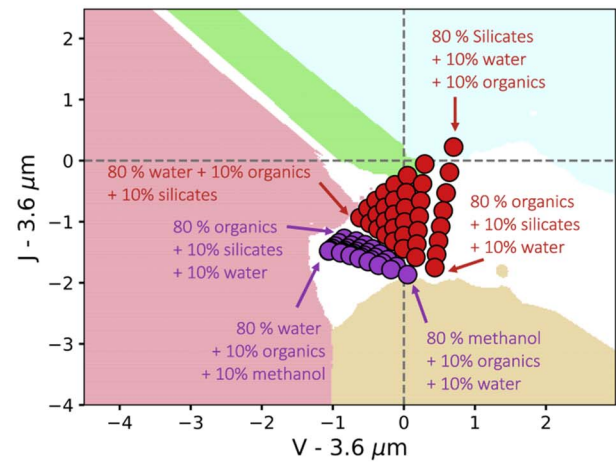
(c) Mixture of two components.



(d) Mixture of two components.



(e) Mixture of three components.



(f) Mixture of three components.

Figure 8. Left panels: $3.6 \mu\text{m} - 4.5 \mu\text{m}$ vs. $V - 3.6 \mu\text{m}$ diagrams for pure components, mixtures of two components, and mixtures of three components (panels a, c, and e, respectively). Shaded regions corresponds to a different material as indicated in panel (a) and equivalent to the compositional clock (Figure 5). Right panels: $V - 3.6 \mu\text{m}$ vs. $J - 3.6 \mu\text{m}$ diagrams for pure components, mixtures of two components, and mixtures of three components (panels b, d, and f, respectively). In this case, since water, CH_4 , and CH_3OH occupy the same region, the pink shaded region corresponds to those three materials as indicated in panel (b).

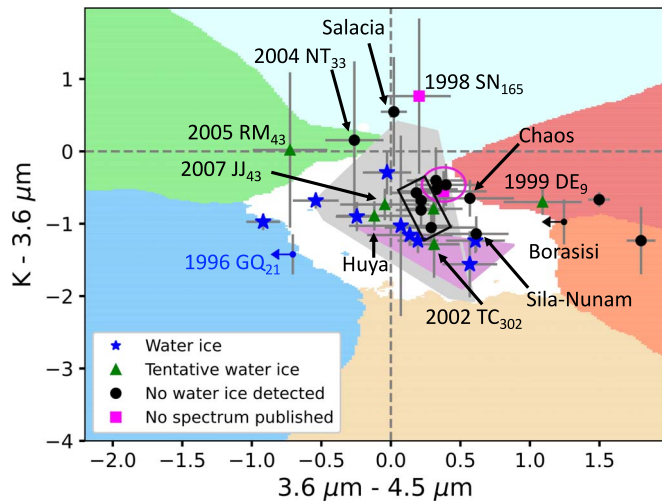


Figure 9. Compositional clock plotting observational data. For comparison between spectroscopic measurements and our results, symbols and colors represent the presence or lack of water detected in spectroscopic data as found in the literature. Blue stars show objects for which water has been identified before using published spectra up to $2 \mu\text{m}$. Green triangles represent objects with tentative detections of water ice using published spectra up to $2 \mu\text{m}$. Black circles represent objects with no identification of water ice in their published spectra. Pink squares show objects for which no spectra have been published. Shaded regions correspond to pure materials as labeled in Figure 7 and explained in Section 6.1. White region is dominated by the combination of all mixtures of different proportions, as explained in Figures 6 and 7(b). Gray shaded polygon represents the binary and ternary models of different proportions of H_2O –silicates–organics plotted in Figure 6. The purple triangle represents models of different proportions of H_2O – CH_3OH –organics. Objects within the black rectangle are the following: 2002 AW₁₉₇, 2005 RN₄₃, 2002 UX₂₅, 2004 TY₃₆₄, and 2000 GN₁₇₁ (from top to bottom). Objects within the pink oval are the following: Varda, 2000 PE₃₀, 2001 UR₁₆₃, and 2004 GV₉.

We did not include sizes larger than 10 mm because the position of the objects in the diagram clearly indicated sizes between 0.4 and 1 mm. In total, we had 15 methane models from 0.01 to 10 mm to perform the KKN method, for which we chose $K = 5$, following the same explanation given in Section 6.1. We obtain a particle size of 0.2 ± 0.1 and 1 ± 0.4 mm for Eris and Makemake, respectively. Even though our models result into particle sizes smaller than those obtained by the spectroscopic models, they manifest the necessity of using larger particle sizes. The difference between the measured grains sizes and those considered here can be explained due to the response of methane molecules at 3.6 and $4.5 \mu\text{m}$, which is higher than in the visible, producing wider absorption bands.

Salacia is an object with a very flat spectrum (Pinilla-Alonso et al. 2008; Schaller & Brown 2008), for which no H_2O ice or other absorption features have been documented. Pinilla-Alonso et al. (2020) suggest that this object has a highly processed surface covered by a mixture of carbon and amorphous silicates. Its position within the silicate region of the color–color diagram results in a proportion of $10 \pm 20\%$ H_2O , $90 \pm 20\%$ silicates and no organics, consistent with the previously detected lack of features.

Sedna and 2002 VE₉₅ are objects for which water ice has been detected in their spectra, yet both objects appear well away from the H_2O -ice region in the color–color diagram. However, their locations are clarified if we consider ternary mixtures of H_2O , complex organics, and CH_3OH , as shown in panel (b) of Figure 7. Because CH_4 and CH_3OH occupy a similar region in the compositional clock, a similar location for

each object is displayed if we use CH_4 instead of CH_3OH , which makes it impossible to distinguish between them using this method. However, we can indicate the presence of CH_4 and/or CH_3OH on the surface of the objects, and confirm their existence using VNIR spectroscopy, as CH_4 and CH_3OH behave quite different at those wavelengths (see Figure 4). Sedna’s spectrum has been modeled by Emery et al. (2007) using VNIR spectroscopy and Spitzer measurements at 3.6 and $4.5 \mu\text{m}$. They found the best model was given by a mixture of 50% CH_4 , 25% complex organics, 15% H_2O , and 10% N_2 . This agrees with Sedna’s position in the color–color diagram, which corresponds to a composition of $25 \pm 10\%$ H_2O ice, $50 \pm 10\%$ CH_4 , and $25 \pm 10\%$ complex organics. The spectrum of 2002 VE₉₅ has been modeled using 12%–13% H_2O , 10%–12% CH_3OH , 64%–78% complex organics, and 0%–11% silicates (Barucci et al. 2006; Barkume et al. 2008). This is consistent with 2002 VE₉₅’s position in the color–color diagram, which corresponds to $20 \pm 10\%$ H_2O , $40 \pm 10\%$ CH_3OH , and $40 \pm 20\%$ organics.

Varuna has been found to have absorption bands related to water ice (Licandro et al. 2001; Barkume et al. 2008). Also, Lorenzi et al. (2014) fit its spectrum using two different mixtures: one composed of 25% water, 25% silicates, 35% complex organics, and 15% carbon; and a second one composed of 20% water, 25% silicates, 35% complex organics, 10% carbon and 10% of CH_4 . The position of this object in the compositional clock results in a different proportion of water depending on whether the mixture is a combination of water, silicates, and organics or water, methanol, and organics. For the former, the resulting composition is $30 \pm 10\%$ H_2O ice, $20 \pm 10\%$ silicates, and $50 \pm 10\%$ organics, while for the latter, the resulting composition is $50 \pm 10\%$ H_2O ice, $20 \pm 10\%$ methane, and $30 \pm 10\%$ organics. A combination between both mixtures is in agreement with the spectroscopic models.

Based on the test cases presented, we find that overall the color–color diagram provides compositional information that is consistent with that derived from visible to near-IR spectral fits for well-characterized TNOs. Appendix A presents an individually exploration to understand the composition, based on IRAC data, for the large numbers of objects in our sample that lack detailed characterization in the visible and near-IR wavelengths.

7. Other Color–Color Diagrams

We have built other color–color diagrams in order to verify and/or identify the different components that dominate the surface of our sample (see Figure 8). The results of these diagrams are explained similarly to the compositional clock.

Of special interest is the diagram of $3.6 \mu\text{m} - 4.5 \mu\text{m}$ versus $V - 3.6 \mu\text{m}$. Synthetic models of the components plotted in the compositional clock can be seen in the left panels of Figure 8, where pure materials, mixtures of two components, and mixtures of three components are plotted. The region of influence of each material has been plotted using the KNN method as explained in Section 6.1. The inconvenience of this diagram is that the organic materials occupied a very similar region to the silicates, so we cannot distinguish between them. Also, when comparing the three panels, it can be seen that the mixtures with high percentages of silicates and/or organics overlap the regions occupied by models of pure materials, which makes that region unsuitable for our purpose. This is noticeable, for instance, when using the K-nearest neighbor

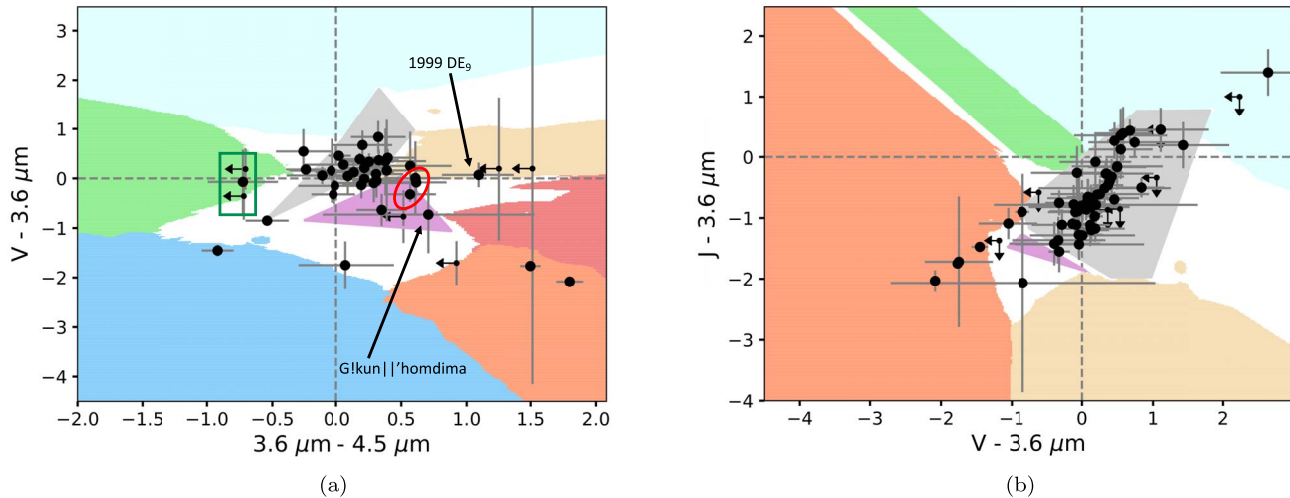


Figure 10. (a) Diagram of $3.6 \mu\text{m} - 4.5 \mu\text{m}$ vs. $V - 3.6 \mu\text{m}$, highlighting objects that have or may have ices on their surfaces. Objects within the red circle are Sedna, Sila-Nunam, and 2002 VE₉₅ (from top to bottom). Objects within the black rectangle are 1996 GQ₂₁, 2005 RM₄₃, and 2004 PG₁₁₅ (from top to bottom). Shaded regions correspond to different materials as indicated in Figure 8(a) and equivalent to the compositional clock (Figure 5). (b) Diagram $V - 3.6 \mu\text{m}$ vs. $J - 3.6 \mu\text{m}$. Shaded regions correspond to different materials as indicated in Figure 8(b). In both diagrams, gray shaded polygons represent the binary and ternary models of different proportions of H₂O-silicates-organics, and purple triangles represent models of different proportions of H₂O-CH₃OH-organics as plotted in Figure 8.

method, which produces blurred results in that region. However, there are two advantages. The first one is that, because there are more objects observed with visible colors than near-infrared colors, we can analyze a larger sample than using the compositional clock. The second is that some organic materials change their position with respect to the compositional clock, therefore we are able to more easily distinguish between complex organics and CH₄ and CH₃OH compounds.

In Figure 8, the panels on the right show diagrams of $V - 3.6 \mu\text{m}$ versus $J - 3.6 \mu\text{m}$. As in the other cases, this figure shows models of pure materials, mixtures of two components, and mixtures of three components (panels b, d, and f, respectively). In this diagram, models with higher proportions of silicates are in the upper right quadrant and organic materials appear in a completely different region than do the other materials. Meanwhile, supervolatiles are nearly indistinguishable, and H₂O, CH₄, and CH₃OH share the same region in the lower left quadrant. For that reason, we have applied the KNN, considering one region for H₂O, CH₄, and CH₃OH models (pink shaded region), while the rest of the colors are equivalent to the other diagrams. This diagram is especially suitable for the identification of complex organics.

At VNIR wavelengths (up to $2.2 \mu\text{m}$), complex organics and amorphous silicates present very similar behavior, with no absorption bands (Cruikshank et al. 2005). Therefore, we can only claim indications of objects with higher proportions of complex organics than silicates, and vice versa, depending on the slope of the spectrum, i.e., objects with abrupt slopes will be modeled using complex organics, while for objects with less abrupt slopes, the spectrum will be modeled by a combination of silicates and complex organics (Emery & Brown 2004). However, the different behavior of silicates and complex organics at IRAC wavelengths (Figure 4) enables separation of these two materials in the compositional clock and the $J - 3.6 \mu\text{m}$ versus $V - 3.6 \mu\text{m}$ diagram (panels b, d, and f in Figure 8), allowing the identification of complex organics (due to absorption bands beyond $2.2 \mu\text{m}$), and demonstrating that

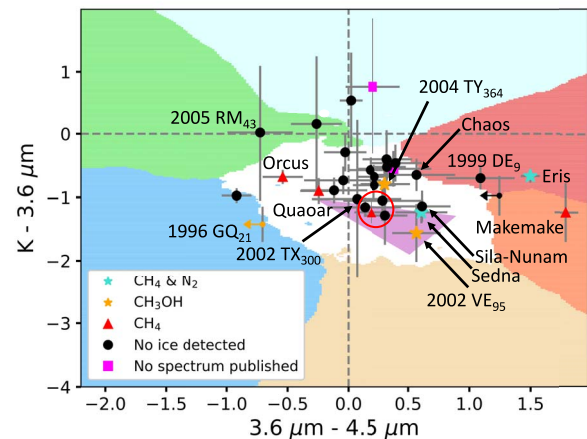


Figure 11. Compositional clock with the sample highlighting objects for which bands related to ices have been identified in VNIR spectroscopic measurements. Turquoise stars depict objects that have CH₄ and N₂ in their spectra. Orange stars represent objects with possible detection of CH₃OH. Red triangles represent objects with CH₄ detections. Black circles represent objects with no identification of any ice in their spectra. Pink squares show objects for which no spectroscopic data have been published. Red, orange, and green shaded regions represent the regions of influence of synthetic models of different grain sizes of pure methane, methanol, and supervolatiles (N₂, CO, ...), respectively. White region represents the region of influence of synthetic models with different proportions of mixtures of H₂O-CH₄-organics, and H₂O-silicates-organics. Purple triangle bounds the theoretical points of different proportions of H₂O-CH₃OH-organics.

the wide bandpass of IRAC at 3.6 and $4.5 \mu\text{m}$ is a powerful tool to identify, for the first time, what the coloring agent that produces redness on TNOs is.

8. The Surface Composition of Our Sample

We have demonstrated the consistency of our photometric measurements with the presence of H₂O ice and other materials such as CH₄, CH₃OH, complex organics, and amorphous

silicates for objects that present clear signature of those materials in their VNIR spectra (up to $2.0 \mu\text{m}$). Our idea within the following subsections is to focus on the different materials that can be detected using the IRAC colors.

8.1. Water Ice

In Figure 9, we plotted our sample as a function of the detection of water ice in the VNIR spectra published in the literature (up to $2.0 \mu\text{m}$; e.g., Licandro et al. 2001; Barucci et al. 2011; Lorenzi et al. 2014). Blue stars represent objects for which water detection is already known from the spectra, and were used to test our method (see Section 6.2). This includes Sedna and 2002 VE₉₅, for which H₂O has been detected using spectroscopic studies, and as we explained at the end of Section 6.2, the presence of CH₃OH moves them rightward within the diagram. One object we have not yet discussed is 1996 GQ₂₁, because we only obtained an upper limit at $4.5 \mu\text{m}$ (a more detailed discussion can be found in Appendix A). However, this limit constrains the region in which the object is localized within the diagram, eliminating the possibility of having ices other than water.

Objects with tentative detections of water in the VNIR spectra are represented by green triangles. As can be seen, with the exception of 2005 RM₄₃ and 1999 DE₉, all of them fall within regions where H₂O has to be part of the composition. The position of 2005 RM₄₃ in Figure 9 is quite interesting, as this region is the one dominated by CO₂. However, since the error bars are quite large, we have considered a mixture of organics, silicates, and water to obtain a composition, resulting in $50 \pm 40\%$ H₂O ice, $50 \pm 40\%$ silicates, and no organics. Large amounts of H₂O should be detected by VNIR spectroscopy, which is not the case. The presence of CO₂ in the mixture could be placing the object in that region of the diagram while decreasing the amount of water. Additionally, as we point out in Section 8.3, other color-color diagrams support the possibility of this object having CO₂. On the other hand, the presence of H₂O for 1999 DE₉ has been discussed by several authors with no clear agreement. We conclude that the position of this object within the diagram is not consistent with the presence of H₂O, but is consistent with there being CH₃OH on its surface (see also Jewitt & Luu 2001). Considering a mixture of H₂O–CH₃OH–organics, the resulting proportion for this object is $20 \pm 10\%$ H₂O, $60 \pm 10\%$ CH₃OH, and $20 \pm 10\%$ organics. These two objects are deeply discussed in Section 8.3.

Black circles in Figure 9 represent objects for which no H₂O has been reported before. Our results show that 2004 NT₃₃ and the groups formed by 2000 GN₁₇₁, 2002 AW₁₉₇, 2002 UX₂₅, 2004 TY₃₆₄, 2005 RN₄₃, Varda, 2001 UR₁₆₃, and 2004 GV₉, marked by a black rectangle and a pink circle, are consistent with $\sim 20\%$ H₂O ice within their composition. The resulting proportions for each object are given in Appendix A.

For those objects that have published spectra in the literature, we are able to say that our results are in agreement with the spectra (see Appendix A for an individual explanation on each object). In summary, IRAC colors are highly sensitive to the presence of H₂O, thus when using the $3.6 \mu\text{m} - 4.5 \mu\text{m}$ diagram, with a total of 30 objects (32 if counting the upper limits), 26 objects (86%) present error bars within a 1σ independent probability consistent with the presence of H₂O on their surface, with 22 (73%) representing the 1σ compound probability.

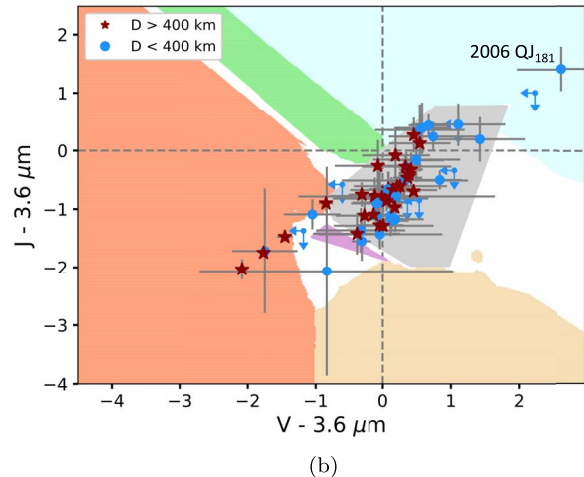


Figure 12. Diagram of $V - 3.6 \mu\text{m}$ vs. $J - 3.6 \mu\text{m}$ as a function of size. Objects with diameters smaller than 400 km are represented by brown circles, while objects larger than 400 km are represented by red stars. Shaded regions are equivalent to those in Figure 10(b).

This conclusion is also consistent with the other two color-color diagrams (Figure 10). In Figure 10, we have plotted our sample represented by black circles, and the shaded regions corresponding to each pure material (as described in Figure 8), with the white region representing binary and trinary mixtures. From panel (a), we obtain that 30 of a total of 37 objects (81%) present error bars within a 1σ independent probability consistent with the presence of H₂O on their surface, with 26 (70%) representing the 1σ compound probability. From panel (b), we obtain that 50 of a total of 59 objects (85%) present error bars within a 1σ independent probability consistent with the presence of H₂O on their surface, with 36 (61%) representing the 1σ compound probability.

8.2. Complex Organics

As we have discussed, in order to obtain colors that occupied the center of the compositional clock (see Figure 6), it is required to include complex organics (e.g., tholins) within our models. Tholins have been used for modeling the spectra of different objects but have not been detected before, as they do not produce an absorption band at the VNIR spectra. Our method provides a high level of confidence that the surface of most objects within our sample is composed of a mixture that includes complex organic materials such as tholins (e.g., Khare et al. 1993; Materese et al. 2014, 2015). For instance, in Figure 9, we obtain that 80% of the sample present error bars within a 1σ independent probability consistent with the presence of organic material in their surface composition, with the same percentage (80%) representing the compound probability. From Figure 10(b), we obtain that 90% of the sample present error bars within a 1σ independent probability consistent with the presence of organic material on their surface, with 63% representing the compound probability. We do not include statistics from Figure 10(a), since both organics and silicates occupy similar regions and there is no clear separation between them. Our preferred statistics are the ones provided by the compositional clock ($K - 3.6 \mu\text{m}$ versus $3.6 \mu\text{m} - 4.5 \mu\text{m}$ diagram), since they maximize the range difference of colors for each material.

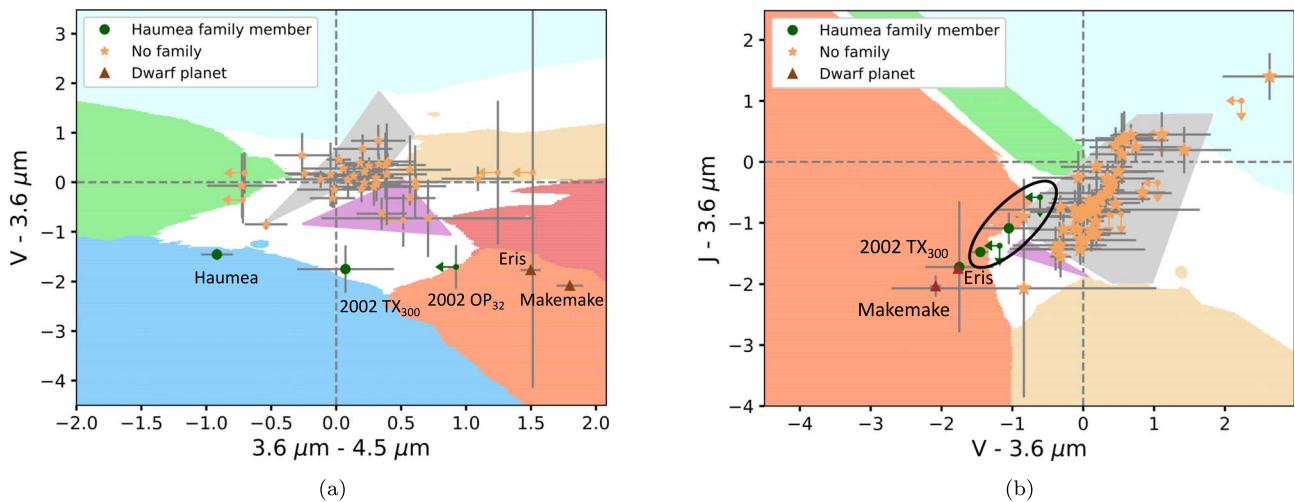


Figure 13. (a) Diagram of $3.6 \mu\text{m} - 4.5 \mu\text{m}$ vs. $V - 3.6 \mu\text{m}$ and of (b) $V - 3.6 \mu\text{m}$ vs. $J - 3.6 \mu\text{m}$. Objects within the black oval are as follows: Haumea, 2005 RR₄₃, 1995 SM₅₅, Orcus, and 1996 TO₆₆ (from left to right). In both panels, we represented the sample as a function of Haumea’s family members and dwarf planets (confirmed through dynamical models and spectroscopic measurements; see Brown et al. 2007b; Snodgrass et al. 2010). Shaded regions are equivalent to those explained in Figure 10.

Specifically in Figure 9, the groups marked by a black rectangle and a pink circle require a percentage between 10% and 60% of complex organics. All of them present an absorption identification at $3.6 \mu\text{m}$ with respect to $4.5 \mu\text{m}$, as well as an abrupt spectral slope in the visible (see Figure 3 and Appendix B, with the exception of 2000 PE₃₀, which has no spectrum published). Huya, Quaoar, and 2007 JJ₄₃ require between 10% and 40% of complex organics; however, this amount of complex organics might be hidden in their spectra due to the large amount of H₂O ice, which flattens the spectral slope.

8.3. Supervolatiles, CH₄, and/or CH₃OH

This section is dedicated to the identification of compositions consistent with the presence of supervolatiles, CH₄, and/or CH₃OH. Figure 11 shows our sample as a function of objects with detections of CH₄, CH₃OH, CO₂, CO, and N₂, as found in the literature from VNIR spectra (e.g., Barucci et al. 2011). Turquoise stars show objects with detection of both CH₄ and N₂. The two objects, Sedna and Eris, with this composition were discussed in Section 6.2, where we explained the good agreement between the results from spectra and ours. Red triangles represent those objects for which CH₄ has been detected from their spectra. As discussed in Section 6.2, Makemake and Eris both have detection of methane with grain sizes over 0.4 mm in their spectra and appear in a region not only dominated by this component but also in which a larger particle size is necessary. The other two objects, Quaoar and Orcus, with CH₄ detection in their spectra are located in a region that seems to contradict this detection. In these specific cases, the large amount of H₂O ice is hiding the detection of CH₄ using this method, and therefore we do not exclude CH₄ as part of their composition. Additionally, for Orcus, its position suggests the presence of CO₂, which has also been suggested by DeMeo et al. (2010).

Objects represented by an orange star are those for which CH₃OH has been tentatively suggested. For 2002 VE₉₅, the detection of CH₃OH is in clear agreement with its position in Figure 11. As explained in Section 6.2, we obtained a composition that includes $40 \pm 20\%$ of complex organics,

considering a mixture of H₂O–CH₃OH–organics. The position of 2004 TY₃₆₄ is not as clear. Considering models with a mixture of H₂O–CH₃OH–organics, we obtain a proportion of $50 \pm 10\%$, $30 \pm 10\%$, and $20 \pm 10\%$, respectively. However, such an amount of water should be noticeable in its spectrum, and that is not the case. On the other hand, considering a mixture of H₂O–silicates–organics, we obtain a proportion of $20 \pm 10\%$, $50 \pm 10\%$, and $35 \pm 10\%$, respectively. The latter is more in agreement with its spectra, although a combination of both mixtures would be a very likely situation. The other two interesting objects in this figure are Sila–Nunam and 1999 DE₉, whose positions are consistent with the presence of CH₄ or CH₃OH. Due to the small size of the binary system (around 300 km; Vilenius et al. 2012; Lellouch et al. 2013), it is unlikely that Sila and Nunam possess CH₄ on their surfaces. Instead, it is more realistic to think that their position in Figure 11 is due to CH₃OH, and the same occurs also for 1999 DE₉. We obtain a composition of $30 \pm 10\%$ H₂O, $50 \pm 10\%$ CH₃OH, and $20 \pm 10\%$ organics for Sila–Nunam and $20 \pm 10\%$ H₂O, $60 \pm 10\%$ CH₃OH, and $20 \pm 10\%$ organics for 1999 DE₉. A more detailed explanation is given in Appendix A.

A composition including CH₄ and CH₃OH on the surfaces of Sedna and 2002 VE₉₅, respectively, is consistent also with their position in Figure 11, as explained in Section 6.2.

There are three objects, (Lempo, 2000 GN₁₇₁, and 2002 TC₃₀₂) depicted by black points within the red circle that are very close or within the purple triangle, whose position could indicate the presence of CH₃OH. However, for them to have CH₃OH and be located on that region, they would also require a high percentage of H₂O, which should have been detected in their VNIR spectra (specific proportions for each of them are given in Appendix A). On the contrary, the object 2002 TX₃₀₀, which is right next to the red circle, is known for having large amounts of water on its surface (Licandro et al. 2006a). Considering a mixture of H₂O–CH₃OH–organics, we obtain a composition of $60 \pm 30\%$ H₂O, $20 \pm 10\%$ CH₃OH, and $30 \pm 30\%$ organics. Therefore, the existence of CH₃OH on the surface of 2002 TX₃₀₀ could be displacing this object to the right of the diagram.

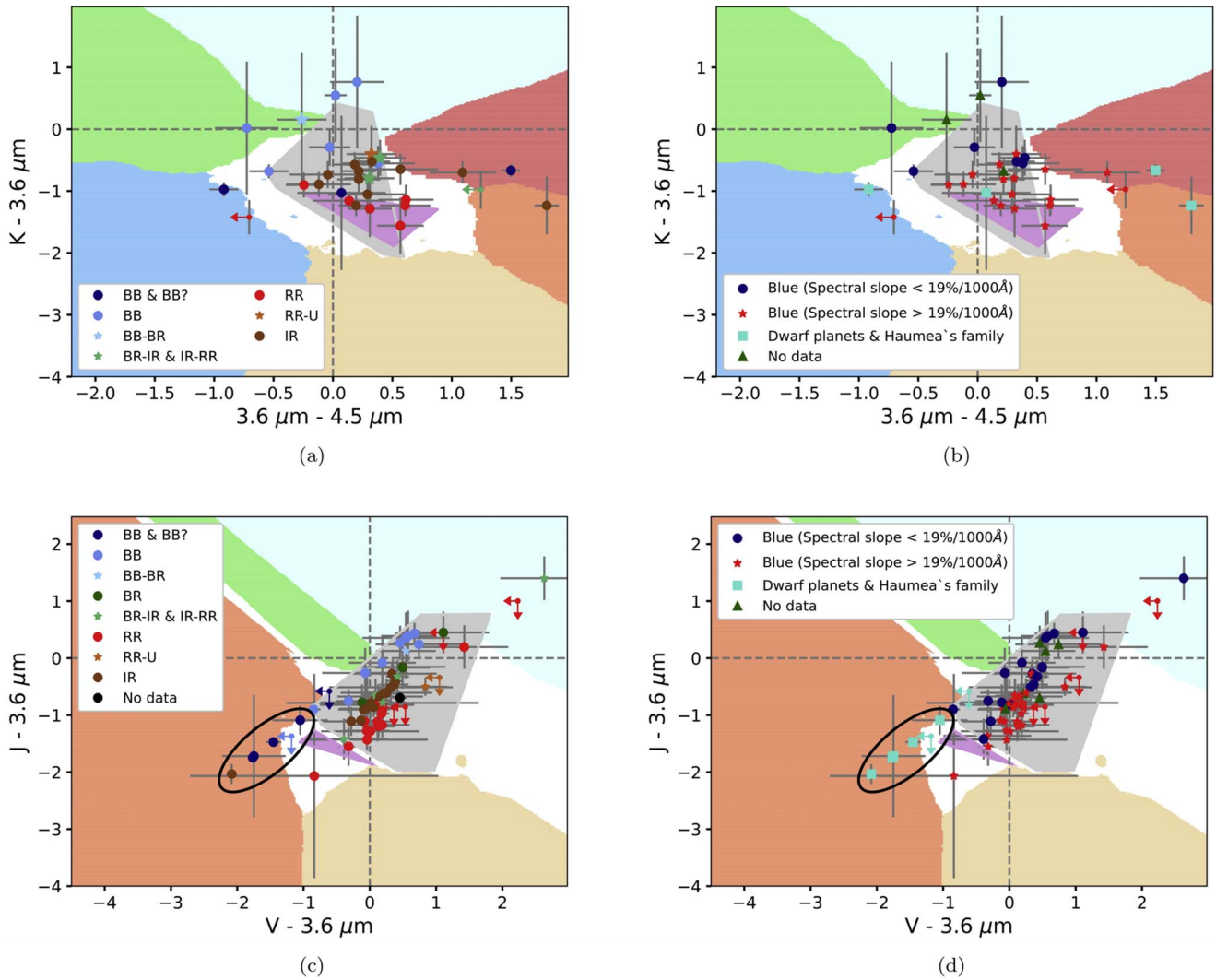


Figure 14. Upper panels: Compositional clock as a function of taxonomic classifications. Shaded regions are equivalent to those of Figure 5. (a) Taxonomy developed by Barucci et al. (2005a) and Belskaya et al. (2015). (b) Taxonomy developed by Fraser & Brown (2012) and Lacerda et al. (2014). Bottom panels: $V - 3.6 \mu\text{m}$ vs. $J - 3.6 \mu\text{m}$ diagrams as a function of taxonomy classifications. Shaded regions are equivalent to those of Figure 8(b). (c) Taxonomy developed by Barucci et al. (2005a) and Belskaya et al. (2015). (d) Taxonomy developed by Fraser & Brown (2012) and Lacerda et al. (2014). The group of objects with extremely high albedo claimed by both taxonomic theories are located within the black oval.

Finally, as we mentioned in Section 8.1, in Figure 11, 2005 RM_{43} shares the region occupied by CO_2 . Although the error bars are large and could place this object out of this region, the diagram of $V - 3.6 \mu\text{m}$ versus $J - 3.6 \mu\text{m}$ also supports this interpretation (see panel (a) in Figure 10), where there are four objects that share the region occupied by CO_2 : 1996 GQ_{21} , 2002 GV_{31} , 2004 PG_{115} , and 2005 RM_{43} . Although three of these objects have measurements with only upper limits in the $3.6 \mu\text{m} - 4.5 \mu\text{m}$ color, these limits also constrain the objects to regions dominated by supervolatiles (CO_2 , CO , N_2) and/or water. On the other hand, the error bars for the $V - 3.6 \mu\text{m}$ color constrain the region to one dominated by the supervolatiles. Therefore, our measurements suggest the possibility of these objects containing CO_2 and H_2O . A more detailed explanation and specific proportions considering a mixture of H_2O , silicates, and organics are given in Appendix A.

Summarizing, seven of 30 objects within the compositional clock (Eris, Makemake, Sila-Nunam, Sedna, 2002 VE_{95} , 2004 TY_{364} , and 2002 TX_{300}), 32 including those with upper limits, are consistent with a composition that includes CH_3OH and/or

CH_4 on their surfaces. Considering other color-color diagrams (Figure 10), a total of four objects are consistent with a composition that includes CO_2 .

8.4. Silicates

In the compositional clock, the region dominated by the amorphous silicates (see Figure 9) is occupied by two objects: Salacia and 1998 SN_{158} . Salacia was discussed in Section 6.2, where we conclude that it has a surface clearly dominated by silicates. 1998 SN_{165} 's measurements are also consistent with a surface dominated by amorphous silicates. We obtain a proportion of $90 \pm 20\%$ silicates, $10 \pm 10\%$ H_2O , and no organics.

In this regard, we also found interesting information representing the $V - 3.6 \mu\text{m}$ versus $J - 3.6 \mu\text{m}$ diagram when dividing the sample between small objects (those with diameters, D , smaller than 400 km) and large objects (those with $D > 400$ km; see Figure 12). In this specific diagram, where there is a total of 28 objects over 400 km, only one object presents a 1σ probability of having $J - 3.6 \mu\text{m} > 0$, or in other words, being dominated by silicates: that object is Salacia, which has a diameter of ~ 900 km

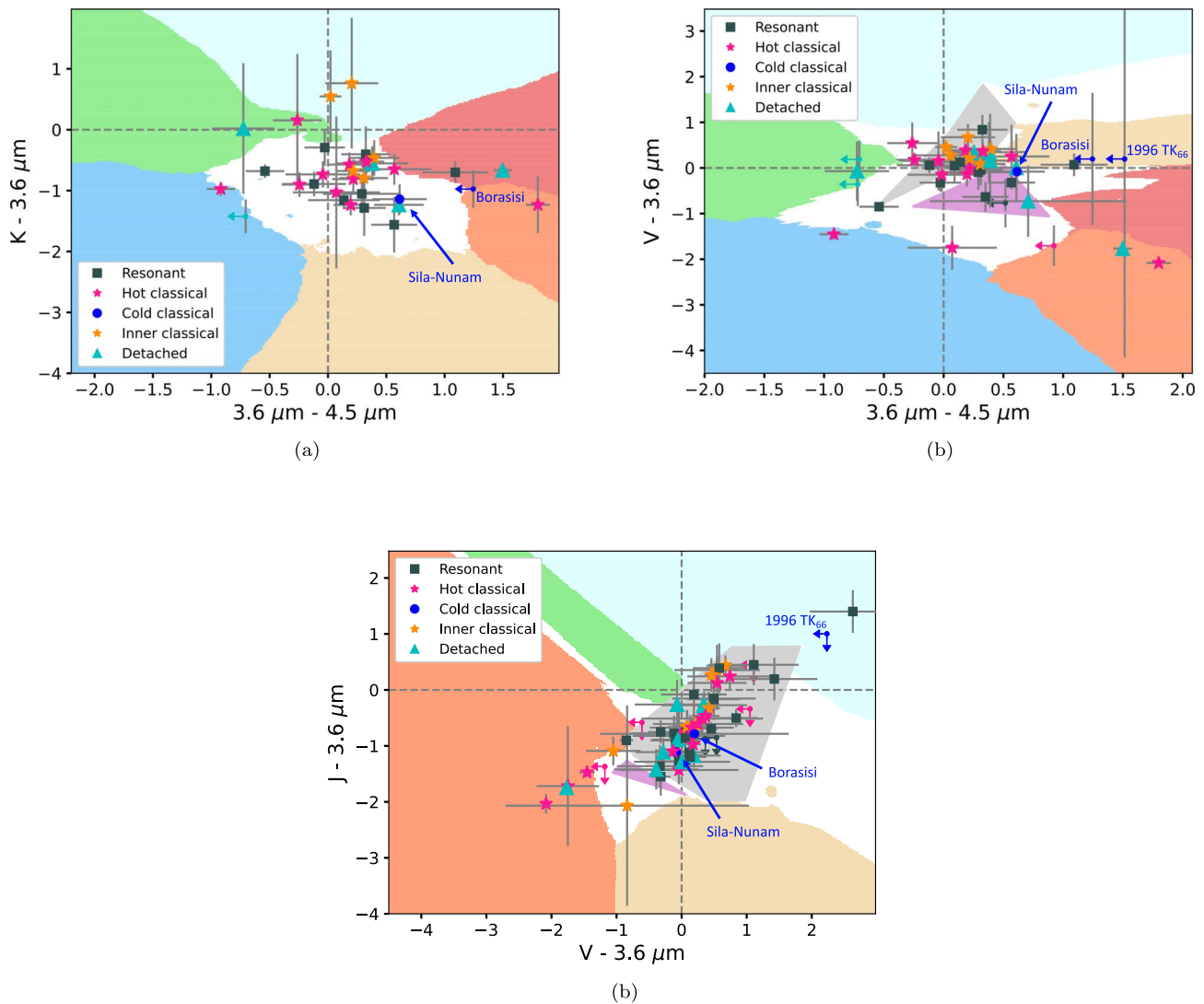


Figure 15. Compositional clock as a function of dynamical classes. Green squares depict resonant objects, turquoise triangles depict detached objects, pink stars depict hot classical objects, and blue circles depict cold classical objects. Asterisks represent objects for which $3.6 \mu\text{m} - 4.5 \mu\text{m}$ color is an upper limit, and the color of the asterisks is matched to the dynamical class. In all three diagrams, shaded regions are equivalent to those of Figures 5 and 8(a) and (b).

(Fornasier et al. 2013). This translates into a 4% probability of an object over 400 km presenting $J - 3.6 \mu\text{m} > 0$. There are six objects with $D < 400$ km (from a total of 38) with colors consistent with a surface dominated by silicates: 2000 GP₁₈₃, 2000 QL₂₅₁, 2001 CZ₃₁, 2001 QJ₁₈₁, 2002 CY₂₂₄, and 2004 EW₉₅. For all of them, we obtain over 80% of silicates on their respective surfaces, considering a mixture of H₂O, silicates, and organics (see detailed information in Appendix A). In fact, the spectrum of 2004 EW₉₅ was studied by Seccull et al. (2018). They demonstrated that its composition is “consistent” with a C-type asteroid and the spectrum presents a clear feature produced by hydrated, iron-rich silicates. This result provides validity for these specific colors to indicate surface consistency with compositions dominated by silicates.

9. Diagrams by Dwarf Planets and Haumea’s Family

Panel (a) in Figure 13 shows the $V - 3.6 \mu\text{m}$ versus $3.6 \mu\text{m} - 4.5 \mu\text{m}$ diagram and indicates whether the objects are dwarf planets, Haumea family members, or neither of these

two classifications. This diagram reveals that dwarf planets and Haumea family members (confirmed through dynamical models and spectroscopic measurements; see Brown et al. 2007b; Snodgrass et al. 2010) appear segregated from the rest of the TNO population (including those non-Haumea family members that show H₂O), in regions dominated by H₂O, CH₄, or CH₃OH and in agreement with previous knowledge about their composition.

In panel (b) of Figure 13, these objects appear again in a region detached from the rest of the sample. The dwarf planets, Makemake, Eris, Haumea, and 2002 TX₃₀₀ are clearly located over the region dominated by pure CH₄ or H₂O materials. The location of 1995 SM₅₅ is not as clear; however, it is detached from the rest of the population. Measurements for 2005 RR₄₃ and 1996 TO₆₆ are upper limits in both axes; however, these limits constrain the surface composition to models with high percentages of water, in agreement with their published spectra (Brown et al. 1999; Pinilla-Alonso et al. 2007; Barucci et al. 2011).

Due to the lack of measurements for Haumea family members either at infrared wavelength or at $4.5 \mu\text{m}$, we are not able to use the diagram $K - 3.6 \mu\text{m}$ versus $3.6 \mu\text{m} - 4.5 \mu\text{m}$ (Haumea and 2002 TX₃₀₀ are the only two objects within the family that provide such a combination of measurements).

New observations of objects that have been dynamically identified as part of the family could also be “spectroscopically” confirmed if they fall in the same region of both diagrams.

10. Diagrams by Taxonomic Classifications

The paucity of spectroscopic data compelled different authors to establish taxonomic classes in order to interpret the different surfaces found in the trans-Neptunian region. Two different taxonomies can be found in the literature. One was first proposed by Barucci et al. (2005b), who proposed four different taxonomic groups: neutral objects (BB), two intermediate slightly red types (BR and IR), and the reddest objects (RR). This taxonomy was updated more recently by Belskaya et al. (2015), where the BB taxonomic group was divided between objects with high and low albedo (BBb and BB, respectively). The other system was first proposed by Fraser & Brown (2012) and further developed by Lacerda et al. (2014), who presented a different perspective in which two main classes are defined: the red one, which includes objects with higher albedos and redder colors, and the blue one, which includes objects with lower albedos and less red colors. Furthermore, Lacerda et al. (2014) proposed two other groups within the latter taxonomy classification in order to distinguish between dwarf planets and Haumea’s family. The taxonomy proposed by Fraser & Brown (2012) is also discussed in Schwamb et al. (2019).

The most interesting diagrams to plot by taxonomy are the compositional clock ($3.6 \mu\text{m} - 4.5 \mu\text{m}$ versus $K - 3.6 \mu\text{m}$) and the $V - 3.6 \mu\text{m}$ versus $J - 3.6 \mu\text{m}$ diagrams (Figure 14). In both cases, we see how blue (Lacerda et al. 2014) and neutral (Belskaya et al. 2015) objects, depending on the reference, fall within regions where our models indicate the presence of high percentages of water and/or silicates, which have generally more neutral spectroscopic slopes. In contrast, redder objects are found in regions where models indicate the presence of organic materials, which have redder spectral slopes. In panels (c) and (d) of Figure 14, we can also highlight the group of objects that are distinct from the rest of TNOs due to their extremely high albedo. This group can be seen at the locations of models with pure water, CH₄, and CH₃OH, which have the common characteristic of presenting high albedos.

We want to emphasize that our data can generate a compositional context for the different taxonomic classifications. For instance, IR objects are consistent with having a mixture of similar proportions of silicates and complex organics and having nonzero H₂O. Also, most RR (Belskaya et al. 2015) and red (Lacerda et al. 2014) objects are consistent with being composed of material with smaller proportions of silicates and both rich in organics, and having a nonzero H₂O-ice content. While the latter was known for part of our sample from VNIR spectroscopy, the former was only inferred due to their red colors. Our measurements provide a high level of confidence that this red visible color is imparted by organic materials such as tholins (e.g., Khare et al. 1993; Materese et al. 2014, 2015), which produce absorption bands beyond $2.2 \mu\text{m}$.

11. Diagrams by Dynamical Classes

As mentioned in Section 1, one might expect that different dynamical classes could experience different physical processes, due to having different past and present environments, and therefore that they may exhibit at least slightly different surface compositions. As expected, Figure 15 shows that there is no distinction between detached, resonant, and hot classical objects.

In particular, all of our inner classical belt objects fall firmly in with the majority of TNOs, even the low-*i* inner beltlers. This fact thus adds additional support to the hypothesis, based on orbital dynamics (Kavelaars et al. 2009; Petit et al. 2011), that the inner-belt classical ($a < 39.4$ au classical objects) TNOs are entirely a captured hot population, and the low-*i* members are just the low-inclination tail of the hot distribution. This hypothesis was confirmed in optical colors by Tegler et al. (2016), and we extend this into the infrared. Thus, the cold classical population appears not to exist today for $a < 42.5$ au where it begins (between 39.4 and 42.5 au, the ν_8 secular resonance rapidly removes all low-*i* TNOs).

It is highly desirable to examine the infrared features of the cold classical population, as the members of this population are thought to have formed and remained in the same location throughout their respective lifetimes (Kavelaars et al. 2009; Parker & Kavelaars 2010); it is thus a probe of the formation conditions at this distance (Petit et al. 2011). If any TNO population region should look spectrally distinct, this is the population to study. Unfortunately, we only have measurements for four cold classical objects, of which only three have colors represented in our diagrams. However, we can provide some limited statements. Panel (a) in Figure 15 provides colors for one cold classical (Sila–Nunam) and an upper limit on the color $3.6 \mu\text{m} - 4.5 \mu\text{m}$ for another object (Borasisi). Panel (b) provides colors for Sila–Nunam and an upper limit on the color $3.6 \mu\text{m} - 4.5 \mu\text{m}$ for two objects (Borasisi and 1996 TK₆₆). In these two panels, all cold classical objects appear within the same region; however, note that only Sila–Nunam provides measured colors, as the other two only have $4.6 \mu\text{m}$ upper limits. Panel (c) provides colors for Sila–Nunam and Borasisi, as well as upper limits on both colors for 1996 TK₆₆. In this panel, both objects with colors are located close to each other, and only the one with upper limits is in a region detached from them. Furthermore, agreement appears to exist between all the diagrams regarding the interpretation of the composition of those objects, namely, the colors are consistent with the existence of CH₃OH on their surfaces. This is especially true in the case of Sila–Nunam, which has accurate measurements in all three diagrams. This strongly motivates future work to obtain infrared colors for a sample of cold classical objects; we tentatively hypothesize that they will be found to have features related to the existence of CH₃OH on their surfaces and appear distinct from the other TNO populations (with some overlap in some colors with large objects like Eris and Makemake, due to atmospheric physics).

Interestingly, Grundy et al. (2020) show that the spectra of Arrokoth (also a cold classical object), taken by LEISA on board of New Horizons, has clear CH₃OH absorption bands, but the spectra do not show convincing evidence for H₂O. As mentioned above, our models are consistent with Sila–Nunam containing CH₃OH. In order to explain Arrokoth’s composition, Grundy et al. (2020) propose that temperatures at the formation location of cold classical objects would have been

low enough that volatile CO and CH₄ could freeze onto dust grains in the cold midplane of the nebula (where the sunlight was blocked), enabling production of CH₃OH and perhaps also destruction of H₂O. Once the dust and gas are dissipated from the nebula, the CH₄ volatilizes due to the high equilibrium temperature, leaving only CH₃OH. Thus, the cold population should show signatures of CH₃OH on their surfaces, either in spectra or color. It has been shown by different authors that cold classicals are both brighter (a characteristic of CH₃OH on the spectrum), and redder (because of the tholin material produced by the irradiation of CH₃OH) than other populations (e.g., Brucker et al. 2009; Vilenius et al. 2014). The hypothesis of Grundy et al. (2020) could be tested with new color measurements of cold classicals, but we will need to wait for JWST to achieve the desired sensitivity at the specific wavelengths in which CH₃OH absorption bands can be detected for such a faint population.

12. Conclusions

We present a new method to study the surface composition of small solar system bodies. Using VNIR colors, together with specific broadband photometric measurements beyond 2.2 μm , we have built color–color diagrams in which different materials occupy different regions of the diagram. Using these color–color diagrams, we are able to study very faint objects for which spectroscopic techniques would be either very expensive in time or impossible to carry out. Specifically, the compositional clock can discern compositions that are consistent with mixtures that require small amounts of H₂O and other ices such as CO₂, CH₄, and CH₃OH. The compositional clock also provides a high degree of confidence for the presence of complex organic materials such as tholins. The diagram of $V - 36 \mu\text{m}$ versus $J - 3.6 \mu\text{m}$ also supports this conclusion. A summary of the compositional interpretation made via this method can be found in Table 4.

From the compositional clock, we found that most of the TNOs within our sample (73%), which includes detached, resonant, and classical objects, have colors consistent with surfaces mainly composed of a mixture of H₂O ice, complex organics, and amorphous silicates. Eighty-six percent of the sample have signatures consistent with water ice on their surface, and 23% have or may have CH₄ and/or CH₃OH. Also, 80% have colors consistent with the presence of complex organics. Using other diagrams, we notice that only smaller objects seem to have colors that indicate surfaces dominated by silicates. In agreement with other authors, we also noticed that Haumea’s family members and dwarf planets have a peculiar composition when compared with other TNOs. We are not able to distinguish very clearly between CH₄ and CH₃OH using the compositional clock or the other diagrams. Observations with specific/narrower filters should be carried out in order to be able to distinguish between these two components (as IRAC filters are very wide passbands).

There is currently a lack of measurements for cold classical and detached objects at 4.5 μm , due to the faintness of these specific classes. In this regard, JWST will be advantageous for observing these objects. JWST will have a set of filters specifically for the detection of the different materials discussed in this work (Figure 4); see Kalirai (2018). Thus, JWST will enable similar studies with much fainter objects and will provide additional filters for more specific detections. This

Table 4
Summary of the Different Compositions within Our Sample

Composition	Objects
Dominated by H ₂ O	Haumea
>50% of H ₂ O	Quaoar, Orcus
Dominated by CH ₄	Eris, Makemake
Dominated by silicates	Salacia, 1998 SN ₁₆₅
Presence of CH ₃ OH and/or CH ₄	Sedna, Sila–Nunam, 1999 DE ₉ , 2002 VE ₉₅ , 2002 TX ₃₀₂ .
86% of the sample presents colors consistent with the presence of H ₂ O ice	
80% of the sample presents colors consistent with the presence of complex organics	
93% of the sample presents colors consistent with the presence of amorphous silicates	
23% of the objects in our sample have or may have CH ₄ and/or CH ₃ OH	
Only smaller objects are dominated by silicates	

Note. Statistics are given according to the compositional clock.

capability will be extremely useful to constrain the surface composition of objects within the trans-Neptunian region.

E. F.-V. acknowledges support from the 2017 Preminent Postdoctoral Program (P³) at UCF and the “Earth and Space Based Studies in Support of NASA Space Missions” under the Space Research Initiative (SRI) Program at FSI. B. G. and C. v. L. acknowledge funding support from NSERC. N. P.-A. acknowledges funding support from the Spitzer Space Telescope, operated by the Jet Propulsion Laboratory, California, and from the SRI/FSI project “Digging-up Ice Rocks In The Solar System.” T. M. has received funding from the European Union Horizon 2020 Research and Innovation Programme, under grant Agreement No. 687378, as part of the project “Small Bodies Near and Far” (SBNF). This work is based on observations made with the Spitzer Space Telescope, which is operated by the Jet Propulsion Laboratory, California Institute of Technology, under a contract with NASA. Support for this work was provided by NASA. We acknowledge Raúl Carballo-Rubio and the anonymous referees for providing useful comments that helped improve this manuscript.

Appendix A Individual Analysis of the Sample

In the following, we analyze and provide the surface composition for each object individually. All proportions for different materials are calculated using the diagram $K - 3.6 \mu\text{m}$ versus $3.6 \mu\text{m} - 4.5 \mu\text{m}$, also referred to as the compositional clock (unless otherwise indicated in the text):

1. The spectra of 1996 GQ₂₁ was studied by Doressoundiram et al. (2003), who found no water detection. Later, Barkume et al. (2008) obtained a new spectrum, claiming a detection of water at the 3σ level, which was later supported by Barucci et al. (2011). Barkume et al. (2008) also suggested the presence of CH₃OH. Our measurements for this object provide only an upper limit for the color index $3.6 \mu\text{m} - 4.5 \mu\text{m}$. However, this limit constrains the region in which the object is localized within the diagram, eliminating the possibility of having ices other than water. Nonetheless, it is possible that large

- amounts of water could be hiding the CH_3OH , as in the case of Orcus (see Section 6.2).
2. No spectrum has yet been published for 1998 SN₁₆₅ in the literature. Its location in the Figure 9 indicates that the surface of this object is dominated by silicates, with a small probability of the presence of water ice (taking into account the error bars). We obtain a proportion of $90 \pm 20\%$ silicates, $10 \pm 10\%$ H_2O , and no organics. Note that this object is an inner-belt classical object with a heliocentric ecliptic inclination of $i = 4^\circ 6'$; we compute a free inclination (with respect to the local forced plane) of $3^\circ 5'$. The fact that this object appears similar to hot classicals despite a low i provides evidence for Section 11's argument for a "hot only" inner classical belt.
 3. Several authors have reported 1999 DE₉ to have tentative water ice bands in its spectrum (Jewitt & Luu 2001; Brown et al. 2007b; Barkume et al. 2008). Counter to this, Alvarez-Candal et al. (2007) published a spectrum with no indications of water related bands, however, they mentioned that the absorption bands that the other authors found were placed at $2 \mu\text{m}$, a region of the spectrum that they had to remove due to the strong atmospheric absorption. Nonetheless, this object appears in a region of the compositional clock where there is no presence of water ice but CH_4 or CH_3OH . In fact, 1999 DE₉ was reported by Jewitt & Luu (2001) to have features near 1.4 and $2.25 \mu\text{m}$ similar to what is found in the centaur Pholus, for which they interpreted the presence of solid CH_3OH on its surface (although they claim that the spectrum was not good enough for them to definitively make this identification). As this object has a diameter of ~ 300 km (Lellouch et al. 2013), we discard the possibility of having CH_4 (see Section 8.3). Therefore, our measurements are consistent with the detection of CH_3OH on its surface. We obtain a composition of $20 \pm 10\%$ H_2O , $60 \pm 10\%$ CH_3OH , and $20 \pm 10\%$ organics.
 4. We only provide measurements at $3.6 \mu\text{m}$ for 1999 OC₄. However, inspecting its spectrophotometric measurements, this object is red and has an absorption band at $3.6 \mu\text{m}$ with respect to the K band. As no absorptions are found at VNIR wavelengths, and due to its deep slope, such an absorption band should be due to complex organics. Considering the diagram $V - 3.6 \mu\text{m}$ versus $J - 3.6 \mu\text{m}$, we obtain a composition of $40 \pm 50\%$ H_2O , $0 \pm 30\%$ silicates, and $60 \pm 50\%$ organics. Note that this object is an inner-belt classical object with a heliocentric ecliptic inclination of $i = 4^\circ 0'$ for which we compute a free inclination of $2^\circ 3'$.
 5. The published spectra for 2000 GN₁₇₁ have presented conflicting interpretations about the presence of water. De Bergh et al. (2004) found an absorption band at $\sim 1.6 \mu\text{m}$ that they reported to be related to water. However, Alvarez-Candal et al. (2007) obtained a spectrum of this object where no water bands were present. Later, Barkume et al. (2008) modeled a new spectra of 2000 GN₁₇₁ that included 10% of water. Finally, Guilbert et al. (2009) presented another spectrum that is in agreement with the one published by Alvarez-Candal et al. (2007). In the compositional clock, the position of this object corresponds to a composition of $20 \pm 20\%$ H_2O , $40 \pm 20\%$ silicates, and $40 \pm 20\%$ organics.
 6. The literature contains no published spectrum for 2000 PE₃₀. The position of this object in the diagram is consistent with a composition of $20 \pm 10\%$ H_2O , $60 \pm 20\%$ silicates, and $30 \pm 10\%$ organics.
 7. We only provide upper limit measurements of 2001 QT₃₂₂ at 3.6 and $4.5 \mu\text{m}$. However, this object appears similar to hot classicals despite a low i ($1^\circ 8'$, with a free inclination of $2^\circ 4'$). This object provides evidence for Section 11's argument for a "hot only" inner classical belt.
 8. Doressoundiram et al. (2005) and Barkume et al. (2008) both obtained the spectrum of 2002 AW₁₉₇ and both reported a very small fraction of water. However, Guilbert et al. (2009) also observed this object, and they suggested that the band found at $2 \mu\text{m}$ is related to incomplete removal of telluric features. Its position in the compositional clock corresponds to a composition of $20 \pm 10\%$ H_2O , $60 \pm 10\%$ silicates, and $20 \pm 10\%$ organics.
 9. Barkume et al. (2008) and Guilbert et al. (2009) studied 2002 KX₁₄, with no apparent detection of H_2O -ice bands in the spectra. Considering the diagram $3.6 \mu\text{m} - 4.5 \mu\text{m}$ versus $V - 3.6 \mu\text{m}$, we obtain a composition of $20 \pm 10\%$ H_2O , $60 \pm 10\%$ silicates, and $20 \pm 10\%$ organics, in agreement with previous reports. Note that this object is an inner-belt classical object with a heliocentric ecliptic inclination of $i = 0^\circ 4'$; we compute a free inclination (with respect to the local forced plane) of $2^\circ 7'$. The fact that this object appears similar to hot classicals despite a low i provides evidence for Section 11's argument for a "hot only" inner classical belt.
 10. There are tentative reports that 2002 TC₃₀₂ has water ice (Barkume et al. 2008; Barucci et al. 2011). Stansberry et al. (2008) also suggested that this object has very little fresh ice on its surface. Our results agree with both conclusions, with a composition of $20 \pm 10\%$ H_2O , $30 \pm 20\%$ silicates, and $50 \pm 20\%$ organics. For a mixture of H_2O - CH_3OH -organics, we obtain $40 \pm 20\%$, $30 \pm 10\%$, and $30 \pm 30\%$, respectively; however, those amounts of H_2O should have been detected in its VNIR spectrum. Also, the visible colors of this object are very red (see Appendix B), indicating that a higher presence of complex organics is more likely.
 11. The published spectra for 2002 UX₂₅ has presented conflicting interpretations. Barkume et al. (2008) suggested a small fraction, 6%, of water on its surface. Later, Barucci et al. (2011) obtained a new spectrum and reported no water bands. However, its position corresponds to a composition of $20 \pm 10\%$ H_2O , $50 \pm 10\%$ silicates, and $30 \pm 10\%$ organics, similar to 2002 AW₁₉₇.
 12. Object 2002 VE₉₅ has a strong detection of CH_3OH (Barucci et al. 2006) and our measurements are in agreement with this detection. This object was discussed in Section 6.2. We obtain a composition of $20 \pm 10\%$ H_2O , $40 \pm 10\%$ CH_3OH , and $40 \pm 20\%$ organics.
 13. Object 2003 QA₉₂ only presents measurements at $3.6 \mu\text{m}$. The lack of infrared data prevents us from proving or disproving the existence of absorption bands. Note that

- this object is an inner-belt classical object with a heliocentric ecliptic inclination of $i = 3^\circ.4$ for which we compute a free inclination of $2^\circ.4$.
14. Object 2004 EW₉₅ was studied by Seccull et al. (2018). They demonstrated that its composition is “consistent” with a C-type asteroid and the spectrum present a clear feature produced by hydrated, iron-rich silicates. Considering the diagram $V - 3.6 \mu\text{m}$ versus $J - 3.6 \mu\text{m}$, we obtain a composition of $10 \pm 10\%$ H₂O, $80 \pm 10\%$ silicates, and $10 \pm 10\%$ organics.
 15. Object 2004 NT₃₃ has been studied by several authors, who are in agreement that there is no detection of water (Barkume et al. 2008; Barucci et al. 2011). We obtain a composition of $20 \pm 40\%$ H₂O, $80 \pm 60\%$ silicates, and $0 \pm 20\%$ organics. Additionally, the presence of CO₂ on its surface is also a possibility. CO₂ has been previously detected on the surface of Iapetus (Saturn’s moon), where H₂O ice and complex organics coexist (e.g., Palmer & Brown 2008; Pinilla-Alonso et al. 2011). CO₂ could originate as a byproduct of the interaction of these two materials.
 16. Object 2004 TY₃₆₄ has been reported to tentatively have water ice (Barkume et al. 2008; Barucci et al. 2011). Barucci et al. (2011) measured a depth for the band of 5.8%, in agreement with previous works (e.g., Barkume et al. 2008). Additionally, Merlin et al. (2012) found a band at $2.27 \mu\text{m}$ in the spectrum of 2004 TY₃₆₄, which could be associated with methanol. The position of this object in the compositional clock corresponds to a composition of $20 \pm 10\%$ H₂O, $50 \pm 10\%$ silicates, and $30 \pm 10\%$ organics. However, if we consider a mixture of H₂O, CH₃OH, and organics, we obtain proportions of $50 \pm 10\%$, $30 \pm 10\%$, and $20 \pm 10\%$ for each material, respectively, which would increase the amount of H₂O too much for it not to have been clearly detected in its spectrum.
 17. Object 2005 RM₄₃ has been studied spectroscopically by Fornasier et al. (2009) and Barucci et al. (2011). No water detection was obtained by Fornasier et al. (2009), but tentative detection was reported by Barucci et al. (2011), who model the spectra using up to $\sim 40\%$. The position of this object in Figure 9 is quite interesting, as this region is the one dominated by CO₂. However, error bars are quite large and could easily place the object in a region where the surface would be completely dominated by water. Nonetheless, such amount of H₂O should be detected by VNIR spectroscopy, which is not the case. Other color–color diagrams support the possibility of this object having CO₂ (see Section 7). For a mixture of H₂O, silicates and organics, we obtain a proportion of $50 \pm 40\%$, $50 \pm 40\%$, and 0% for each material, respectively.
 18. Object 2005 RN₄₃ has been reported to not have water ice on its surface by Barkume et al. (2008) and Guilbert et al. (2009); however, its position in Figure 9 indicates that this object is composed of $20 \pm 10\%$ H₂O, $50 \pm 10\%$ silicates, and $30 \pm 10\%$ organics.
 19. Object 2007 JJ₄₃ was studied by Gourgeot et al. (2015). They proposed a surface composition of around 50% of complex organics and up to 6.5% water. Our measurements result in a composition of $40 \pm 30\%$ H₂O, $40 \pm 20\%$ silicates, and $20 \pm 10\%$ organics.
 20. Borasisi’s spectrum was published in Barkume et al. (2008). They obtained a spectral slope of $28.67 \pm 3.61\%/100 \text{ nm}$ and no absorption bands. In our data, Borasisi has only upper limit measurements in the color index $3.6 \mu\text{m} - 4.5 \mu\text{m}$, and due to its position in the compositional clock, no strong conclusions can be drawn about the composition of this object. However, the color index $K - 3.6 \mu\text{m}$ indicates that there is an absorption band that may be either related to ices or complex organics. Also, considering the diagram $V - 3.6 \mu\text{m}$ versus $J - 3.6 \mu\text{m}$, we obtain a composition of $30 \pm 50\%$ H₂O, $40 \pm 30\%$ silicates, and $30 \pm 20\%$ organics.
 21. The spectrum of Huya has been studied by Licandro et al. (2001), Jewitt & Luu (2001), and Fornasier et al. (2004a), with the conclusion that no water ice is observed. Nonetheless, Jewitt & Luu (2001) suggested the possibility of a wide absorption band near $2.0 \mu\text{m}$ that could be related to water. In Figure 9, the position of this object indicates a proportion of $40 \pm 20\%$ H₂O, $30 \pm 10\%$ silicates, and $30 \pm 10\%$ organics.
 22. Barucci et al. (2008), Delsanti et al. (2010), and DeMeo et al. (2010) suggested the presence of methane and their irradiated products on the surface of Orcus. We obtain a composition of $70 \pm 10\%$ H₂O, $20 \pm 10\%$ silicates, and $10 \pm 10\%$ organics. Due to the large amount of water ice found in this object, we are unable to detect methane or the irradiated products with our method, and therefore we do not exclude CH₄ as part of its composition. DeMeo et al. (2010) also suggested the possibility of the presence of CO₂, and due to the position of this object in Figure 11, close to the region dominated by CO₂, we also support this possibility.
 23. The spectrum of Quaoar has been studied in detail by Dalle Ore et al. (2009) using VNIR spectroscopic and IRAC data. Those authors reported the presence of H₂O ice and CH₄. Our measurements agree with the results from Dalle Ore et al. (2009), and we report a composition of $60 \pm 10\%$ H₂O, $20 \pm 10\%$ silicates, and $20 \pm 10\%$ organics. The high percentage of water prevents from clearly detecting the presence of CH₄. Thus, Quaoar could be a good reference for objects with similar spectra.
 24. Schaller & Brown (2008) reported that the fraction of water ice in the surface of Salacia is consistent with zero, which is in a very good agreement with our measurements (see Figure 7(a)). Its position in the compositional clock suggests that the surface of Salacia is dominated by silicates and depleted from ices. We obtain a composition of $10 \pm 10\%$ H₂O, $90 \pm 20\%$ silicates, and no organics.
 25. The spectrum of Sila–Nunam has been studied by Grundy et al. (2005), who found no water bands. The reanalysis conducted by Barucci et al. (2011) for the spectrum published by Grundy et al. (2005) is in agreement. Grundy et al. (2005) reported a neutral spectrum with no strong evidence for H₂O or CH₄, although they noticed a dip around $2.33 \mu\text{m}$ that may arise from absorption by an organic ice. Our measurements indicate the presence of CH₄ or CH₃OH on the surface of Sila–Nunam. Due to the small size of the binary system (around 340 km; Vilenius et al. 2012), it is unlikely that this object possesses CH₄ on its surface and it is more realistic to think that its position in Figure 11 is due to CH₃OH. We obtain a

composition of $30 \pm 10\%$ H₂O, $50 \pm 10\%$ CH₃OH, and $20 \pm 10\%$ organics.

26. Varda's spectrum has been studied by Barucci et al. (2011), whose results are in good agreement with its position in the compositional clock. We obtain a composition of $20 \pm 10\%$ H₂O, $60 \pm 10\%$ silicates, and $30 \pm 10\%$ organics.
27. Objects 2001 UR₁₆₃ and 2004 GV₉ are both located within the pink circle in Figure 9. The spectra of these two objects were studied by Barkume et al. (2008), Barucci et al. (2011), and Guilbert et al. (2009). We obtain a composition of $20 \pm 10\%$ H₂O, $60 \pm 20\%$ silicates, and $20 \pm 20\%$ organics for 2001 UR₁₆₃, and $20 \pm 10\%$ H₂O, $60 \pm 20\%$ silicates, and $20 \pm 10\%$ organics for 2004 GV₉.
28. G!kúnll'hòmdímà was studied by Barucci et al. (2011), who reported water detection. We can analyze this object considering the diagram and $V - 3.6 \mu\text{m}$ versus $3.6 \mu\text{m} - 4.5 \mu\text{m}$, for which we obtain a composition of $20 \pm 50\%$ H₂O, $10 \pm 20\%$ silicates, and $70 \pm 50\%$ organics.

The following objects have no spectrum published in the literature. Considering the diagram $V - 3.6 \mu\text{m}$ versus $J - 3.6 \mu\text{m}$, we obtain surface compositions as follows:

1. 2000 GP₁₈₃: $10 \pm 10\%$ H₂O, $80 \pm 10\%$ silicates, and $10 \pm 10\%$ organics.
2. 2000 QL₂₅₁: $10 \pm 10\%$ H₂O, $90 \pm 10\%$ silicates, and $10 \pm 10\%$ organics.
3. 2001 CZ₃₁: $10 \pm 10\%$ H₂O, $80 \pm 10\%$ silicates, and $10 \pm 10\%$ organics.
4. 2001 QJ₁₈₁: no H₂O, $90 \pm 10\%$ silicates, $10 \pm 10\%$, and organics.
5. 2002 CY₂₂₄: no H₂O, $90 \pm 10\%$ silicates, $10 \pm 10\%$, and organics.

Appendix B

Spectrophotometric Measurements Plotted for Each Object

Here we present the spectrophotometric measurements of our sample in Figure B1. Purple asterisks indicate VNIR measurements from the literature. Red circles and green stars depict Spitzer measurements (blue and yellow triangles are for objects with more than two measurements). Arrows indicate when measurements are upper limits. When available, we also plotted the spectrum or the spectrum model, depicted by lines (references are indicated on the plots). The figures are ordered by provisional designation in ascending order, followed by the named objects in alphabetical order.

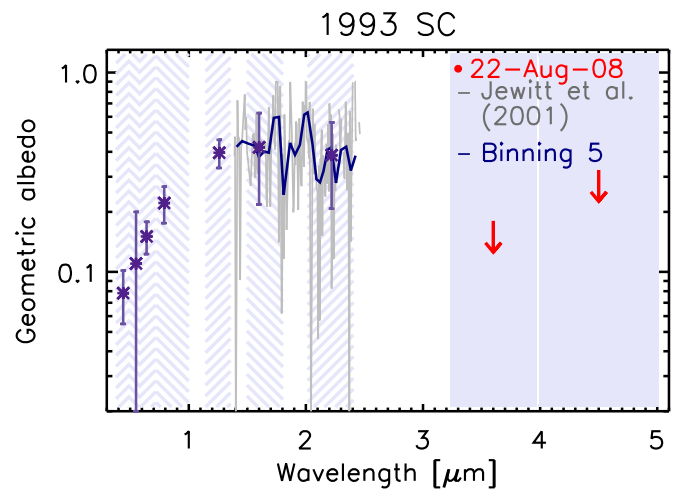


Figure B1. The spectrophotometric measurements of 1993 SC. (The complete figure set (100 images) is available.)

Appendix C

Compiled physical properties used in this work and results from Spitzer (Tables C1–C5).

Table C1
Summary of Observations

Designation	Date (DD/MM/YY)	Δ (au)	r_H (au)	α (deg)	$F_{3.6 \mu m}$ (μJy)	$F_{4.5 \mu m}$ (μJy)	$P_{3.6 \mu m}$	$P_{4.5 \mu m}$
1993 SC	22-Aug-8	36.335	36.329	1.615	<1.4	<1.7	<0.2	<0.3
1995 SM ₅₅	25-Oct-10	38.109	38.572	1.372	2.6 ± 0.9	...	0.21 ± 0.08	...
	27-Oct-10	38.080	38.571	1.349	2.8 ± 0.6	...	0.23 ± 0.05	...
1995 TL ₈	03-Mar-11	43.670	44.145	1.155	2.0 ± 0.3	...	0.22 ± 0.05	...
1996 GQ ₂₁	07-Aug-7	40.254	40.656	1.329	3.8 ± 0.5	1.3	0.15 ± 0.03	<0.08
1996 TK ₆₆	04-Sep-9	42.827	42.988	1.352	<1.8	...	<0.75	...
	08-Sep-9	42.761	42.988	1.337	<2.3	...	<1.0	...
1996 TO ₆₆	22-Dec-5	46.094	46.486	1.151	<2.0	<2.3	<0.46	<0.79
	25-Dec-5	46.142	46.486	1.173	<1.1	<2.2	<0.24	<0.76
1996 TP ₆₆	10-Mar-8	26.772	26.926	2.114	<2.4	<2.1	<0.10	<0.14
	11-Mar-8	26.789	26.926	2.119	<2.4	<1.8	<0.10	<0.11
1998 SM ₁₆₅	14-Mar-12	38.350	38.590	1.453	1.9 ± 0.4	...	0.09 ± 0.02	...
	17-Mar-12	38.403	38.593	1.468	2.1 ± 0.4	...	0.10 ± 0.02	...
1998 SN ₁₆₅	29-Jan-10	37.438	37.750	1.463	7.3 ± 1.1	4.4 ± 0.5	0.17 ± 0.03	0.16 ± 0.03
	03-Feb-10	37.520	37.750	1.495	3.0 ± 0.5	3.2 ± 0.6	0.07 ± 0.02	0.11 ± 0.03
1998 VG ₄₄	20-Nov-11	29.392	29.390	1.999	2.6 ± 1.2	...	0.06 ± 0.03	...
1999 CD ₁₅₈	12-Jun-12	46.828	47.229	1.121	2.0 ± 0.3	...	0.15 ± 0.04	...
1999 DE ₉	29-Dec-5	35.073	35.146	1.645	7.2 ± 0.9	12.9 ± 5.8	0.21 ± 0.04	0.57 ± 0.27
	26-Dec-5	35.121	35.143	1.649	4.9 ± 0.7	...	0.14 ± 0.03	...
1999 OJ ₄	06-Dec-9	37.460	37.989	1.322	0.6 ± 0.8	...	0.09 ± 0.14	...
	11-Dec-9	37.535	37.989	1.382	0.2 ± 0.5	...	0.03 ± 0.08	...
2000 CN ₁₀₅	26-Jun-10	46.157	46.571	1.137	<2.5	<1.5	<0.34	<0.30
	01-Jul-10	46.237	46.573	1.177	<3.8	<1.3	<0.51	<0.27
2000 GN ₁₇₁	10-Aug-6	28.344	28.372	2.066	2.9 ± 0.6	3.2 ± 1.0	0.17 ± 0.05	0.28 ± 0.10
	14-Aug-6	28.410	28.371	2.064	3.9 ± 0.6	2.7 ± 0.7	0.23 ± 0.06	0.24 ± 0.08
2000 GP ₁₈₃	04-Sep-9	36.807	36.989	1.563	3.0 ± 0.4	...	0.16 ± 0.04	...
	07-Sep-9	36.857	36.988	1.575	3.8 ± 0.5	...	0.20 ± 0.05	...
2000 OK ₆₇	13-Jan-10	40.175	40.318	1.427	<1.7	<1.7	<0.31	<0.45
	17-Jan-10	40.242	40.318	1.436	<3.6	<1.4	<0.65	<0.39
2000 PE ₃₀	14-Nov-7	37.812	38.210	1.415	2.5 ± 0.5	2.8 ± 0.7	0.14 ± 0.04	0.23 ± 0.07
	18-Nov-7	37.878	38.212	1.450	3.0 ± 0.5	2.4 ± 0.5	0.17 ± 0.04	0.20 ± 0.06
2000 QL ₂₅₁	29-Jan-10	39.041	39.281	1.434	2.0 ± 0.6	...	0.28 ± 0.10	...
	03-Feb-10	39.127	39.283	1.456	2.4 ± 0.7	...	0.34 ± 0.13	...
2000 YW ₁₃₄	14-Jan-12	44.380	44.525	1.299	4.0 ± 0.4	...	0.18 ± 0.03	...
	19-Jan-12	44.300	44.528	1.279	3.9 ± 0.5	...	0.17 ± 0.03	...
2001 CZ ₃₁	20-Jan-11	40.519	40.626	1.425	3.1 ± 0.4	...	0.22 ± 0.05	...
	24-Jan-11	40.451	40.625	1.413	3.1 ± 0.4	...	0.22 ± 0.05	...
2001 QC ₂₉₈	25-Dec-9	40.144	40.655	1.244	<3.1	...	<0.16	...
	28-Dec-9	40.189	40.655	1.278	1.1 ± 0.6	...	0.06 ± 0.03	...
2001 QF ₂₉₈	10-Sep-11	42.797	43.176	1.269	2.3 ± 0.8	...	0.08 ± 0.03	...
2001 QS ₃₂₂	23-Jan-10	42.111	42.357	1.330	0.7 ± 0.6	1.8	0.11 ± 0.11	<0.46
	28-Jan-10	42.196	42.357	1.351	0.7 ± 0.5	1.8	0.12 ± 0.09	<0.46
2001 QT ₃₂₂	23-Jan-10	36.704	37.031	1.485	<3.2	<2.4	<0.43	<0.49
	28-Jan-10	36.786	37.031	1.520	<5.3	<1.3	<0.71	<0.27
2001 RZ ₁₄₃	05-Sep-9	41.281	41.308	1.422	0.7 ± 0.6	...	0.20 ± 0.16	...
	10-Sep-9	41.197	41.308	1.416	1.8 ± 1.5	...	0.48 ± 0.41	...
2001 UR ₁₆₃	17-Aug-8	50.597	50.481	1.152	4.1 ± 0.4	3.5 ± 0.8	0.38 ± 0.06	0.51 ± 0.13
	21-Aug-8	50.533	50.484	1.160	5.7 ± 0.5	5.1 ± 0.7	0.54 ± 0.08	0.73 ± 0.14
2001 XD ₂₅₅	02-Jan-12	39.308	39.467	1.466	3.0 ± 0.5	...	0.14 ± 0.04	...
	06-Jan-12	39.240	39.466	1.448	3.2 ± 0.5	...	0.15 ± 0.04	...
2001 YH ₁₄₀	02-Jan-12	36.608	36.674	1.591	3.6 ± 0.7	...	0.10 ± 0.02	...
	06-Jan-12	36.541	36.675	1.581	2.4 ± 0.6	...	0.07 ± 0.02	...
2002 AW ₁₉₇	20-Dec-8	46.580	46.566	1.251	11.1 ± 0.5	10.0 ± 1.3	0.16 ± 0.02	0.22 ± 0.04
	24-Dec-8	46.512	46.564	1.250	11.2 ± 0.4	7.5 ± 1.6	0.16 ± 0.02	0.16 ± 0.04
2002 CY ₂₂₄	22-Jun-12	37.117	37.644	1.312	1.5 ± 0.3	...	0.37 ± 0.11	...
	26-Jun-12	37.178	37.646	1.365	1.8 ± 0.3	...	0.45 ± 0.12	...
2002 GV ₃₁	25-Jun-10	39.769	40.283	1.243	<2.7	<1.1	<0.22	<0.13
	26-Aug-16	39.684	40.117	1.312	<1.4	...	<0.1	...

Table C1
(Continued)

Designation	Date (DD/MM/YY)	Δ (au)	r_H (au)	α (deg)	$F_{3.6 \mu m}$ (μJy)	$F_{4.5 \mu m}$ (μJy)	$P_{3.6 \mu m}$	$P_{4.5 \mu m}$
2002 KX ₁₄	26-Aug-16	39.684	40.117	1.312	<0.9	...	<0.1	...
	16-Sep-8	39.242	39.486	1.447	5.7 \pm 0.8	3.7 \pm 1.6	0.12 \pm 0.02	0.12 \pm 0.05
2002 TC ₃₀₂	20-Sep-8	39.307	39.486	1.467	6.1 \pm 1.0	4.4 \pm 1.1	0.13 \pm 0.03	0.14 \pm 0.04
	15-Sep-8	46.572	46.822	1.222	4.9 \pm 0.4	3.2 \pm 0.4	0.12 \pm 0.02	0.12 \pm 0.02
2002 TX ₃₀₀	18-Sep-8	46.521	46.820	1.207	4.0 \pm 0.7	4.6 \pm 0.5	0.10 \pm 0.02	0.18 \pm 0.03
	17-Aug-8	41.362	41.397	1.417	2.7 \pm 0.3	2.3 \pm 0.5	0.14 \pm 0.03	0.18 \pm 0.04
2002 UX ₂₅	19-Aug-8	41.331	41.397	1.415	3.3 \pm 0.6	1.9 \pm 1.1	0.17 \pm 0.04	0.15 \pm 0.09
	18-Sep-8	41.517	41.866	1.328	9.4 \pm 0.3	7.4 \pm 1.3	0.11 \pm 0.01	0.13 \pm 0.03
2002 VE ₉₅	21-Sep-8	41.468	41.865	1.304	9.4 \pm 0.5	7.7 \pm 1.0	0.11 \pm 0.01	0.13 \pm 0.02
	22-Oct-5	27.347	28.093	1.449	6.6 \pm 0.5	8.1 \pm 0.8	0.11 \pm 0.02	0.21 \pm 0.04
2002 VR ₁₂₈	23-Oct-5	27.336	28.093	1.425	6.2 \pm 0.4	6.2 \pm 1.3	0.11 \pm 0.02	0.16 \pm 0.04
	23-Oct-11	37.695	37.924	1.518	4.5 \pm 0.5	...	0.08 \pm 0.01	...
2002 VT ₁₃₀	26-Oct-11	37.649	37.926	1.500	5.1 \pm 0.6	...	0.09 \pm 0.02	...
	30-Oct-9	42.611	42.862	1.335	<1.5	...	<0.09	...
2002 WC ₁₉	03-Nov-9	42.547	42.862	1.311	<0.8	...	<0.0	...
	11-Nov-11	41.996	42.008	1.400	3.7 \pm 0.6	...	0.17 \pm 0.03	...
2002 XV ₉₃	14-Nov-11	41.944	42.006	1.398	4.3 \pm 0.5	...	0.20 \pm 0.03	...
	19-Nov-11	39.465	39.514	1.486	5.9 \pm 0.7	...	0.09 \pm 0.02	...
2003 AZ ₈₄	23-Nov-11	39.397	39.513	1.480	5.6 \pm 0.7	...	0.08 \pm 0.01	...
	02-Jun-12	44.824	45.151	1.208	6.3 \pm 0.5	3.8 \pm 0.5	0.09 \pm 0.01	0.08 \pm 0.01
2003 FE ₁₂₈	05-Jun-12	44.871	45.150	1.227	5.2 \pm 0.4	3.5 \pm 0.6	0.07 \pm 0.01	0.07 \pm 0.01
	09-Sep-11	35.421	35.860	1.482	0.6 \pm 0.5	...	0.13 \pm 0.12	...
2003 FY ₁₂₈	13-Sep-11	35.483	35.860	1.525	1.3 \pm 0.9	...	0.29 \pm 0.22	...
	05-Mar-11	38.853	38.857	1.485	6.7 \pm 0.8	5.2 \pm 0.4	0.13 \pm 0.02	0.16 \pm 0.03
2003 OP ₃₂	09-Mar-11	38.786	38.859	1.482	4.4 \pm 0.5	3.9 \pm 0.4	0.09 \pm 0.02	0.12 \pm 0.02
	23-Nov-7	40.874	41.283	1.301	1.6 \pm 0.5	2.5	0.11 \pm 0.03	<0.26
2003 QA ₉₂	06-Jan-10	37.346	37.432	1.549	2.4 \pm 0.8	...	0.26 \pm 0.11	...
2003 QR ₉₁	28-Nov-9	38.698	39.221	1.288	5.7 \pm 0.8	...	0.30 \pm 0.06	...
	03-Dec-9	38.775	39.222	1.345	6.2 \pm 0.3	...	0.33 \pm 0.05	...
2003 QW ₉₀	09-Apr-16	43.538	43.552	1.324	2.0 \pm 0.6	...	0.08 \pm 0.03	...
	10-Apr-16	43.555	43.552	1.324	2.7 \pm 0.8	...	0.11 \pm 0.03	...
2003 UT ₂₉₂	01-Nov-11	29.066	29.090	2.022	2.1 \pm 0.4	...	0.08 \pm 0.02	...
	03-Nov-11	29.033	29.089	2.021	1.9 \pm 0.5	...	0.08 \pm 0.02	...
2003 UY ₁₁₇	23-Oct-11	32.400	32.857	1.616	4.2 \pm 0.6	...	0.15 \pm 0.03	...
	26-Oct-11	32.356	32.858	1.576	4.2 \pm 0.5	...	0.14 \pm 0.03	...
2003 UZ ₄₁₃	29-Oct-10	42.091	42.575	1.228	6.6 \pm 0.7	...	0.08 \pm 0.01	...
	31-Oct-10	42.064	42.576	1.206	7.1 \pm 0.7	...	0.09 \pm 0.01	...
2003 VS ₂	19-Oct-7	36.017	36.441	1.479	12.3 \pm 0.4	8.9 \pm 1.0	0.14 \pm 0.02	0.16 \pm 0.03
	22-Oct-7	35.973	36.441	1.445	14.5 \pm 0.4	10.2 \pm 0.6	0.17 \pm 0.02	0.18 \pm 0.03
2004 EW ₉₅	04-Sep-11	27.080	27.330	2.085	5.7 \pm 0.8	...	0.07 \pm 0.02	...
	08-Sep-11	27.144	27.329	2.114	6.2 \pm 0.6	...	0.08 \pm 0.02	...
2004 GV ₉	12-Sep-10	39.070	39.190	1.488	10.8 \pm 1.3	11.2 \pm 1.4	0.10 \pm 0.02	0.16 \pm 0.03
	15-Sep-10	39.119	39.190	1.494	13.6 \pm 2.3	11.8 \pm 1.8	0.13 \pm 0.03	0.17 \pm 0.03
2004 NT ₃₃	29-Nov-10	37.769	38.297	1.317	9.2 \pm 0.9	4.1 \pm 0.6	0.19 \pm 0.03	0.13 \pm 0.03
	30-Nov-10	37.781	38.297	1.327	10.4 \pm 2.1	6.2 \pm 0.8	0.22 \pm 0.05	0.20 \pm 0.04
2004 PF ₁₁₅	14-Dec-10	40.935	41.425	1.242	4.5 \pm 1.0	...	0.11 \pm 0.03	...
	16-Dec-10	40.964	41.425	1.263	5.6 \pm 0.8	...	0.13 \pm 0.02	...
2004 PG ₁₁₅	18-Jul-11	36.908	36.994	1.568	4.1 \pm 1.1	1.2	0.08 \pm 0.03	<0.04
	20-Jul-11	36.876	36.995	1.564	<3.6	<1.4	<0.07	<0.04
2004 PT ₁₀₇	01-Mar-16	38.293	38.223	1.514	3.4 \pm 0.5	...	0.08 \pm 0.02	...
	02-Mar-16	38.310	38.223	1.512	3.3 \pm 0.5	...	0.08 \pm 0.02	...
2004 TY ₃₆₄	18-Sep-11	39.464	39.418	1.487	6.1 \pm 1.1	6.5 \pm 1.0	0.10 \pm 0.02	0.17 \pm 0.03
	19-Sep-11	39.448	39.418	1.488	7.7 \pm 0.7	5.5 \pm 0.5	0.13 \pm 0.02	0.14 \pm 0.02
2004 UX ₁₀	18-Sep-10	38.881	38.957	1.506	5.4 \pm 1.0	...	0.14 \pm 0.03	...
	21-Sep-10	38.832	38.957	1.500	6.0 \pm 0.9	...	0.16 \pm 0.03	...
2004 VT ₇₅	19-Feb-11	37.393	37.847	1.368	1.4 \pm 0.4	...	0.10 \pm 0.04	...
	19-Feb-11	37.393	37.847	1.368	1.2 \pm 0.4	...	0.08 \pm 0.03	...
2004 XA ₁₉₂	19-Nov-10	35.683	35.729	1.643	11.7 \pm 1.0	10.4 \pm 1.1	0.31 \pm 0.08	0.42 \pm 0.12
	20-Nov-10	35.669	35.728	1.642	11.2 \pm 1.2	11.1 \pm 2.0	0.29 \pm 0.08	0.45 \pm 0.14
2005 CA ₇₉	07-Jan-11	37.164	37.297	1.552	2.2 \pm 0.5	...	0.06 \pm 0.02	...
	10-Jan-11	37.115	37.298	1.541	4.2 \pm 0.6	...	0.11 \pm 0.03	...
2005 GE ₁₈₇	01-Jun-16	28.627	28.609	2.009	1.6 \pm 0.7	...	0.43 \pm 0.21	...
	03-Jun-16	28.593	28.608	2.010	<1.8	...	<0.5	...

Table C1
(Continued)

Designation	Date (DD/MM/YY)	Δ (au)	r_H (au)	α (deg)	$F_{3.6 \mu m}$ (μJy)	$F_{4.5 \mu m}$ (μJy)	$P_{3.6 \mu m}$	$P_{4.5 \mu m}$
2005 RM ₄₃	25-Oct-10	35.261	35.454	1.634	8.0 ± 1.2	3.3 ± 0.4	0.11 ± 0.02	0.07 ± 0.01
	28-Oct-10	35.214	35.455	1.619	7.1 ± 1.1	2.0 ± 0.6	0.10 ± 0.02	0.04 ± 0.01
2005 RN ₄₃	18-Dec-10	40.166	40.681	1.244	12.2 ± 0.9	9.5 ± 0.5	0.13 ± 0.02	0.15 ± 0.02
	21-Dec-10	40.210	40.681	1.278	12.7 ± 0.6	10.5 ± 0.8	0.13 ± 0.02	0.17 ± 0.02
2005 RR ₄₃	25-Oct-10	38.558	38.794	1.481	<3.7	<2.1	<0.17	<0.15
	27-Oct-10	38.527	38.795	1.470	<2.9	<2.6	<0.13	<0.18
2005 RS ₄₃	03-Sep-10	42.284	42.334	1.385	3.2 ± 0.6	...	0.11 ± 0.03	...
	06-Sep-10	42.235	42.336	1.381	2.3 ± 0.6	...	0.08 ± 0.03	...
2005 TB ₁₉₀	07-Jan-11	45.925	46.330	1.155	3.1 ± 0.5	...	0.11 ± 0.02	...
2005 UQ ₅₁₃	10-Sep-10	48.478	48.672	1.188	4.3 ± 1.2	1.8 ± 0.6	0.17 ± 0.05	0.11 ± 0.04
	13-Sep-10	48.432	48.672	1.177	4.5 ± 0.7	4.5 ± 0.8	0.18 ± 0.03	0.28 ± 0.06
2006 QJ ₁₈₁	05-Nov-11	33.867	33.892	1.735	2.7 ± 0.4	...	1.27 ± 0.35	...
	08-Nov-11	33.814	33.890	1.732	2.6 ± 0.4	...	1.22 ± 0.34	...
2007 JF ₄₃	13-Apr-11	38.705	38.713	1.486	2.6 ± 0.5	...	0.09 ± 0.02	...
	17-Apr-11	38.634	38.711	1.483	3.1 ± 0.6	...	0.10 ± 0.03	...
2007 JH ₄₃	24-Apr-11	40.454	40.554	1.413	7.5 ± 0.8	...	0.14 ± 0.03	...
	28-Apr-11	40.385	40.554	1.402	7.4 ± 0.6	...	0.14 ± 0.02	...
2007 JJ ₄₃	21-Sep-11	40.996	41.527	1.213	5.2 ± 0.8	4.8 ± 1.1	0.11 ± 0.02	0.15 ± 0.04
	27-Sep-11	41.084	41.525	1.280	7.4 ± 0.7	3.1 ± 1.3	0.15 ± 0.03	0.10 ± 0.04
2007 OC ₁₀	29-Nov-10	35.034	35.525	1.454	4.1 ± 0.6	...	0.12 ± 0.02	...
2007 XV ₅₀	27-Oct-10	46.290	46.371	1.266	1.5 ± 0.5	...	0.04 ± 0.02	...
	31-Oct-10	46.224	46.372	1.257	4.3 ± 0.4	...	0.13 ± 0.02	...
2008 NW ₄	23-Nov-10	36.266	36.773	1.391	2.5 ± 0.6	...	0.07 ± 0.02	...
	26-Nov-10	36.310	36.773	1.427	1.9 ± 0.4	...	0.06 ± 0.01	...
2008 OG ₁₉	26-Nov-11	38.128	38.602	1.352	3.6 ± 0.5	...	0.07 ± 0.01	...
	29-Nov-11	38.173	38.602	1.384	4.7 ± 0.7	...	0.09 ± 0.02	...
2009 YG ₁₉	29-Dec-15	34.188	34.545	1.603	2.5 ± 0.4	...	0.09 ± 0.03	...
	31-Dec-15	34.158	34.546	1.583	2.2 ± 0.5	...	0.08 ± 0.02	...
2010 ER ₆₅	21-Mar-12	39.959	40.239	1.382	2.4 ± 0.5	...	0.07 ± 0.02	...
2010 ET ₆₅	22-Jul-11	39.168	39.637	1.304	3.3 ± 0.6	...	0.10 ± 0.02	...
2010 FD ₄₉	04-Sep-11	32.021	32.070	1.824	2.2 ± 0.4	...	0.08 ± 0.02	...
	06-Sep-11	32.054	32.069	1.826	3.5 ± 0.4	...	0.13 ± 0.03	...
2010 JC ₈₀	24-May-16	32.724	32.668	1.756	1.5 ± 0.7	2.3	0.05 ± 0.02	<0.11
	25-May-16	32.707	32.668	1.758	<2.1	<1.5	<0.06	<0.07
Borasisi	26-Dec-7	41.286	41.362	1.401	1.6 ± 0.4	2.6	0.33 ± 0.08	<0.80
	31-Dec-7	41.372	41.363	1.402	1.2 ± 0.5	3.3	0.24 ± 0.10	<0.99
Chaos	19-Oct-7	41.522	41.848	1.338	4.2 ± 0.7	4.6 ± 0.7	0.06 ± 0.01	0.11 ± 0.02
Dziewanna	09-Sep-11	38.654	38.795	1.497	7.7 ± 0.8	6.1 ± 0.6	0.17 ± 0.03	0.20 ± 0.03
	10-Sep-11	38.668	38.794	1.500	7.3 ± 0.9	7.6 ± 0.9	0.16 ± 0.03	0.26 ± 0.05
Eris	17-Aug-8	96.747	96.751	0.606	7.6 ± 0.3	18.0 ± 0.9	0.21 ± 0.01	0.75 ± 0.06
	22-Aug-8	96.665	96.750	0.605	6.3 ± 0.3	17.9 ± 0.7	0.17 ± 0.01	0.75 ± 0.05
G'kúnl' hòm dímà	25-Oct-10	44.688	44.870	1.293	3.5 ± 1.2	3.8 ± 0.7	0.07 ± 0.03	0.12 ± 0.03
	27-Oct-10	44.655	44.868	1.286	5.1 ± 6.6	7.5 ± 4.8	0.10 ± 0.13	0.23 ± 0.15
Gonggong	23-Jul-11	86.337	86.381	0.673	4.6 ± 0.9	...	0.28 ± 0.06	...
	30-Jul-11	86.223	86.385	0.667	2.9 ± 0.5	...	0.17 ± 0.03	...
Haumea	16-Dec-10	85.719	86.234	0.584	2.9 ± 0.5	...	0.17 ± 0.03	...
	20-Dec-10	85.781	86.236	0.605	3.1 ± 0.5	...	0.18 ± 0.03	...
Huya	17-Mar-9	50.638	51.069	1.024	28.1 ± 0.7	8.2 ± 0.8	0.22 ± 0.02	0.10 ± 0.01
	19-Mar-9	50.611	51.069	1.009	27.0 ± 0.7	7.3 ± 0.5	0.21 ± 0.02	0.09 ± 0.01
Lempo	10-Aug-6	28.954	29.013	2.019	14.3 ± 1.8	9.4 ± 1.6	0.09 ± 0.02	0.09 ± 0.02
	12-Aug-6	28.986	29.012	2.021	12.8 ± 1.5	6.7 ± 1.5	0.08 ± 0.02	0.07 ± 0.02
Makemake	23-Dec-5	30.558	30.964	1.721	8.2 ± 0.6	6.1 ± 1.9	0.09 ± 0.02	0.10 ± 0.03
	23-Dec-5	30.558	30.964	1.721	8.1 ± 1.0	6.0 ± 2.0	0.09 ± 0.02	0.10 ± 0.04
Orcus	16-Jun-8	51.610	52.059	1.000	18.7 ± 0.5	64.0 ± 0.7	0.12 ± 0.01	0.60 ± 0.06
	18-Jun-8	51.636	52.059	1.014	17.8 ± 0.4	61.4 ± 0.7	0.11 ± 0.01	0.58 ± 0.05
Quaoar	27-Dec-5	47.359	47.711	1.144	10.2 ± 0.3	4.5 ± 0.5	0.10 ± 0.01	0.07 ± 0.01
	29-Dec-5	47.329	47.711	1.130	11.2 ± 0.5	4.0 ± 0.7	0.11 ± 0.01	0.06 ± 0.01
Salacia	15-Sep-5	43.276	43.331	1.353	26.7 ± 0.8	13.2 ± 0.6	0.15 ± 0.02	0.11 ± 0.01
	18-Sep-5	43.326	43.331	1.354	27.3 ± 0.6	15.2 ± 1.7	0.15 ± 0.02	0.13 ± 0.02
Salacia	11-Oct-16	44.455	44.658	1.290	6.5 ± 0.6	4.8 ± 0.8	0.06 ± 0.01	0.06 ± 0.01
	12-Oct-16	44.439	44.658	1.286	7.9 ± 0.9	4.8 ± 0.5	0.07 ± 0.01	0.06 ± 0.01
	23-Jan-10	44.009	44.107	1.308	8.7 ± 1.0	...	0.07 ± 0.01	...
	26-Jan-10	44.057	44.107	1.312	8.5 ± 1.1	...	0.07 ± 0.01	...

Table C1
(Continued)

Designation	Date (DD/MM/YY)	Δ (au)	r_H (au)	α (deg)	$F_{3.6 \mu\text{m}}$ (μJy)	$F_{4.5 \mu\text{m}}$ (μJy)	$p_{3.6 \mu\text{m}}$	$p_{4.5 \mu\text{m}}$
Sedna	05-Feb-6	88.509	88.854	0.607	3.7 ± 0.3	3.9 ± 1.0	0.48 ± 0.05	0.76 ± 0.21
	09-Feb-6	88.569	88.850	0.620	2.8 ± 0.5	3.5 ± 0.6	0.36 ± 0.07	0.68 ± 0.12
Sila–Nunam	07-May-8	43.104	43.522	1.207	0.8 ± 0.3	1.3 ± 0.7	0.04 ± 0.02	0.10 ± 0.05
	09-May-8	43.135	43.522	1.225	2.0 ± 0.8	1.7 ± 0.5	0.11 ± 0.05	0.14 ± 0.04
	24-Jul-16	43.113	43.471	1.244	1.8 ± 0.7	...	0.10 ± 0.04	...
	25-Jul-16	43.129	43.471	1.252	2.1 ± 0.6	...	0.11 ± 0.04	...
Varda	20-May-11	47.281	47.588	1.158	10.6 ± 1.2	9.4 ± 0.7	0.15 ± 0.02	0.21 ± 0.03
	22-May-11	47.250	47.587	1.146	9.4 ± 1.0	8.3 ± 0.5	0.13 ± 0.02	0.18 ± 0.02
Varuna	24-Mar-6	42.791	43.307	1.141	7.7 ± 0.5	6.9 ± 0.8	0.11 ± 0.01	0.14 ± 0.02
	29-Mar-6	42.868	43.307	1.196	8.6 ± 0.5	6.0 ± 0.5	0.12 ± 0.01	0.13 ± 0.02

Note. Abbreviations are defined as follows: geocentric distance (Δ), heliocentric distance (r_H), phase angle (α), flux at 3.6 and 4.5 μm ($F_{3.6 \mu\text{m}}$ and $F_{4.5 \mu\text{m}}$, respectively), geometric albedo at 3.6 and 4.5 μm ($p_{3.6 \mu\text{m}}$ and $p_{4.5 \mu\text{m}}$, respectively).

(This table is available in machine-readable form.)

Table C2
Compilation of the Physical Properties

Designation	p_V	H_V (mag)	D (km)	Taxonomy	S' (%/1000)	Binarity	Dyn. Class.	OB
1993 SC [†]	0.11 ± 0.09	7.00 ± 0.70	160.0 ± 50.0	RR	6.84 ± 4.88	No	Resonant	S
1995 SM ₅₅ [‡]	0.58 ± 0.26	4.49 ± 0.03	220.0 ± 17.0	BBb?	1.27 ± 2.91	No	Inner Classical	S
1995 TL ₈	0.23 ± 0.19	5.29 ± 0.06	244.0 ± 82.0	RR	3.17 ± 6.08	Si	Hot Classical	I
1996 GQ ₂₁	0.13 ± 0.04	5.20 ± 0.30	349.0 ± 49.0	RR	4.74 ± 3.15	No	Detached	I
1996 TK ₆₆ [†]	0.11 ± 0.09	6.10 ± 0.60	120.0 ± 30.0	RR	8.62 ± 4.51	...	Cold Classical	S
1996 TO ₆₆	0.58 ± 0.26	4.81 ± 0.11	190.0 ± 17.0	BBb?	8.12 ± 8.43	HH	Hot Classical	S
1996 TP ₆₆	0.07 ± 0.06	7.51 ± 0.09	154.0 ± 33.0	RR	0.36 ± 4.74	No	Resonant	S
1998 SM ₁₆₅	0.08 ± 0.02	6.02 ± 0.08	291.0 ± 26.0	RR	9.02 ± 4.33	Si	Resonant	S
1998 SN ₁₆₅	0.06 ± 0.02	5.71 ± 0.09	393.0 ± 39.0	BB	8.24 ± 4.91	No	Inner Classical	S
1998 VG ₄₄	0.06 ± 0.03	6.67 ± 0.04	248.0 ± 43.0	IR	9.02 ± 3.08	No	Resonant	S
1999 CD ₁₅₈ [†]	0.11 ± 0.09	5.35 ± 0.67	340.0 ± 100.0	IR	6.73 ± 5.83	No	Hot Classical	S
1999 DE ₉	0.16 ± 0.04	5.16 ± 0.05	311.0 ± 32.0	IR	0.12 ± 2.25	No	Resonant	S
1999 OJ ₄ [†]	0.11 ± 0.09	7.10 ± 0.71	152.0 ± 50.0	RR	7.37 ± 3.21	Si	Inner Classical	S
2000 CN ₁₀₅	0.15 ± 0.07	5.20 ± 0.30	247.0 ± 63.0	RR	7.80 ± 5.69	No	Hot Classical	I
2000 GN ₁₇₁	0.21 ± 0.09	6.45 ± 0.34	147.0 ± 20.0	IR	3.88 ± 2.88	No	Resonant	S
2000 GP ₁₈₃ [†]	0.11 ± 0.09	6.00 ± 0.60	253.0 ± 70.0	BB	8.18 ± 3.45	No	Inner Classical	S
2000 OK ₆₇	0.17 ± 0.16	6.47 ± 0.13	164.0 ± 45.0	RR-U	0.14 ± 4.59	No	Hot Classical	S
2000 PE ₃₀ [†]	0.11 ± 0.09	5.90 ± 0.59	265.0 ± 72.0	BB	2.78 ± 4.11	No	Detached	S
2000 QL ₂₅₁ [†]	0.11 ± 0.09	6.80 ± 0.68	175.0 ± 55.0	BR	1.64 ± 2.46	Si	Resonant	S
2000 YW ₁₃₄ [†]	0.11 ± 0.09	4.88 ± 0.05	400.0 ± 10.0	IR	4.45 ± 3.51	Si	Resonant	S
2001 CZ _{31r} [†]	0.11 ± 0.09	5.90 ± 0.59	265.0 ± 72.0	BB	...	No	Hot Classical	S
2001 QC ₂₉₈	0.06 ± 0.03	6.26 ± 0.32	303.0 ± 30.0	BR	7.90 ± 4.21	Si	Resonant	S
2001 QF ₂₉₈	0.07 ± 0.02	5.43 ± 0.07	408.0 ± 44.0	BB	4.60 ± 4.64	No	Resonant	S
2001 QS ₃₂₂	0.10 ± 0.53	6.91 ± 0.68	186.0 ± 99.0	No	Cold Classical	S
2001 QT ₃₂₂	0.09 ± 0.42	7.29 ± 0.67	159.0 ± 47.0	...	5.58 ± 11.08	No	Inner Classical	S
2001 RZ ₁₄₃	0.19 ± 0.07	6.69 ± 0.13	140.0 ± 39.0	...	3.26 ± 7.24	Si	Hot Classical	I
2001 UR ₁₆₃	0.21 ± 0.08	4.10 ± 0.30	352.0 ± 85.0	RR-U	2.52 ± 4.66	No	Resonant	S
2001 XD ₂₅₅ [†]	0.11 ± 0.09	5.60 ± 0.56	304.0 ± 78.0	No	Resonant	S
2001 YH ₁₄₀	0.08 ± 0.05	5.80 ± 0.20	349.0 ± 81.0	IR	7.01 ± 3.18	No	Resonant	S
2002 AW ₁₉₇	0.11 ± 0.01	3.57 ± 0.05	768.0 ± 39.0	IR	3.45 ± 3.25	No	Hot Classical	S
2002 CY ₂₂₄ [†]	0.11 ± 0.09	6.10 ± 0.60	120.0 ± 30.0	RR	0.91 ± 2.70	...	Resonant	S
2002 GV ₃₁ [†]	0.11 ± 0.09	6.10 ± 0.60	240.0 ± 70.0	No	Hot Classical	S
2002 KX ₁₄	0.10 ± 0.01	4.86 ± 0.10	455.0 ± 27.0	...	3.82 ± 2.06	No	Inner Classical	S
2002 TC ₃₀₂	0.12 ± 0.05	4.17 ± 0.10	584.0 ± 105.0	RR	9.33 ± 2.40	No	Resonant	I
2002 TX ₃₀₀	0.76 ± 0.45	3.37 ± 0.05	323.0 ± 95.0	BBb	0.07 ± 1.39	HH	Hot Classical	S
2002 UX ₂₅	0.11 ± 0.01	3.87 ± 0.02	697.0 ± 24.0	IR	9.31 ± 2.44	Si	Hot Classical	S
2002 VE ₉₅	0.15 ± 0.02	5.70 ± 0.06	249.0 ± 13.0	RR	7.77 ± 3.71	No	Resonant	S
2002 VR ₁₂₈	0.05 ± 0.03	5.58 ± 0.37	448.0 ± 43.0	...	2.76 ± 2.06	No	Resonant	S
2002 VT ₁₃₀	0.10 ± 0.10	5.80 ± 0.30	324.0 ± 68.0	U	...	Si	Inner Classical	S
2002 WC ₁₉	0.17 ± 0.05	4.88 ± 0.07	348.0 ± 45.0	RR	9.36 ± 0.94	Si	Resonant	S
2002 XV ₉₃	0.04 ± 0.02	5.42 ± 0.46	549.0 ± 23.0	...	0.85 ± 2.06	No	Resonant	S
2003 AZ ₈₄	0.11 ± 0.02	3.74 ± 0.08	727.0 ± 66.0	BB	3.65 ± 3.46	Si	Resonant	S
2003 FE ₁₂₈ [†]	0.11 ± 0.09	6.30 ± 0.63	114.0 ± 12.0	Si	Resonant	S
2003 FY ₁₂₈ [†]	0.08 ± 0.01	5.09 ± 0.09	460.0 ± 21.0	IR	1.48 ± 3.46	No	Detached	S

Table C2
(Continued)

Designation	p_V	H_V (mag)	D (km)	Taxonomy	S' (%/1000)	Binarity	Dyn. Class.	OB
2003 OP ₃₂	0.54 ± 0.15	4.10 ± 0.07	274.0 ± 47.0	BBb?	2.40 ± 3.75	HH	Hot Classical	S
2003 QA ₆₂ [†]	0.11 ± 0.09	6.70 ± 0.67	183.0 ± 57.0	...	5.97 ± 3.79	No	Inner Classical	I
2003 QR ₉₁	0.05 ± 0.04	6.55 ± 0.56	280.0 ± 30.0	Si	Hot Classical	S
2003 QW ₅₀ [†]	0.08 ± 0.03	5.00 ± 0.30	401.0 ± 63.0	RR	0.80 ± 3.43	No	Hot Classical	S
2003 UT ₂₉₂	0.07 ± 0.07	6.85 ± 0.68	185.0 ± 18.0	No	Resonant	S
2003 UY ₁₁₇	0.13 ± 0.04	5.70 ± 0.30	247.0 ± 30.0	IR	0.28 ± 0.94	No	Resonant	S
2003 UZ ₄₁₃	0.07 ± 0.02	5.70 ± 0.30	670.0 ± 84.0	...	6.64 ± 3.72	No	Resonant	S
2003 VS ₂	0.15 ± 0.06	4.11 ± 0.38	523.0 ± 35.0	...	1.71 ± 2.06	No	Resonant	S
2004 EW ₉₅	0.04 ± 0.02	6.69 ± 0.35	291.0 ± 25.0	BB	1.71 ± 2.06	No	Resonant	S
2004 GV ₉	0.08 ± 0.01	4.23 ± 0.10	680.0 ± 34.0	BR-IR	4.61 ± 2.91	No	Inner Classical	S
2004 NT ₃₃	0.12 ± 0.07	4.74 ± 0.11	423.0 ± 87.0	BB-BR	...	No	Hot Classical	S
2004 PF ₁₁₅ [†]	0.12 ± 0.04	4.54 ± 0.25	468.0 ± 49.0	No	Inner Classical	S
2004 PG ₁₁₅ [†]	0.11 ± 0.09	4.80 ± 0.48	410.0 ± 34.0	No	Detached	I
2004 PT ₁₀₇	0.03 ± 0.01	6.33 ± 0.11	400.0 ± 51.0	No	Inner Classical	S
2004 TY ₃₆₄	0.11 ± 0.02	4.52 ± 0.07	512.0 ± 40.0	BR-IR	0.78 ± 3.17	No	Inner Classical	S
2004 UX ₁₀	0.14 ± 0.04	4.75 ± 0.16	398.0 ± 39.0	IR-BR	0.23 ± 4.40	No	Inner Classical	S
2004 VT ₇₅ [†]	0.11 ± 0.09	6.20 ± 0.62	231.0 ± 66.0	No	Resonant	S
2004 XA ₁₉₂	0.26 ± 0.34	4.42 ± 0.63	339.0 ± 120.0	No	Detached	S
2005 CA ₇₉ [†]	0.11 ± 0.09	5.20 ± 0.52	365.0 ± 88.0	RR-IR	3.62 ± 2.46	No	Resonant	S
2005 GE ₁₈₇ [†]	0.11 ± 0.09	7.30 ± 0.70	70.0 ± 20.0	...	5.29 ± 6.49	No	Resonant	S
2005 RM ₄₃ [†]	0.11 ± 0.09	4.40 ± 0.44	460.0 ± 17.0	BB	3.01 ± 4.89	No	Detached	S
2005 RN ₄₃	0.11 ± 0.03	3.89 ± 0.05	679.0 ± 73.0	IR	...	No	Inner Classical	S
2005 RR ₄₃	0.44 ± 0.12	4.13 ± 0.08	300.0 ± 43.0	BB	3.89 ± 4.89	No	Hot Classical	S
2005 RS ₄₃ [†]	0.11 ± 0.09	5.00 ± 0.50	401.0 ± 93.0	BR	1.95 ± 2.46	No	Resonant	S
2005 TB ₁₉₀	0.15 ± 0.05	4.40 ± 0.11	464.0 ± 62.0	IR	8.63 ± 1.89	No	Detached	S
2005 UQ ₄₁₃ [†]	0.20 ± 0.08	3.87 ± 0.14	498.0 ± 75.0	No	Hot Classical	S
2006 QJ ₁₈₁ [†]	0.11 ± 0.09	7.20 ± 0.70	73.0 ± 20.0	BR-IR	4.76 ± 4.04	No	Resonant	S
2007 JF ₄₃ [†]	0.11 ± 0.09	5.30 ± 0.53	349.0 ± 85.0	No	Resonant	S
2007 JH ₄₃ [†]	0.11 ± 0.09	4.50 ± 0.45	504.0 ± 105.0	No	Resonant	I
2007 JJ ₄₃ [†]	0.11 ± 0.09	4.50 ± 0.45	504.0 ± 105.0	IR	9.12 ± 1.33	No	Hot Classical	I
2007 OC ₁₀	0.13 ± 0.04	5.43 ± 0.10	309.0 ± 37.0	IR	...	No	Detached	S
2007 XV ₅₀ [†]	0.11 ± 0.09	4.40 ± 0.44	528.0 ± 10.0	No	Hot Classical	S
2008 NW ₄ [†]	0.11 ± 0.09	5.40 ± 0.54	333.0 ± 83.0	No	Detached	S
2008 OG ₁₉ [†]	0.11 ± 0.09	4.70 ± 0.47	460.0 ± 100.0	IR-RR	8.30 ± 0.94	No	Detached	I
2009 YG ₁₉ [†]	0.11 ± 0.09	5.90 ± 0.59	264.0 ± 72.0	No	Resonant	S
2010 ER ₆₅ [†]	0.11 ± 0.09	5.00 ± 0.50	401.0 ± 92.0	No	Detached	S
2010 ET ₆₅ [†]	0.11 ± 0.09	5.10 ± 0.51	383.0 ± 90.0	No	Detached	S
2010 FD ₄₉ [†]	0.11 ± 0.09	6.20 ± 0.62	231.0 ± 66.0	No	Resonant	S
2010 JC ₈₀ [†]	0.11 ± 0.09	5.90 ± 0.60	265.0 ± 73.0	No	Resonant	S
Borasisi	0.24 ± 0.44	6.21 ± 0.07	163.0 ± 66.0	IR-RR	34.20 ± 3.90	Si	Cold Classical	I
Chaos	0.05 ± 0.03	5.00 ± 0.06	600.0 ± 140.0	IR	24.58 ± 2.94	No	Hot Classical	S
Dziewanna	0.30 ± 0.11	3.80 ± 0.10	433.0 ± 64.0	No	Resonant	S
Eris	0.96 ± 0.04	-1.12 ± 0.03	2 326.0 ± 12.0	BBb	1.85 ± 3.08	Si	Detached	S
G!kúnll'hòmđmà	0.17 ± 0.06	3.69 ± 0.10	599.0 ± 77.0	U	0.85 ± 3.17	Si	Detached	S
Gonggong	0.13 ± 0.01	2.34 ± 0.05	1 252.0 ± 43.0	No	Resonant	S
Haumea	0.80 ± 0.10	0.43 ± 0.11	1 239.0 ± 68.0	BBb	-1.53 ± 3.34	HH	Hot Classical	I
Huya	0.08 ± 0.00	5.04 ± 0.03	458.0 ± 9.0	IR	21.89 ± 4.59	Si	Resonant	S
Lempo	0.08 ± 0.01	5.41 ± 0.10	393.0 ± 26.0	RR	2.06 ± 2.34	Si	Resonant	S
Makemake	0.77 ± 0.02	0.14 ± 0.05	1 430.0 ± 9.0	BBb-U	8.32 ± 1.65	Xx	Hot Classical	S
Orcus	0.23 ± 0.02	2.30 ± 0.03	958.0 ± 22.0	BB	1.92 ± 2.47	Si	Resonant	S
Quaoar [†]	0.13 ± 0.01	2.73 ± 0.06	1 073.0 ± 37.0	RR	63.39 ± 1.34	Si	Hot Classical	S
Salacia	0.04 ± 0.00	4.25 ± 0.05	901.0 ± 45.0	BB	...	Si	Inner Classical	I
Sedna	0.41 ± 0.39	1.83 ± 0.05	906.0 ± 314.0	RR	37.31 ± 7.28	No	Detached	S
Sila–Nunam	0.09 ± 0.03	5.56 ± 0.04	343.0 ± 42.0	RR	8.39 ± 3.34	Si	Cold Classical	S
Varda	0.10 ± 0.02	3.61 ± 0.05	792.0 ± 91.0	IR	17.11 ± 7.64	Si	Hot Classical	S
Varuna	0.13 ± 0.04	3.76 ± 0.04	668.0 ± 154.0	IR	24.07 ± 1.91	No	Hot Classical	S

Note. Geometric albedo in V band (p_V), absolute magnitude in V band (H_V), and diameter (D) have been compiled from “TNOs Are Cool” database. In cases where the object was not studied by this project (marked with the symbol †), we calculated the median value of p_V from this database, with H_V from the Minor Planet Center, and we calculated D using Equation (1). For the Haumea family members for which the “TNOs Are Cool” project only provided a lower limit (marked with †), we applied the same procedure using a median value from those family members with known albedos ($p_{V, \text{Haumea}} = 0.58 \pm 0.26$). Taxonomy was taken Fulchignoni et al. (2008), with the exception of those marked with the symbol †, for which it was taken from Belskaya et al. (2015). The spectral gradient was taken from Peixinho et al. (2015). Binarity was taken from the webpage of Lowell Observatory (<http://www2.lowell.edu/users/grundy/tlbs/status.html>); in this column, Haumea family members are labeled as HH. Dynamical classification (Dyn. Class.) follows the work by Gladman et al. (2008). The orbital behavior (OB) is characterized as secure (S) or insecure (I).

(This table is available in machine-readable form.)

Table C3
Visible and Near-infrared Colors Compilation

Designation	$B - V$ (mag)	$V - R$ (mag)	$V - I$ (mag)	$V - J$ (mag)	$V - H$ (mag)	$V - K$ (mag)
1993 SC	1.04 ± 0.13	0.70 ± 0.08	1.45 ± 0.09	2.42 ± 0.07	2.82 ± 0.21	2.78 ± 0.20
1995 SM ₅₅	0.65 ± 0.03	0.37 ± 0.05	0.70 ± 0.05	1.07 ± 0.05	0.59 ± 0.06	0.49 ± 0.05
1995 TL ₈	1.01 ± 0.16	0.62 ± 0.09	1.14 ± 0.21	2.42 ± 0.05	2.82 ± 0.09	2.8 ± 0.09
1996 GQ ₂₁	1.00 ± 0.06	0.70 ± 0.05	1.42 ± 0.07	2.39 ± 0.04	2.88 ± 0.04	3.03 ± 0.08
1996 TK ₆₆ *	0.99 ± 0.06	0.68 ± 0.07	1.28 ± 0.13	2.26 ± 0.18	2.66 ± 0.22	2.66 ± 0.25
1996 TO ₆₆	0.68 ± 0.07	0.39 ± 0.15	0.74 ± 0.07	1 ± 0.1	0.79 ± 0.2	1.6 ± 0.18
1996 TP ₆₆	1.03 ± 0.11	0.66 ± 0.07	1.29 ± 0.11	2.26 ± 0.08	2.42 ± 0.12	2.44 ± 0.11
1998 SM ₁₆₅	0.98 ± 0.08	0.64 ± 0.07	1.34 ± 0.06	2.36 ± 0.01	2.91 ± 0.02	2.96 ± 0.07
1998 SN ₁₆₅ *	0.75 ± 0.08	0.43 ± 0.06	0.98 ± 0.17	1.27 ± 0.05	1.27 ± 0.49	1.33 ± 0.6
1998 VG ₄₄	0.95 ± 0.05	0.56 ± 0.04	1.17 ± 0.11	1.81 ± 0.01	2.21 ± 0.01	2.23 ± 0.01
1999 CD ₁₅₈	0.84 ± 0.07	0.53 ± 0.09	1.10 ± 0.07	1.86 ± 0.07	2.3 ± 0.07	2.33 ± 0.08
1999 DE ₉	0.93 ± 0.10	0.58 ± 0.04	1.16 ± 0.12	1.84 ± 0.04	2.17 ± 0.05	2.19 ± 0.05
1999 OJ ₄ *	0.99 ± 0.08	0.68 ± 0.05	1.22 ± 0.10	2.26 ± 0.18	2.66 ± 0.22	2.66 ± 0.25
2000 CN ₁₀₅ *	1.06 ± 0.10	0.61 ± 0.10	1.35 ± 0.11	1.69 ± 0.13	2.13 ± 0.12	2.29 ± 0.11
2000 GN ₁₇₁	0.96 ± 0.06	0.60 ± 0.04	1.14 ± 0.17	1.84 ± 0.08	2.21 ± 0.14	2.38 ± 0.14
2000 GP ₁₈₃ *	0.77 ± 0.04	0.45 ± 0.05	0.91 ± 0.08	1.22 ± 0.23	1.27 ± 0.49	1.33 ± 0.6
2000 OK ₆₇	0.82 ± 0.12	0.59 ± 0.07	1.14 ± 0.09	2.42 ± 0.08	2.88 ± 0.11	2.92 ± 0.12
2000 PE ₃₀	0.75 ± 0.07	0.37 ± 0.08	0.76 ± 0.09	1.65 ± 0.08	2.09 ± 0.08	2.32 ± 0.11
2000 QL ₂₅₁ *	0.87 ± 0.06	0.49 ± 0.04	0.93 ± 0.09	1.69 ± 0.13	2.13 ± 0.12	2.29 ± 0.11
2000 YW ₁₃₄	0.92 ± 0.05	0.48 ± 0.06	1.08 ± 0.07	1.68 ± 0.12	2.02 ± 0.16	2.18 ± 0.16
2001 CZ ₃₁ ^a	0.6 ± 0.15	0.5 ± 0.1	0.8 ± 0.15	1.53 ± 0.1	2.08 ± 0.14	2.24 ± 0.14
2001 QC ₂₉₈ *	0.66 ± 0.07	0.37 ± 0.07	0.85 ± 0.12	1.69 ± 0.13	2.13 ± 0.12	2.29 ± 0.11
2001 QF ₂₉₈	0.67 ± 0.07	0.39 ± 0.06	0.89 ± 0.19	1.3 ± 0.1	1.53 ± 0.14	1.69 ± 0.15
2001 QS ₃₂₂
2001 QT ₃₂₂	0.71 ± 0.06	0.53 ± 0.12
2001 RZ ₁₄₃	1.08 ± 0.14	0.51 ± 0.13	1.00 ± 0.16
2001 UR ₁₆₃	1.29 ± 0.11	0.86 ± 0.07	1.50 ± 0.12	2.37 ± 0.06	2.86 ± 0.08	2.66 ± 0.25
2001 XD ₂₅₅
2001 YH ₁₄₀ *	0.97 ± 0.08	0.56 ± 0.07	1.07 ± 0.07	1.86 ± 0.06	2.21 ± 0.09	2.31 ± 0.09
2002 AW ₁₉₇	0.88 ± 0.15	0.59 ± 0.04	1.21 ± 0.17	1.82 ± 0.06	2.15 ± 0.08	2.38 ± 0.10
2002 CY ₂₂₄ *	1.12 ± 0.10	0.67 ± 0.04	1.32 ± 0.06	2.26 ± 0.18	2.66 ± 0.22	2.66 ± 0.25
2002 GV ₃₁
2002 KX ₁₄	1.05 ± 0.03	0.61 ± 0.02	1.21 ± 0.16
2002 TC ₃₀₂ *	1.09 ± 0.06	0.65 ± 0.04	1.30 ± 0.06	2.26 ± 0.18	2.66 ± 0.22	2.66 ± 0.25
2002 TX ₃₀₀ ^b	0.70 ± 0.09	0.36 ± 0.02	0.68 ± 0.12	1.0 ± 0.6	0.7 ± 0.7	0.7 ± 0.7
2002 UX ₂₅	0.95 ± 0.13	0.56 ± 0.04	1.05 ± 0.15	1.82 ± 0.09	2.22 ± 0.1	2.22 ± 0.11
2002 VE ₉₅ *	1.07 ± 0.14	0.72 ± 0.05	1.38 ± 0.15	2.26 ± 0.18	2.66 ± 0.22	2.66 ± 0.25
2002 VR ₁₂₈	0.94 ± 0.03	0.60 ± 0.02
2002 VT ₁₃₀ *	1.45 ± 0.21	0.56 ± 0.1	1.19 ± 0.13
2002 WC ₁₉ *	1.14 ± 0.02	0.65 ± 0.01	1.30 ± 0.04	2.26 ± 0.18	2.66 ± 0.22	2.66 ± 0.25
2002 XV ₉₃	0.72 ± 0.02	0.37 ± 0.02
2003 AZ ₈₄	0.65 ± 0.04	0.38 ± 0.04	0.83 ± 0.12	1.46 ± 0.1	1.48 ± 0.14	1.39 ± 0.16
2003 FE ₁₂₈
2003 FY ₁₂₈	1.05 ± 0.03	0.60 ± 0.05	1.14 ± 0.09	1.64 ± 0.06
2003 OP ₃₂	0.70 ± 0.05	0.39 ± 0.06	0.76 ± 0.06
2003 QA ₉₂	1.04 ± 0.03	0.63 ± 0.04
2003 QR ₉₁
2003 QW ₉₀ *	1.11 ± 0.07	0.67 ± 0.06	1.32 ± 0.08	1.98 ± 0.16	2.66 ± 0.22	2.66 ± 0.25
2003 UT ₂₉₂
2003 UY ₁₁₇ *	0.97 ± 0.02	0.56 ± 0.01	1.15 ± 0.02	1.86 ± 0.06	2.21 ± 0.09	2.31 ± 0.09
2003 UZ ₄₁₃	...	0.45 ± 0.06	0.82 ± 0.06
2003 VS ₂	0.93 ± 0.02	0.59 ± 0.02
2004 EW ₉₅ ^{c*}	0.70 ± 0.02	0.38 ± 0.02	...	1.22 ± 0.23	1.27 ± 0.49	1.33 ± 0.6
2004 GV ₉ *	0.90 ± 0.06	0.52 ± 0.03	1.15 ± 0.03	1.77 ± 0.14	2.17 ± 0.14	2.3 ± 0.14
2004 NT ₃₃ *	0.71 ± 0.09	0.42 ± 0.05	0.85 ± 0.09	1.45 ± 0.26	1.7 ± 0.5	1.81 ± 0.61
2004 PF ₁₁₅
2004 PG ₁₁₅
2004 PT ₁₀₇
2004 TY ₃₆₄ *	0.92 ± 0.18	0.60 ± 0.05	1.03 ± 0.18	1.77 ± 0.14	2.17 ± 0.14	2.3 ± 0.14
2004 UX ₁₀ *	0.95 ± 0.02	0.58 ± 0.05	...	1.77 ± 0.14	2.17 ± 0.14	2.3 ± 0.14
2004 VT ₇₅

Table C3
(Continued)

Designation	$B - V$ (mag)	$V - R$ (mag)	$V - I$ (mag)	$V - J$ (mag)	$V - H$ (mag)	$V - K$ (mag)
2004 XA ₁₉₂
2005 CA ₇₉ *	1.12 ± 0.05	0.64 ± 0.04	1.17 ± 0.05	2.06 ± 0.18	2.43 ± 0.22	2.48 ± 0.25
2005 GE ₁₈₇ *	0.98 ± 0.13	0.76 ± 0.10	1.31 ± 0.14
2005 RM ₄₃ *	0.59 ± 0.04	0.40 ± 0.05	0.73 ± 0.04	1.22 ± 0.23	1.27 ± 0.49	1.33 ± 0.6
2005 RN ₄₃ *	0.91 ± 0.04	0.58 ± 0.04	1.14 ± 0.07	1.86 ± 0.06	2.21 ± 0.09	2.31 ± 0.09
2005 RR ₄₃ *	0.79 ± 0.08	0.41 ± 0.05	0.69 ± 0.08	1.22 ± 0.23	1.27 ± 0.49	1.33 ± 0.6
2005 RS ₄₃ *	0.87 ± 0.06	0.50 ± 0.04	0.97 ± 0.05	1.69 ± 0.13	2.13 ± 0.12	2.29 ± 0.11
2005 TB ₁₉₀ *	0.98 ± 0.04	0.56 ± 0.03	1.11 ± 0.04	1.86 ± 0.06	2.21 ± 0.09	2.31 ± 0.09
2005 UQ ₅₁₃
2006 QJ ₁₈₁	0.95 ± 0.11	0.54 ± 0.08	1.02 ± 0.09	2.26 ± 0.18	2.66 ± 0.22	2.66 ± 0.25
2007 JF ₄₃
2007 JH ₄₃
2007 JJ ₄₃ *	1.02 ± 0.03	0.59 ± 0.02	1.09 ± 0.03	1.86 ± 0.06	2.21 ± 0.09	2.31 ± 0.09
2007 OC ₁₀ ^{d*}	0.88 ± 0.01	0.55 ± 0.01	1.02 ± 0.01	1.86 ± 0.06	2.21 ± 0.09	2.31 ± 0.09
2007 XV ₅₀
2008 NW ₄
2008 OG ₁₉ *	0.94 ± 0.02	0.53 ± 0.01	1.12 ± 0.02	2.06 ± 0.18	2.43 ± 0.22	2.48 ± 0.25
2009 YG ₁₉ ^c	1 ± 0.04	0.61 ± 0.04
2010 ER ₆₅
2010 ET ₆₅
2010 FD ₄₉
2010 JC ₈₀
Borasisi	0.86 ± 0.09	0.71 ± 0.06	1.29 ± 0.07	2.01 ± 0.07	2.49 ± 0.11	2.59 ± 0.09
Chaos	0.95 ± 0.05	0.60 ± 0.04	1.24 ± 0.06	1.89 ± 0.03	2.29 ± 0.03	2.32 ± 0.04
Dziewanna
Eris	0.74 ± 0.06	0.39 ± 0.05	0.77 ± 0.06	1.01 ± 0.02	0.72 ± 0.04	0.32 ± 0.05
G!kún *hòmdímà	...	0.62 ± 0.05	1.09 ± 0.05
Gonggong*	0.94 ± 0.11	0.65 ± 0.02	1.33 ± 0.14	2.18 ± 0.06	2.5 ± 0.1	2.5 ± 0.1
Haumea	0.65 ± 0.04	0.34 ± 0.06	0.68 ± 0.04	1.05 ± 0.02	1.01 ± 0.04	0.94 ± 0.05
Huya	0.95 ± 0.05	0.57 ± 0.09	1.19 ± 0.06	1.95 ± 0.02	2.27 ± 0.05	2.37 ± 0.06
Lempo	0.99 ± 0.13	0.69 ± 0.03	1.30 ± 0.13	2.32 ± 0.01	2.7 ± 0.03	2.7 ± 0.02
Makemake ^b	0.82 ± 0.05	0.49 ± 0.02	0.81 ± 0.05	0.98 ± 0.09	0.85 ± 0.1	0.57 ± 0.26
Orcus	0.62 ± 0.08	0.38 ± 0.04	0.75 ± 0.10	1.08 ± 0.04	1.21 ± 0.04	1.25 ± 0.04
Quaoar ^b	0.94 ± 0.11	0.65 ± 0.02	1.33 ± 0.14	2.18 ± 0.06	2.5 ± 0.1	2.5 ± 0.1
Salacia ^{c*}	0.66 ± 0.06	0.4 ± 0.04	0.87 ± 0.01	1.22 ± 0.23	1.27 ± 0.49	1.33 ± 0.6
Sedna	1.17 ± 0.12	0.73 ± 0.12	1.39 ± 0.15	2.32 ± 0.06	2.61 ± 0.06	2.66 ± 0.07
Sila–Nunam	1.08 ± 0.07	0.67 ± 0.05	1.27 ± 0.07	2.06 ± 0.03	2.44 ± 0.08	2.48 ± 0.09
Varda	...	0.58 ± 0.11	1.00 ± 0.17	1.86 ± 0.06	2.21 ± 0.09	2.31 ± 0.09
Varuna	0.93 ± 0.13	0.60 ± 0.04	1.23 ± 0.13	1.99 ± 0.01	2.55 ± 0.07	2.52 ± 0.08

Notes. Visible colors are taken from Peixinho et al. (2015), and infrared colors are taken from Fulchignoni et al. (2008). For those objects without VNIR colors but with taxonomic classification, we took the average color for the corresponding taxonomy (*). See footnotes and Section 3 for exceptions.

^a Fulchignoni et al. (2008).

^b From its spectrum.

^c Peixinho et al. (2015) & Belskaya et al. (2015).

^d Perna et al. (2013).

^e Tegler et al. (2016).

(This table is available in machine-readable form.)

Table C4
Visible and Near-infrared Albedos

Designation	p_B	p_R	p_I	p_J	p_H	p_K
1993 SC	0.08 ± 0.02	0.15 ± 0.03	0.22 ± 0.05	0.40 ± 0.06	0.42 ± 0.20	0.38 ± 0.18
1995 SM ₅₅	0.59 ± 0.04	0.59 ± 0.07	0.59 ± 0.07	0.60 ± 0.07	0.29 ± 0.04	0.25 ± 0.03
1995 TL ₈	0.17 ± 0.06	0.29 ± 0.06	0.35 ± 0.17	0.83 ± 0.10	0.89 ± 0.18	0.82 ± 0.17
1996 GQ ₂₁	0.09 ± 0.01	0.17 ± 0.02	0.25 ± 0.04	0.44 ± 0.04	0.52 ± 0.05	0.56 ± 0.10
1996 TK ₆₆	0.08 ± 0.01	0.15 ± 0.02	0.19 ± 0.06	0.34 ± 0.14	0.36 ± 0.18	0.34 ± 0.20
1996 TO ₆₆	0.57 ± 0.09	0.60 ± 0.21	0.61 ± 0.10	0.56 ± 0.13	0.34 ± 0.16	0.68 ± 0.28
1996 TP ₆₆	0.05 ± 0.01	0.10 ± 0.02	0.13 ± 0.03	0.23 ± 0.04	0.20 ± 0.05	0.19 ± 0.05
1998 SM ₁₆₅	0.06 ± 0.01	0.11 ± 0.02	0.15 ± 0.02	0.28 ± 0.01	0.35 ± 0.02	0.34 ± 0.06
1998 SN ₁₆₅	0.06 ± 0.01	0.06 ± 0.01	0.08 ± 0.03	0.07 ± 0.01	0.06 ± 0.06	0.06 ± 0.08
1998 VG ₄₄	0.05 ± 0.01	0.08 ± 0.01	0.10 ± 0.02	0.13 ± 0.00	0.14 ± 0.00	0.13 ± 0.00
1999 CD ₁₅₈	0.09 ± 0.02	0.13 ± 0.03	0.16 ± 0.03	0.24 ± 0.04	0.26 ± 0.04	0.25 ± 0.05
1999 DE ₉	0.13 ± 0.03	0.20 ± 0.02	0.25 ± 0.07	0.34 ± 0.03	0.34 ± 0.04	0.33 ± 0.04
1999 OJ ₄	0.08 ± 0.02	0.15 ± 0.02	0.18 ± 0.04	0.34 ± 0.14	0.36 ± 0.18	0.34 ± 0.20
2000 CN ₁₀₅	0.11 ± 0.02	0.19 ± 0.04	0.28 ± 0.07	0.28 ± 0.08	0.31 ± 0.08	0.34 ± 0.09
2000 GN ₁₇₁	0.16 ± 0.02	0.27 ± 0.02	0.33 ± 0.13	0.45 ± 0.08	0.47 ± 0.15	0.52 ± 0.17
2000 GP ₁₈₃	0.10 ± 0.01	0.12 ± 0.01	0.13 ± 0.02	0.13 ± 0.07	0.10 ± 0.11	0.10 ± 0.14
2000 OK ₆₇	0.15 ± 0.04	0.21 ± 0.03	0.26 ± 0.05	0.61 ± 0.11	0.69 ± 0.17	0.67 ± 0.19
2000 PE ₃₀	0.10 ± 0.02	0.11 ± 0.02	0.12 ± 0.02	0.19 ± 0.04	0.22 ± 0.04	0.25 ± 0.06
2000 QL ₂₅₁	0.09 ± 0.01	0.12 ± 0.01	0.14 ± 0.03	0.20 ± 0.06	0.22 ± 0.06	0.25 ± 0.06
2000 YW ₁₃₄	0.09 ± 0.01	0.12 ± 0.02	0.16 ± 0.03	0.20 ± 0.06	0.20 ± 0.07	0.22 ± 0.08
2001 CZ ₃₁₁	0.12 ± 0.04	0.13 ± 0.03	0.12 ± 0.04	0.17 ± 0.04	0.21 ± 0.07	0.23 ± 0.08
2001 QC ₂₉₈	0.06 ± 0.01	0.06 ± 0.01	0.07 ± 0.02	0.11 ± 0.03	0.12 ± 0.03	0.14 ± 0.03
2001 QF ₂₉₈	0.07 ± 0.01	0.07 ± 0.01	0.09 ± 0.04	0.09 ± 0.02	0.08 ± 0.03	0.09 ± 0.03
2001 QS ₃₂₂
2001 QT ₃₂₂	0.08 ± 0.01	0.10 ± 0.03
2001 RZ ₁₄₃	0.13 ± 0.04	0.22 ± 0.07	0.25 ± 0.09
2001 UR ₁₆₃	0.12 ± 0.03	0.33 ± 0.05	0.44 ± 0.12	0.72 ± 0.10	0.83 ± 0.15	0.65 ± 0.38
2001 XD ₂₅₅
2001 YH ₁₄₀	0.06 ± 0.01	0.10 ± 0.02	0.11 ± 0.02	0.17 ± 0.02	0.17 ± 0.04	0.18 ± 0.04
2002 AW ₁₉₇	0.09 ± 0.03	0.14 ± 0.01	0.18 ± 0.07	0.23 ± 0.03	0.23 ± 0.04	0.27 ± 0.06
2002 CY ₂₂₄	0.07 ± 0.02	0.15 ± 0.01	0.20 ± 0.03	0.34 ± 0.14	0.36 ± 0.18	0.34 ± 0.20
2002 GV ₃₁
2002 KX ₁₄	0.07 ± 0.00	0.12 ± 0.01	0.16 ± 0.06
2002 TC ₃₀₂	0.08 ± 0.01	0.15 ± 0.01	0.20 ± 0.03	0.36 ± 0.15	0.38 ± 0.19	0.36 ± 0.21
2002 TX ₃₀₀	0.74 ± 0.15	0.76 ± 0.04	0.75 ± 0.21	0.74 ± 1.02	0.41 ± 0.67	0.39 ± 0.63
2002 UX ₂₅	0.08 ± 0.02	0.13 ± 0.01	0.15 ± 0.05	0.22 ± 0.05	0.24 ± 0.05	0.22 ± 0.06
2002 VE ₉₅	0.10 ± 0.03	0.21 ± 0.02	0.28 ± 0.10	0.46 ± 0.19	0.49 ± 0.25	0.47 ± 0.27
2002 VR ₁₂₈	0.04 ± 0.00	0.06 ± 0.00
2002 VT ₁₃₀	0.05 ± 0.02	0.12 ± 0.03	0.15 ± 0.05
2002 WC ₁₉	0.11 ± 0.01	0.22 ± 0.01	0.29 ± 0.03	0.52 ± 0.21	0.55 ± 0.28	0.52 ± 0.30
2002 XV ₉₃	0.04 ± 0.00	0.04 ± 0.00
2003 AZ ₈₄	0.11 ± 0.01	0.11 ± 0.01	0.12 ± 0.03	0.16 ± 0.04	0.12 ± 0.04	0.10 ± 0.04
2003 FE ₁₂₈
2003 FY ₁₂₈	0.06 ± 0.00	0.10 ± 0.01	0.12 ± 0.02	0.14 ± 0.02
2003 OP ₃₂	0.53 ± 0.06	0.56 ± 0.08	0.58 ± 0.08
2003 QA ₉₂	0.08 ± 0.01	0.14 ± 0.01
2003 QR ₉₁
2003 QW ₉₀	0.06 ± 0.01	0.11 ± 0.02	0.15 ± 0.03	0.20 ± 0.07	0.28 ± 0.14	0.26 ± 0.15
2003 UT ₂₉₂
2003 UY ₁₁₇	0.10 ± 0.00	0.15 ± 0.00	0.19 ± 0.01	0.27 ± 0.04	0.28 ± 0.06	0.29 ± 0.06
2003 UZ ₄₁₃	...	0.08 ± 0.01	0.08 ± 0.01
2003 VS ₂	0.12 ± 0.01	0.18 ± 0.01
2004 EW ₉₅	0.04 ± 0.00	0.04 ± 0.00	...	0.05 ± 0.03	0.04 ± 0.05	0.04 ± 0.06
2004 GV ₉	0.06 ± 0.01	0.09 ± 0.01	0.12 ± 0.01	0.15 ± 0.05	0.16 ± 0.05	0.17 ± 0.06
2004 NT ₃₃	0.12 ± 0.03	0.13 ± 0.02	0.14 ± 0.03	0.18 ± 0.11	0.17 ± 0.20	0.18 ± 0.25
2004 PF ₁₁₅
2004 PG ₁₁₅
2004 PT ₁₀₇
2004 TY ₃₆₄	0.09 ± 0.04	0.13 ± 0.02	0.15 ± 0.06	0.21 ± 0.07	0.23 ± 0.07	0.24 ± 0.08
2004 UX ₁₀	0.11 ± 0.01	0.17 ± 0.02	...	0.28 ± 0.09	0.30 ± 0.10	0.32 ± 0.10
2004 VT ₇₅
2004 XA ₁₉₂
2005 CA ₇₉	0.07 ± 0.01	0.14 ± 0.01	0.17 ± 0.02	0.28 ± 0.12	0.29 ± 0.15	0.29 ± 0.17
2005 GE ₁₈₇	0.08 ± 0.02	0.16 ± 0.04	0.19 ± 0.06

Table C4
(Continued)

Designation	p_B	p_R	p_I	p_J	p_H	p_K
2005 RM ₄₃	0.12 ± 0.01	0.11 ± 0.01	0.11 ± 0.01	0.13 ± 0.07	0.10 ± 0.11	0.10 ± 0.14
2005 RN ₄₃	0.09 ± 0.01	0.13 ± 0.01	0.16 ± 0.03	0.23 ± 0.03	0.23 ± 0.05	0.24 ± 0.05
2005 RR ₄₃	0.39 ± 0.07	0.46 ± 0.05	0.44 ± 0.08	0.52 ± 0.28	0.41 ± 0.46	0.41 ± 0.56
2005 RS ₄₃	0.09 ± 0.01	0.13 ± 0.01	0.14 ± 0.02	0.20 ± 0.06	0.22 ± 0.06	0.25 ± 0.06
2005 TB ₁₉₀	0.11 ± 0.01	0.18 ± 0.01	0.22 ± 0.02	0.32 ± 0.04	0.32 ± 0.07	0.34 ± 0.07
2005 UQ ₅₁₃
2006 QJ ₁₈₁	0.09 ± 0.02	0.13 ± 0.02	0.15 ± 0.03	0.34 ± 0.14	0.36 ± 0.18	0.34 ± 0.20
2007 JF ₄₃
2007 JH ₄₃
2007 JJ ₄₃	0.08 ± 0.01	0.14 ± 0.01	0.16 ± 0.01	0.24 ± 0.03	0.24 ± 0.05	0.25 ± 0.05
2007 OC ₁₀	0.10 ± 0.00	0.15 ± 0.00	0.17 ± 0.00	0.27 ± 0.04	0.28 ± 0.06	0.29 ± 0.06
2007 XV ₅₀
2008 NW ₄
2008 OG ₁₉	0.09 ± 0.00	0.13 ± 0.00	0.16 ± 0.01	0.28 ± 0.12	0.29 ± 0.15	0.29 ± 0.17
2009 YG ₁₉	0.08 ± 0.01	0.14 ± 0.01
2010 ER ₆₅
2010 ET ₆₅
2010 FD ₄₉
2010 JC ₈₀
Borasisi	0.20 ± 0.04	0.33 ± 0.04	0.41 ± 0.07	0.58 ± 0.09	0.67 ± 0.17	0.69 ± 0.14
Chaos	0.04 ± 0.00	0.06 ± 0.01	0.08 ± 0.01	0.11 ± 0.01	0.12 ± 0.01	0.11 ± 0.01
Dziewanna
Eris	0.90 ± 0.12	0.99 ± 0.11	1.03 ± 0.14	0.94 ± 0.04	0.53 ± 0.05	0.35 ± 0.04
G!kún 'hòmdímà	...	0.21 ± 0.02	0.24 ± 0.03
Gonggong	0.10 ± 0.03	0.17 ± 0.01	0.23 ± 0.08	0.37 ± 0.05	0.37 ± 0.09	0.35 ± 0.08
Haumea	0.82 ± 0.08	0.79 ± 0.11	0.80 ± 0.07	0.82 ± 0.04	0.58 ± 0.05	0.52 ± 0.06
Huya	0.06 ± 0.01	0.10 ± 0.02	0.13 ± 0.02	0.19 ± 0.01	0.19 ± 0.02	0.20 ± 0.03
Lempo	0.06 ± 0.02	0.11 ± 0.01	0.14 ± 0.04	0.26 ± 0.01	0.27 ± 0.02	0.26 ± 0.01
Makemake	0.67 ± 0.08	0.87 ± 0.04	0.86 ± 0.10	0.74 ± 0.15	0.48 ± 0.11	0.35 ± 0.21
Orcus	0.24 ± 0.04	0.24 ± 0.02	0.24 ± 0.06	0.24 ± 0.02	0.20 ± 0.02	0.20 ± 0.02
Quaoar	0.10 ± 0.03	0.17 ± 0.01	0.23 ± 0.07	0.37 ± 0.05	0.36 ± 0.08	0.34 ± 0.08
Salacia	0.04 ± 0.01	0.05 ± 0.00	0.05 ± 0.00	0.05 ± 0.03	0.04 ± 0.05	0.04 ± 0.06
Sedna	0.26 ± 0.07	0.58 ± 0.16	0.78 ± 0.27	1.35 ± 0.19	1.30 ± 0.18	1.28 ± 0.21
Sila–Nunam	0.06 ± 0.01	0.12 ± 0.01	0.15 ± 0.02	0.23 ± 0.02	0.24 ± 0.04	0.24 ± 0.05
Varda	...	0.12 ± 0.03	0.14 ± 0.05	0.22 ± 0.03	0.22 ± 0.05	0.23 ± 0.05
Varuna	0.10 ± 0.03	0.16 ± 0.01	0.21 ± 0.06	0.31 ± 0.01	0.38 ± 0.06	0.35 ± 0.06

Note. Abbreviations are defined as follows. Albedo at wavelengths: B , R , I , J , H , and K (p_B , p_R , p_I , p_J , p_H , and p_K , respectively). Albedo in V band is shown in Table C2, together with the physical properties of each object.

(This table is available in machine-readable form.)

Table C5
IRAC/Spitzer Colors




Designation	$V - 3.6 \mu\text{m}$ (mag)	$J - 3.6 \mu\text{m}$ (mag)	$K - 3.6 \mu\text{m}$ (mag)	$3.6 \mu\text{m} - 4.5 \mu\text{m}$ (mag)
1993 SC	<0.54	<-0.85	<-0.82	<0.64
1995 SM ₅₅	-1.05 ± 0.42	-1.09 ± 0.26	-0.12 ± 0.26	...
1995 TL ₈	-0.04 ± 0.92	-1.43 ± 0.25	-1.42 ± 0.32	...
1996 GQ ₂₁	0.19 ± 0.41	-1.17 ± 0.22	-1.42 ± 0.28	<-0.71
1996 TK ₆₆	<2.23	<1.00	<0.99	...
1996 TO ₆₆	<-0.61	<-0.58	<-0.79	<0.93
1996 TP ₆₆	<0.36	<-0.87	<-0.66	<0.21
1998 SM ₁₆₅	0.13 ± 0.25	-1.20 ± 0.19	-1.41 ± 0.22	...
1998 SN ₁₆₅	0.67 ± 0.29	0.43 ± 0.19	0.76 ± 1.07	0.20 ± 0.23
1998 VG ₄₄	-0.04 ± 0.71	-0.82 ± 0.55	-0.85 ± 0.55	...
1999 CD ₁₅₈	0.32 ± 0.93	-0.51 ± 0.33	-0.59 ± 0.35	...
1999 DE ₉	0.07 ± 0.25	-0.74 ± 0.17	-0.70 ± 0.18	1.09 ± 0.28
1999 OJ ₄	-0.84 ± 1.87	-2.07 ± 1.79	-2.08 ± 1.82	...
2000 CN ₁₀₅	<1.11	<0.45	<0.24	<-0.43
2000 GN ₁₇₁	-0.09 ± 0.39	-0.90 ± 0.24	-1.05 ± 0.32	0.29 ± 0.33
2000 GP ₁₈₃	0.54 ± 0.66	0.35 ± 0.45	0.63 ± 1.08	...
2000 OK ₆₇	<1.05	<-0.34	<-0.45	<-0.07
2000 PE ₃₀	0.35 ± 0.66	-0.27 ± 0.25	-0.55 ± 0.28	0.38 ± 0.31
2000 QL ₂₅₁	1.11 ± 0.69	0.45 ± 0.37	0.24 ± 0.35	...
2000 YW ₁₃₄	0.50 ± 0.64	-0.15 ± 0.25	-0.26 ± 0.31	...
2001 CZ ₃₁	0.74 ± 0.65	0.24 ± 0.25	-0.08 ± 0.31	...
2001 QC ₂₉₈	0.49 ± 0.41	-0.17 ± 0.37	-0.38 ± 0.36	...
2001 QF ₂₉₈	0.19 ± 0.51	-0.08 ± 0.47	-0.08 ± 0.55	...
2001 QS ₃₂₂	0.20 ± 4.35	<1.51
2001 QT ₃₂₂	<2.04	<-0.47
2001 RZ ₁₄₃	0.53 ± 0.68
2001 UR ₁₆₃	0.84 ± 0.32	-0.50 ± 0.16	-0.40 ± 0.46	0.32 ± 0.21
2001 XD ₂₅₅	0.32 ± 0.66
2001 YH ₁₄₀	0.01 ± 0.52	-0.82 ± 0.23	-0.88 ± 0.26	...
2002 AW ₁₉₇	0.39 ± 0.12	-0.40 ± 0.14	-0.57 ± 0.20	0.18 ± 0.19
2002 CY ₂₂₄	1.42 ± 0.66	0.19 ± 0.38	0.18 ± 0.49	...
2002 GV ₃₁	<0.29	<-0.55
2002 KX ₁₄	0.28 ± 0.19	0.06 ± 0.33
2002 TC ₃₀₂	-0.04 ± 0.34	-1.27 ± 0.34	-1.28 ± 0.46	0.31 ± 0.18
2002 TX ₃₀₀	-1.75 ± 0.48	-1.72 ± 1.07	-1.03 ± 1.25	0.07 ± 0.37
2002 UX ₂₅	-0.01 ± 0.11	-0.80 ± 0.19	-0.81 ± 0.22	0.22 ± 0.18
2002 VE ₉₅	-0.32 ± 0.15	-1.55 ± 0.34	-1.56 ± 0.46	0.57 ± 0.20
2002 VR ₁₂₈	0.58 ± 0.42
2002 VT ₁₃₀	<-0.51
2002 WC ₁₉	0.12 ± 0.28	-1.11 ± 0.35	-1.12 ± 0.46	...
2002 XV ₉₃	0.82 ± 0.41
2003 AZ ₈₄	-0.32 ± 0.20	-0.75 ± 0.21	-0.29 ± 0.30	-0.03 ± 0.17
2003 FE ₁₂₈	0.63 ± 0.90
2003 FY ₁₂₈	0.33 ± 0.17	-0.28 ± 0.18	...	0.25 ± 0.19
2003 OP ₃₂	-1.71 ± 0.44	<0.92
2003 QA ₉₂	0.95 ± 1.00
2003 QR ₉₁	1.91 ± 0.52
2003 QW ₉₀	0.13 ± 0.34	-0.82 ± 0.37	-1.11 ± 0.50	...
2003 UT ₂₉₂	0.20 ± 0.81
2003 UY ₁₁₇	0.15 ± 0.28	-0.68 ± 0.19	-0.74 ± 0.22	...
2003 UZ ₄₁₃	0.24 ± 0.27
2003 VS ₂	0.05 ± 0.35	0.09 ± 0.16
2004 EW ₉₅	0.58 ± 0.41	0.39 ± 0.44	0.67 ± 1.08	...
2004 GV ₉	0.42 ± 0.17	-0.32 ± 0.29	-0.46 ± 0.29	0.40 ± 0.22
2004 NT ₃₃	0.54 ± 0.45	0.12 ± 0.48	0.15 ± 1.09	-0.26 ± 0.21
2004 PF ₁₁₅	-0.04 ± 0.32
2004 PG ₁₁₅	-0.36 ± 0.48	<-0.72
2004 PT ₁₀₇	1.03 ± 0.31
2004 TY ₃₆₄	0.09 ± 0.21	-0.65 ± 0.29	-0.79 ± 0.29	0.31 ± 0.21
2004 UX ₁₀	0.08 ± 0.29	-0.66 ± 0.30	-0.80 ± 0.30	...
2004 VT ₇₅	-0.21 ± 0.69
2004 XA ₁₉₂	0.16 ± 1.03	0.39 ± 0.31
2005 CA ₇₉	-0.33 ± 0.66	-1.36 ± 0.38	-1.39 ± 0.49	...
2005 GE ₁₈₇	1.52 ± 0.52

Table C5
(Continued)

Designation	$V - 3.6 \mu\text{m}$ (mag)	$J - 3.6 \mu\text{m}$ (mag)	$K - 3.6 \mu\text{m}$ (mag)	$3.6 \mu\text{m} - 4.5 \mu\text{m}$ (mag)
2005 RM ₄₃	-0.07 ± 0.65	-0.26 ± 0.44	0.02 ± 1.07	-0.73 ± 0.27
2005 RN ₄₃	0.21 ± 0.23	-0.62 ± 0.15	-0.68 ± 0.19	0.22 ± 0.14
2005 RR ₄₃	<-1.18	<-1.37	<-1.09	<0.11
2005 RS ₄₃	-0.12 ± 0.66	-0.78 ± 0.32	-0.99 ± 0.29	...
2005 TB ₁₉₀	-0.28 ± 0.43	-1.11 ± 0.25	-1.17 ± 0.30	...
2005 UQ ₅₁₃	-0.15 ± 0.37	-0.01 ± 0.29
2006 QJ ₁₈₁	2.63 ± 0.66	1.40 ± 0.38	1.39 ± 0.49	...
2007 JF ₄₃	-0.16 ± 0.66
2007 JH ₄₃	0.29 ± 0.64
2007 JJ ₄₃	0.16 ± 0.65	-0.67 ± 0.18	-0.73 ± 0.22	-0.04 ± 0.32
2007 OC ₁₀	-0.06 ± 0.40	-0.89 ± 0.26	-0.95 ± 0.31	...
2007 XV ₅₀	-0.42 ± 0.66
2008 NW ₄	-0.59 ± 0.67
2008 OG ₁₉	-0.39 ± 0.65	-1.42 ± 0.36	-1.45 ± 0.47	...
2009 YG ₁₉	-0.27 ± 0.67
2010 ER ₆₅	-0.48 ± 0.93
2010 ET ₆₅	-0.14 ± 0.93
2010 FD ₄₉	-0.07 ± 0.66
2010 JC ₈₀	-0.77 ± 0.53	<0.52
Borasisi	0.20 ± 1.45	-0.78 ± 0.29	-0.97 ± 0.31	<1.25
Chaos	0.25 ± 0.69	-0.61 ± 0.25	-0.65 ± 0.25	0.57 ± 0.32
Dziewanna	-0.63 ± 0.32	0.35 ± 0.19
Eris	-1.77 ± 0.06	-1.75 ± 0.07	-0.67 ± 0.10	1.50 ± 0.08
G!kún 'hòmdímà	-0.73 ± 0.78	0.71 ± 0.82
Gonggong	0.45 ± 0.11	-0.70 ± 0.12	-0.63 ± 0.16	...
Haumea	-1.45 ± 0.12	-1.47 ± 0.08	-0.97 ± 0.12	-0.92 ± 0.12
Huya	0.06 ± 0.17	-0.86 ± 0.17	-0.89 ± 0.20	-0.12 ± 0.27
Lempo	0.12 ± 0.19	-1.17 ± 0.15	-1.16 ± 0.15	0.14 ± 0.31
Makemake	-2.08 ± 0.08	-2.03 ± 0.18	-1.23 ± 0.47	1.80 ± 0.10
Orcus	-0.85 ± 0.10	-0.90 ± 0.11	-0.68 ± 0.11	-0.54 ± 0.16
Quaoar	0.18 ± 0.12	-0.97 ± 0.14	-0.90 ± 0.20	-0.24 ± 0.15
Salacia	0.46 ± 0.10	0.27 ± 0.30	0.55 ± 0.76	0.02 ± 0.09
Sedna	0.01 ± 0.74	-1.28 ± 0.16	-1.23 ± 0.17	0.61 ± 0.21
Sila-Nunam	-0.08 ± 0.27	-1.11 ± 0.22	-1.14 ± 0.24	0.61 ± 0.23
Varda	0.37 ± 0.22	-0.46 ± 0.16	-0.52 ± 0.20	0.33 ± 0.15
Varuna	-0.13 ± 0.27	-1.09 ± 0.10	-1.23 ± 0.17	0.19 ± 0.15

(This table is available in machine-readable form.)

ORCID iDs

E. Fernández-Valenzuela  <https://orcid.org/0000-0003-2132-7769>
N. Pinilla-Alonso  <https://orcid.org/0000-0002-2770-7896>
J. Stansberry  <https://orcid.org/0000-0003-2434-5225>
J. P. Emery  <https://orcid.org/000-0001-9265-9475>
C. Van Laerhoven  <https://orcid.org/0000-0003-2231-3414>
B. J. Gladman  <https://orcid.org/0000-0002-0283-2260>
W. Fraser  <https://orcid.org/0000-0001-6680-6558>
D. Cruikshank  <https://orcid.org/0000-0002-0541-5569>
E. Lellouch  <https://orcid.org/0000-0001-7168-1577>
T. G. Müller  <https://orcid.org/0000-0002-0717-0462>
W. M. Grundy  <https://orcid.org/0000-0002-8296-6540>
D. Trilling  <https://orcid.org/0000-0003-4580-3790>
Y. Fernandez  <https://orcid.org/0000-0003-1156-9721>
C. Dalle Ore  <https://orcid.org/0000-0003-4787-0014>

References

Alvarez-Candal, A., Barucci, M. A., Merlin, F., Guilbert, A., & de Bergh, C. 2007, *A&A*, 475, 369

Alvarez-Candal, A., Pinilla-Alonso, N., Licandro, J., et al. 2011, *A&A*, 532, A130
Alvarez-Candal, A., Pinilla-Alonso, N., Ortiz, J. L., et al. 2016, *A&A*, 586, A155
Barkume, K. M., Brown, M. E., & Schaller, E. L. 2008, *AJ*, 135, 55
Barucci, M. A., Alvarez-Candal, A., Merlin, F., et al. 2011, *Icar*, 214, 297
Barucci, M. A., Belskaya, I. N., Fulchignoni, M., & Birlan, M. 2005a, *AJ*, 130, 1291
Barucci, M. A., Cruikshank, D. P., Dotto, E., et al. 2005b, *A&A*, 439, L1
Barucci, M. A., Doressoundiram, A., Tholen, D., Fulchignoni, M., & Lazzarin, M. 1999, *Icar*, 142, 476
Barucci, M. A., & Merlin, F. 2020, in *The Trans-Neptunian Solar System*, ed. D. Prrialnik et al. (Amsterdam: Elsevier), 109
Barucci, M. A., Merlin, F., Dotto, E., Doressoundiram, A., & de Bergh, C. 2006, *A&A*, 455, 725
Barucci, M. A., Merlin, F., Guilbert, A., et al. 2008, *A&A*, 479, L13
Belskaya, I. N., Barucci, M. A., Fulchignoni, M., & Dovgopel, A. N. 2015, *Icar*, 250, 482
Bessell, M. S. 2005, *ARA&A*, 43, 293
Bessell, M. S., & Brett, J. M. 1988, *PASP*, 100, 1134
Boehnhardt, H., Delsanti, A., Barucci, A., et al. 2002, *A&A*, 395, 297
Brown, M. E. 2001, *AJ*, 121, 2804
Brown, M. E. 2008, in *The Solar System Beyond Neptune*, ed. M. A. Barucci et al. (Tucson, AZ: Univ. Arizona Press), 335
Brown, M. E., Barkume, K. M., Blake, G. A., et al. 2007a, *AJ*, 133, 284
Brown, M. E., Barkume, K. M., Ragozzine, D., & Schaller, E. L. 2007b, *Natur*, 446, 294

- Brown, R. H., Cruikshank, D. P., & Pendleton, Y. 1999, *ApJL*, 519, L101
- Brucker, M. J., Grundy, W. M., Stansberry, J. A., et al. 2009, *Icar*, 201, 284
- Cruikshank, D. P., Imanaka, H., & Dalle Ore, C. M. 2005, *AdSpR*, 36, 178
- Cruikshank, D. P., Roush, T. L., Bartholomew, M. J., et al. 1998, *Icar*, 135, 389
- Dalle Ore, C. M., Barucci, M. A., Emery, J. P., et al. 2009, *A&A*, 501, 349
- de Bergh, C., Boehnhardt, H., Barucci, M. A., et al. 2004, *A&A*, 416, 791
- de Bergh, C., Delsanti, A., Tozzi, G. P., et al. 2005, *A&A*, 437, 1115
- Delsanti, A., Hainaut, O., Jourdeuil, E., et al. 2004, *A&A*, 417, 1145
- Delsanti, A., Merlin, F., Guilbert-Lepoutre, A., et al. 2010, *A&A*, 520, A40
- Delsanti, A., Peixinho, N., Boehnhardt, H., et al. 2006, *AJ*, 131, 1851
- Delsanti, A. C., Boehnhardt, H., Barrera, L., et al. 2001, *A&A*, 380, 347
- DeMeo, F. E., Barucci, M. A., Merlin, F., et al. 2010, *A&A*, 521, A35
- DeMeo, F. E., Fornasier, S., Barucci, M. A., et al. 2009, *A&A*, 493, 283
- Doressoundiram, A., Barucci, M. A., Romon, J., & Veillet, C. 2001, *Icar*, 154, 277
- Doressoundiram, A., Boehnhardt, H., Tegler, S. C., & Trujillo, C. 2008, in *The Solar System Beyond Neptune*, ed. M. A. Barucci (Tucson, AZ: Univ. Arizona Press), 91
- Doressoundiram, A., Peixinho, N., de Bergh, C., et al. 2002, *AJ*, 124, 2279
- Doressoundiram, A., Peixinho, N., Doucet, C., et al. 2005, *Icar*, 174, 90
- Doressoundiram, A., Peixinho, N., Moullet, A., et al. 2007, *AJ*, 134, 2186
- Doressoundiram, A., Tozzi, G. P., Barucci, M. A., et al. 2003, *AJ*, 125, 2721
- Dorschner, J., Begemann, B., Henning, T., Jaeger, C., & Mutschke, H. 1995, *A&A*, 300, 503
- Dotto, E., Barucci, M. A., Boehnhardt, H., et al. 2003, *Icar*, 162, 408
- Emery, J. P., & Brown, R. H. 2004, *Icar*, 170, 131
- Emery, J. P., Dalle Ore, C. M., Cruikshank, D. P., et al. 2007, *A&A*, 466, 395
- Fazio, G. G., Hora, J. L., Allen, L. E., et al. 2004, *ApJS*, 154, 10
- Fernández, J. 2020, in *The Trans-Neptunian Solar System*, ed. D. Prrialnik et al. (Amsterdam: Elsevier), 1
- Fernandez, J. A. 1980, *MNRAS*, 192, 481
- Fornasier, S., Barucci, M. A., de Bergh, C., et al. 2009, *A&A*, 508, 457
- Fornasier, S., Doressoundiram, A., Tozzi, G. P., et al. 2004a, *A&A*, 421, 353
- Fornasier, S., Dotto, E., Barucci, M. A., & Barbieri, C. 2004b, *A&A*, 422, L43
- Fornasier, S., Lellouch, E., Müller, T., et al. 2013, *A&A*, 555, A15
- Fraser, W. C., & Brown, M. E. 2012, *ApJ*, 749, 33
- Fraser, W. C., Brown, M. E., & Glass, F. 2015, *ApJ*, 804, 31
- Fulchignoni, M., Belskaya, I., Barucci, M. A., de Sanctis, M. C., & Doressoundiram, A. 2008, in *The Solar System Beyond Neptune*, ed. M. A. Barucci et al. (Tucson, AZ: Univ. Arizona Press), 181
- Gil-Hutton, R. 2002, *P&SS*, 50, 57
- Gladman, B., Marsden, B. G., & Vanlaerhoven, C. 2008, in *The Solar System Beyond Neptune*, ed. M. A. Barucci et al. (Tucson, AZ: Univ. Arizona Press), 43
- Gourgeot, F., Barucci, M. A., Alvarez-Candal, A., et al. 2015, *A&A*, 582, A13
- Grundy, W. M., Bird, M. K., Britt, D. T., et al. 2020, *Sci*, 367, aay3705
- Grundy, W. M., Buie, M. W., & Spencer, J. R. 2005, *AJ*, 130, 1299
- Grundy, W. M., Schmitt, B., & Quirico, E. 2002, *Icar*, 155, 486
- Guilbert, A., Alvarez-Candal, A., Merlin, F., et al. 2009, *Icar*, 201, 272
- Hainaut, O. R., Boehnhardt, H., & Protopapa, S. 2012, *A&A*, 546, A115
- Hansen, G. B. 1997, *JGR*, 102, 21569
- Hapke, B. 1993, *Topics in Remote Sensing* (Cambridge: Cambridge Univ. Press)
- Hapke, B., & Wells, E. 1981, *JGR*, 86, 3055
- Hastie, T., Tibshirani, R., & Friedman, J. 2001, *The Elements of Statistical Learning*, Springer Series in Statistics (New York: Springer)
- Imanaka, H., Cruikshank, D. P., Khare, B. N., & McKay, C. P. 2012, *Icar*, 218, 247
- James, G., Witten, D., Hastie, T., & Tibshirani, R. 2013, *An Introduction to Statistical Learning: with Applications in R* (Berlin: Springer), <https://faculty.marshall.usc.edu/gareth-james/ISL/>
- Jewitt, D. C., & Luu, J. 2004, *Natur*, 432, 731
- Jewitt, D. C., & Luu, J. X. 2001, *AJ*, 122, 2099
- Johnson, H. L. 1964, in *Astronomical Techniques*, ed. W. A. Hiltner (Chicago, IL: Univ. Chicago Press), 157
- Kalirai, J. 2018, *ConPh*, 59, 251
- Kavelaars, J. J., Jones, R. L., Gladman, B. J., et al. 2009, *AJ*, 137, 4917
- Khain, T., Becker, J. C., Adams, F. C., et al. 2018, *AJ*, 156, 273
- Khare, B. N., Sagan, C., Arakawa, E. T., et al. 1984, *Icar*, 60, 127
- Khare, B. N., Thompson, W. R., Cheng, L., et al. 1993, *Icar*, 103, 290
- Lacerda, P., Fornasier, S., Lellouch, E., et al. 2014, *ApJL*, 793, L2
- Lellouch, E., Santos-Sanz, P., Lacerda, P., et al. 2013, *A&A*, 557, A60
- Levison, H. F., & Duncan, M. J. 1997, *Icar*, 127, 13
- Licandro, J., di Fabrizio, L., Pinilla-Alonso, N., de León, J., & Oliva, E. 2006a, *A&A*, 457, 329
- Licandro, J., Grundy, W. M., Pinilla-Alonso, N., & Leisy, P. 2006b, *A&A*, 458, L5
- Licandro, J., Oliva, E., & Di Martino, M. 2001, *A&A*, 373, L29
- Licandro, J., Pinilla-Alonso, N., Pedani, M., et al. 2006c, *A&A*, 445, L35
- Lorenzi, V., Pinilla-Alonso, N., Licandro, J., Dalle Ore, C. M., & Emery, J. P. 2014, *A&A*, 562, A85
- Marsset, M., Fraser, W. C., Bannister, M. T., et al. 2020, *PSJ*, 1, 16
- Mastrapa, R. M., Sandford, S. A., Roush, T. L., Cruikshank, D. P., & Dalle Ore, C. M. 2009, *ApJ*, 701, 1347
- Materese, C. K., Cruikshank, D. P., Sandford, S. A., et al. 2014, *ApJ*, 788, 111
- Materese, C. K., Cruikshank, D. P., Sandford, S. A., Imanaka, H., & Nuevo, M. 2015, *ApJ*, 812, 150
- Merlin, F., Alvarez-Candal, A., Delsanti, A., et al. 2009, *AJ*, 137, 315
- Merlin, F., Barucci, M. A., Dotto, E., de Bergh, C., & Lo Curto, G. 2005, *A&A*, 444, 977
- Merlin, F., Guilbert, A., Dumas, C., et al. 2007, *A&A*, 466, 1185
- Merlin, F., Quirico, E., Barucci, M. A., & de Bergh, C. 2012, *A&A*, 544, A20
- Morbidelli, A., & Nesvorný, D. 2020, in *The Trans-Neptunian Solar System*, ed. D. Prrialnik et al. (Amsterdam: Elsevier), 25
- Müller, T., Lellouch, E., & Fornasier, S. 2020, in *The Trans-Neptunian Solar System*, ed. D. Prrialnik et al. (Amsterdam: Elsevier), 153
- Müller, T. G., Lellouch, E., Bönhardt, H., et al. 2009, *EM&P*, 105, 209
- Palmer, E. E., & Brown, R. H. 2008, *Icar*, 195, 434
- Parker, A. H., & Kavelaars, J. J. 2010, *ApJL*, 722, L204
- Pedregosa, F., Varoquaux, G., Gramfort, A., et al. 2011, *Journal of Machine Learning Research*, 12, 2825, <https://www.jmlr.org/papers/v12/pedregosa11a.html>
- Peixinho, N., Delsanti, A., & Doressoundiram, A. 2015, *A&A*, 577, A35
- Perna, D., Barucci, M. A., Fornasier, S., et al. 2010, *A&A*, 510, A53
- Perna, D., Dotto, E., Barucci, M. A., et al. 2013, *A&A*, 554, A49
- Petit, J.-M., Kavelaars, J. J., Gladman, B. J., et al. 2011, *AJ*, 142, 131
- Pinilla-Alonso, N., Brunetto, R., Licandro, J., et al. 2009, *A&A*, 496, 547
- Pinilla-Alonso, N., Licandro, J., Gil-Hutton, R., & Brunetto, R. 2007, *A&A*, 468, L25
- Pinilla-Alonso, N., Licandro, J., & Lorenzi, V. 2008, *A&A*, 489, 455
- Pinilla-Alonso, N., Roush, T. L., Marzo, G. A., Cruikshank, D. P., & Dalle Ore, C. M. 2011, *Icar*, 215, 75
- Pinilla-Alonso, N., Stansberry, J. A., & Holler, B. J. 2020, in *The Trans-Neptunian Solar System*, ed. D. Prrialnik et al. (Amsterdam: Elsevier), 395
- Protopapa, S., Alvarez-Candal, A., Barucci, M. A., et al. 2009, *A&A*, 501, 375
- Quirico, E., & Schmitt, B. 1997, *Icar*, 127, 354
- Reach, W. T., Megeath, S. T., Cohen, M., et al. 2005, *PASP*, 117, 978
- Schaller, E. L., & Brown, M. E. 2007a, *ApJL*, 659, L61
- Schaller, E. L., & Brown, M. E. 2007b, *ApJL*, 670, L49
- Schaller, E. L., & Brown, M. E. 2008, *ApJL*, 684, L107
- Schwamb, M. E., Fraser, W. C., Bannister, M. T., et al. 2019, *ApJ*, 243, 12
- Secull, T., Fraser, W. C., Puzia, T. H., Brown, M. E., & Schönebeck, F. 2018, *ApJL*, 855, L26
- Smith, E. V. P., & Gottlieb, D. M. 1974, *SSRv*, 16, 771
- Snodgrass, C., Carry, B., Dumas, C., & Hainaut, O. 2010, *A&A*, 511, A72
- Stansberry, J., Grundy, W., Brown, M., et al. 2008, in *The Solar System Beyond Neptune*, ed. M. A. Barucci et al. (Tucson, AZ: Univ. Arizona Press), 161
- Tegler, S. C., Romanishin, W., & Consolmagno, G. J., S. J. 2016, *AJ*, 152, 210
- Thirouin, A., Ortiz, J. L., Campo Bagatin, A., et al. 2012, *MNRAS*, 424, 3156
- Trujillo, C. A., & Brown, M. E. 2002, *ApJL*, 566, L125
- Trujillo, C. A., Brown, M. E., Barkume, K. M., Schaller, E. L., & Rabinowitz, D. L. 2007, *ApJ*, 655, 1172
- Trujillo, C. A., Brown, M. E., Rabinowitz, D. L., & Geballe, T. R. 2005, *ApJ*, 627, C57
- Van Laerhoven, C., Gladman, B., Volk, K., et al. 2019, *AJ*, 158, 49
- Vilenius, E., Kiss, C., Mommert, M., et al. 2012, *A&A*, 541, A94
- Vilenius, E., Kiss, C., Müller, T., et al. 2014, *A&A*, 564, A35
- Vilenius, E., Stansberry, J., Müller, T., et al. 2018, *A&A*, 618, A136
- Werner, M. W., Roellig, T. L., Low, F. J., et al. 2004, *ApJS*, 154, 1
- Young, L. A., Braga-Ribas, F., & Johnson, R. E. 2020, in *The Trans-Neptunian Solar System*, ed. D. Prrialnik et al. (Amsterdam: Elsevier), 127